A High-Purity Germanium Imaging System for Limited-Angle Nuclear Breast Tomography

By

Desmond L. Campbell

Dissertation

Submitted to the Faculty of the

Graduate School of Vanderbilt University

in partial fulfillment of the requirements

for the degree of

DOCTOR OF PHILOSOPHY

in

Physics

May, 2015

Nashville, Tennessee

Approved:

Professor Todd Peterson

Professor Arnold Burger

Professor David Ernst

Professor Julia Velkovska

Professor Thomas Yankeelov

To my loving family,

to my friends near and far

and

to my supportive wife

ACKNOWLEDGMENTS

The work discussed in this dissertation has been supported by the following entities and funding sources: NIH/NIBIB R44EB15889, NIH/NCI R25CA136440, the Graduate Assistance in Areas of National Need fellowship, the Department of Physics and Astronomy, and the Southern Region Education Board. The work was conducted in part using the resources of the Advanced Computing Center for Research and Education at Vanderbilt University, Nashville, TN.

I have thoroughly enjoyed my time at Vanderbilt. The past six years learning and working with Dr. Todd Peterson has afforded me some of the best experiences of my life. I am eternally grateful for his guidance and assistance with this work. I would also like to extend my thanks to the members of my dissertation committee, Dr. Arnold Burger, Dr. David Ernst, Dr. Julia Velkovska, and Dr. Thomas Yankeelov, for their insightful comments and suggestions during my graduate tenure. I would also like to thank all current and former members of the Ionizing Imaging group, Dr. Lindsay Johnson, Dr. Sepideh Shokouhi, Dr. M. Noor Tantawy, Dr. Benjamin McDonald, Oleg Ochinnikov, and Rose Perea. Additionally, I would like to recognize the Vanderbilt University Institute of Imaging Science for their graduate education and training programs, which have enriched my understanding of physics and the biomedical sciences. I also greatly appreciate the efforts made by Ethan Hull at PHDs Co. and Ben Welch at Dilon Technologies and thank them for their support and assistance through this work.

The support offered by the faculty, post-docs, coordinators, and members of the Fisk-Vanderbilt Bridge program have sustained me through this journey. The people of the "Bridge Family" are incredible and it has been an honor to learn and grow with all of you. To my friends near and far, thank you as well. Your encouragement and kind words have provided me with strength to endure all challenges. And finally to my family, thank you for your continuous and unyielding faith in me. I hope I have made you proud.

TABLE OF CONTENTS

LIST OF TABLES

LIST OF FIGURES

CHAPTER I

INTRODUCTION AND BACKGROUND

The objective of this work is to design and demonstrate the potential imaging capability of a breast-specific High-Purity Germanium (HPGe) imaging system. Traditionally, HPGe detectors were used for spectrometry and source identification due to their superb energy resolution, but the technological challenges of the 1970s limited biomedical imaging capability. Advancements in amorphous semiconductor contacts, cryogenics, and readout electronics in the last 40 years have now made HPGe detectors realistic for single-photon imaging. Currently, research with compact HPGe cameras, fabricated for small-animal imaging, is being conducted; yet extensive work is needed to determine if HPGe cameras would offer any potential benefit to other applications.

One application worth exploring is Nuclear Breast Imaging (NBI). The evolution of NBI has been dictated by the need for improved screening and diagnostic imaging to better identify disease in women with mammographically dense breast while maintaining the mammography radiation dose to the patient. Currently, Breast-Specific Gamma Imaging (BSGI) and Molecular Breast Imaging (MBI) planar acquisition techniques use specially-designed breast-specific cameras with higher sensitivity and specificity than screening mammography. MBI employs the state-of-the-art clinical

breast imaging system, which utilizes pixellated Cadmium Zinc Telluride (CZT) and square-hole collimation registered to the pixels for the best spatial resolution and geometric sensitivity tradeoff. However, the detector capabilities of Germanium detectors have the potential to improve upon breast imaging performance for a few reasons. The good transport properties of Germanium could overcome the sensitivity loss due to tailed events observed in CZT. These sensitivity gains would allow for injecting less of the radiotracer to lower overall radiation dose to the patient. The energy resolution could suppress scattered events and events originating outside the field-of-view from degrading image quality. Finally, a Limited-Angle Tomographic acquisition may be possible with Germanium cameras. Its depth-of-interaction estimation capabilities with mounted wide collimation would grant an HPGe camera a greater degree of angular sampling around an object without the need of object or camera rotation. Applying an iterative reconstruction algorithm with the limited-angle acquisition scheme could result in 3D images with potential enhancements in contrast and resolution.

To carry out the objective of exploring HPGe-detector potential performance for NBI, Monte Carlo computational methods will be used to accomplish three specific aims.

1. To demonstrate the potential benefits Germanium detectors offer to NBI.

2. To develop a breast-specific Germanium imaging system for limited-angle tomography.

3. To explore the limits of performance for a dual-head limited-angle tomography HPGe imaging system

The radiation transport package Monte Carlo N-Particle, version 5 (MCNP5) will be used for all simulations. MCNP5 outputs particle tracking files of position and photon energies of collisions, which are parsed using MATLAB to retrieve data about energy deposition and to generate images. Because the computational burden of these simulations is large, utilizing the campus cluster ACCRE will be essential to expedite run time.

For aim 1, published findings of simulations modeling a CZT imaging system will be replicated by generating images with the breast/torso phantom. This system's performance will be compared against the performance of a generic Germanium system by substituting the 5-mm CZT for 10-mm HPGe and repeating the measurements. Experimental characterization and validation of the Germanium camera will be performed and measured system parameters will be incorporated into the HPGe model. Imaging performance is assessed based on sensitivity (number of absorbed photons), scatter and torso fractions, and tumor contrast. It is expected that for equivalent activity imaged, an optimal HPGe breast camera will provide improvements in sensitivity and tumor contrast while better suppressing small-angle scatter events and background from outside the FOV.

For aim 2, various registered parallel-hole collimators will be evaluated for geome-

try sensitivity, resolution and tumor contrast of contrast-detail and breast phantoms. Limited-angle tomography will be incorporated with the best performing collimator by generating a system matrix that maps object space to the detector. Applying an iterative MLEM algorithm will allow previously collected 2D projections with depth of interaction information to be reconstructed into 3D images. Projections and slices of the generated 3D images will be compared to the 2D planar images created from previous simulations and evaluated by tumor contrast and system resolution. It is expected that the modeled HPGe breast imaging system will provide the advantages of HPGe detectors observed in aim 1 while providing enhancements in spatial resolution and tumor contrast due to the addition of tomographic imaging methods.

Finally for aim 3, a dual-head imaging system using two opposing HPGe cameras will be investigated. Dual-head systems exhibit approximately double system sensitivity over single camera systems and improve spatial resolution close to the second camera. It has been observed that using opposing dual-head cameras with additional image processing and analysis can enhance imaging sensitivity as well as the estimation of some tumor properties, including 3D localization and size. Simulations with opposing HPGe cameras optimized in aim 2 will be conducted to generate planar images. Applying an OSEM reconstruction with opposing-planar images will provide tomographic images. It is expected that the combination of depth of interaction information from HPGe detectors, attenuation differences between acquired projections, and application of the OSEM reconstruction algorithm will provide better localization

and size of tumors with increased spatial resolution contrast than planar images.

The remainder of the chapter will discuss some essential background for full comprehension of this work. Information on biomedical imaging, radiation detectors, select modalities for breast cancer screening, and the evolution of Germanium detectors will be discussed.

1.1 Radionuclide Imaging Overview

Radionuclide imaging is a biomedical imaging technique designed to acquire the spatial distribution of a particular biological process of interest. A molecule of interest is labeled with a radioactive atom with a known characteristic emission and introduced to the subject, usually through injection. The radiotracer is more readily absorbed where the biological process of interest is occurring at higher rates compared to other locations within the body. The radioactive atom attached to the molecule of interest undergoes a radioactive decay process that results in the isotropic emission of the known characteristic gamma ray. Photons not obstructed or attenuated by the subject are collected by external gamma cameras. With calibration of the gamma camera, an energy spectrum of the absorbed photon energies is generated. Placing an energy window or discriminator for the characteristic energy of emitted photons filters out scattered or incomplete events, leaving events with full charge collection within the camera. With position estimation of the energy-filtered events, a projection image of the radiotracer distribution within the subject can be generated. This information

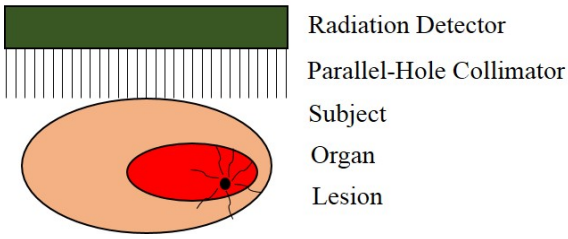

Figure 1: A schematic diagram of a radionuclide scan after injection of a radiotracter. Components are labeled, including the detector, collimator, and subject with a lesion. In cancer imaging, radiotracers has preferential uptake in malignant tissue and appear as hot spots in projections.

can be used to visualize, localize, and characterize the subject for irregularities or disease without initial need for investigative surgery.

The instrument utilized for measuring the radiotracer distribution is the gamma camera. The camera is capable of constraining the direction of incident radiation, measuring, and localizing the energy of absorbed photons. This is accomplished with a few essential components, the collimator and the radiation detector. The collimator consists of a plate constructed from a high-Z material, such as lead or tungsten, with several small holes. The collimator is mounted to the front of the camera and is responsible for limiting the direction which photons can enter. Photons traveling towards the collimator at an oblique angle relative to the normal are absorbed by the high-Z material, preventing entry to the detector. Depending on the characteristic energy of the radiation and the biomedical application, different types of collimation is employed. Most commonly used for clinical applications is the parallel-hole collimator, comprised of a highly density material with multiple small holes for photons to pass through. Behind the collimator is a radiation detector, another dense material

which absorbs incident photons and converts it into a current pulse. Various radiation detectors are utilized for radionuclide imaging with gamma cameras, which some of the most popular are discussed in section 1.2. Some consideration, specifically for the radiation detector, are the relevant properties that largely dictate gamma camera performance. These properties are discussed in the following section.

1.1.1 Relevant Imaging Properties

1.1.1.1 Efficiency

An important property of any detector is its sensitivity to radiation, or better known as its efficiency. The absolute efficiency, which is the ratio of the number of events recorded to the number of emitted radiation particles, depends on both characteristics of the detector and the geometry of the system. More widely used however is the intrinsic efficiency of a detector, also known as the Quantum Detection Efficiency (QDE), which is defined as the ratio of the number of events recorded to the number of emitted radiation particles incident on the detector. When primarily discussing detectors, the intrinsic efficiency is tabulated rather than the absolute efficiency, as the intrinsic efficiency depends upon the density, electronic density, stopping power, attenuation coefficient of the material, its thickness and the incident photon energy (Knoll, 2000; Bushberg and Boone, 2002). The collimator mounted to the gamma camera also has a geometric efficiency for allowing propagating photons to pass. This efficiency, also known as sensitivity, for radiation is dependent upon

collimator type, material, thickness, and hole dimension. Paralllel-hole collimators are quite pertinent to clinical gamma cameras, and their geometric efficiency are discussed more in chapter V.

1.1.1.2 Spatial Resolution

Another important property of a gamma camera is its spatial resolution. Within the image or detector space, the spatial resolution is the minimum lateral distance to resolve two distinct hot spots or points. The geometric resolution of the collimator contributes the most to the spatial resolution of an image, on the order of the collimator pitch. The spatial resolution of the system can be evaluated by acquiring an image of a point source and measuring the full width at half maximum (FWHM) of the point spread function (PSF). Single point sources are rare in nature, so line sources or edge spread functions are acquired instead to measure spatial resolution. Limits on the intrinsic spatial resolution differ between scintillators and semiconductor detectors. Pixelated detectors typically have resolution limits on the order of the detector element size, but energy resolution also influences spatial resolution. Poorer energy resolution forces utilization of wider energy windows and allows for scattered events to spread the PSF (Bushberg and Boone, 2002; Cherry et al., 2012; Hendee and Ritenour, 2003). Energy resolution is discussed further.

1.1.1.3 Energy Resolution

An intrinsic property of radiation detectors is the energy resolution; an observable in detector response distributions. It is a measurement of the spread in a energy spectrum due to fluctuations in the response of a detector. The energy resolution is defined as the dimensionless ratio between the FWHM of the photopeak and the energy of the photopeak. Scintillation detectors have energy resolutions of $\sim$10% at 140 keV, while semiconductor detectors have superior resolution ranging from 1%-5% at 140 keV. A general assumption about detector response is that the energy input is typically linear to its output, which validates the theory that the peak centroid is proportional to the number of charge carriers created per ionization event. If the FWHM stays relatively constant, then the energy resolution could be improved with use of a material that creates more charge carriers per event (Knoll, 2000).

1.2 Radiation Detectors

1.2.1 Scintillators

The technique of observing radiation by the collection of scintillated light created in materials has been one of the more useful and reliable methods in the study of radiation emission. Scintillation detectors work through a process of converting emitted radiation into visible light through interactions with an organic or inorganic scintillation material. When radiation interacts with the scintillator, electrons-hole pairs are created and elevated to higher energy levels. These particles lose some energy

through other non-radiative processes and collapse down to activator energy states. The scintillation light is generated when these electron-hole pairs recombine from the activator energy states. The emitted scintillator light travels down optical pipes to photomultiplier tubes (PMT), where the light is converted into photoelectrons at the cathode. The number of photoelectrons are multiplied through collisions along a series of dynodes over a variable bias. This avalanche of electrons contributes to the production of an electrical signal, which undergoes further processing of amplification and shaping before being collected for analysis (Knoll, 2000; Bushberg and Boone, 2002; Hendee and Ritenour, 2003).

The ideal scintillation detectors hold properties that maximize the efficiency in converting emitted radiation into the electrical signal. One property of importance that is unique to scintillator materials is its luminosity, better known as its light yield or light output. The ideal scintillator would quickly transfer the energy from ionizing radiation into light with a high efficiency. Also, this conversion of light should be linearly proportional from the lower energy x-ray to high energy gamma-rays. The time of the total luminosity should be on the order of nanoseconds for the entire process of fluorescence and phosphorescence. Highly dense scintillators with high Z numbers are also favorable for detectors as those materials more readily stop x-rays and gamma-rays, which leads to shorter attenuation coefficients and higher intrinsic efficiencies (Bushberg and Boone, 2002).

One of the most popular inorganic scintillators used for radiation detection is

Sodium Iodide doped with Thallium as an activator, NaI(Tl). It is considered the gold standard scintillator material for radiation detector due to its superb light yield and near linear response over high gamma-ray energies. Because of its superb light yield, NaI(Tl) also has an excellent energy resolution ($\sim$10% at 140 keV) in comparison to other inorganic scintillators (Peterson and Furenlid, 2011; Hendee and Ritenour, 2003). Its decay time of 230 ns is average for scintillators, but for use in medical imaging with high count rates, it is long. In addition, NaI(Tl) undergoes a form of delayed fluorescence called phosphorescence, which further extends the time of scintillation within the crystal and limits the timing capability of NaI(Tl) detectors. It is also a very delicate material that cracks easily and absorbs moisture from the air, making encasement necessary. Even with some of its shortcomings, it is inexpensive to produce, and thus has been the basis for the Anger Camera, the clinical standard for gamma cameras and nuclear medical devices systems (Knoll, 2000; Bushberg and Boone, 2002).

Table 1 lists the properties of select scintillator crystals used for nuclear medicine and other applications. A considerable amount of work has been accomplished with CsI(Tl) and La-based scintillators due to their high light yield, which translates into good energy resolution. A novel scintillator, SrI_2, has emerged as a suitable candidate for potential imaging application with high light yield, but decay times are uncomfortably slow for high count rate acquisitions.

Table 1: Properties of select scintillators. Table information acquired from Peterson and Furenlid (2011); Van Loef et al. (2009).

	Density (g/cm^3)	Attenuation Coe. at 140 keV (cm^{-1})	Maximum Emission (nm)	Decay Time (ns)	Light Yield (photons/keV)
NaI(Tl)	3.67	3.12	415	230	38
CsI(Tl)	4.51	4.53	540	680 (63%), 3340 (37%)	65
$LaCl_3$(Ce)	3.86	2.82	330	20 (70%), 213 (30%)	49
$LaBr_3$(Ce)	5.30	3.42	358	35 (90%)	61
SrI_2(Eu)	4.59	-	435	1110	80

1.2.2 Semiconductors

Semiconductor diode detectors hold great advantages over scintillation crystals due to their superior energy resolution from the larger number of charge carriers produced per ionization event. Because of the process of converting ionization energy into an electric signal for scintillation detectors, energy on the order of 100 eV is required to produce a charge carrier. However, because semiconductors are able to directly convert ionizing radiation into an electrical signal, only a few eV, depending on the semiconductor, is necessary to create an electron-hole pair. As the energy requirements for producing charge carriers in semiconductors is much lower than in scintillators, radiation of certain energy will yield more charge carriers in semiconductors than in scintillators. This increase in charge carriers allows for the reduction in statistical fluctuations and improves upon energy resolution. Semiconductor diode detectors are also compact in size and have relatively fast timing properties that allow for the process of pulses in high count rates scenarios.

Semiconductor detectors work on the effects of doping them with materials with one more valence electron (n-type) and one fewer valence electron (p-type). The

addition of these impurities in the semiconductor growth process will form a semiconductor junction with an imbalance of electrons and holes; holes being the absence of electrons. This region is known as the depletion region, which can absorb radiation. The charge imbalance of electrons and holes in the depletion region yields a small potential (ψ) that satisfies Poisson's equation:

$$\nabla^2\psi = -\frac{\rho}{\epsilon}, \tag{1}$$

where ρ is the volumetric charge density and ϵ is the dielectric constant of the semiconductor. With a reverse bias applied to the semiconductor, the negative and positive ions travel away from the junction and increase the width of the depletion region. This can be seen from the voltage dependence on the width of the depletion region in (2):

$$d = \sqrt{\frac{2V\epsilon}{eN}}. \tag{2}$$

Thus, applying an appropriate voltage that extends the depletion region throughout the thickness of the semiconductor maximizes the active volume of the detector and provides the highest possible efficiency for ionizing radiation.

There are a few important relevant properties of semiconductor diode detectors. The energy gap between the valence and conduction band, the band gap, is the most predominant of properties for the semiconductor. For a material to be considered a semiconductor, its band gap must be small enough, on the order of a few eV,

to allow for thermal excitation of electrons. This gives semiconductors their high conductivity over insulators. The probability of thermally generated electron-hole pairs in semiconductors heavily depends on the ratio of the band gap energy and the operation temperature of the detector. For some semiconductor detectors, such as Germanium, this property creates a necessity to operate them at 70 K to minimize the number of thermally excited ions. However, this is not the case for Cadmium Zinc Telluride or Silicon detectors.

The applied electric field in a semiconductor diode detector heavily affects the migrating of negative and positive charges towards the electrodes for collection. The net drift velocity of both the electrons and holes are linearly proportional to the magnitude of the electric field by the mobility of that particle. In most semiconductors, the electron- and hole-mobilities are roughly similar, so collection times for the electrons and holes are also similar, on the order of tens of nanoseconds. At higher electric fields, the drift velocity eventually reaches a saturation point, where increasing the electric field ceases to increase the net drift velocity. For fast detection, semiconductor diodes are operated at applied electric fields that allow for this drift velocity saturation, which allow for quick collection times. Diffusion of charge also affects the collection time, as charge will drift down longer paths while approaching the anode and cathode, slightly increasing the collection time and altering position measurements. These effects are minimal in small volume detectors, but cause significant changes in timing and position measurements in large volume detectors (Knoll,

Table 2: Properties of select semiconductor. Table information adopted from Peterson and Furenlid (2011).

	Density (g/cm^3)	Attenuation Coe. at 140 keV (cm^{-1})	Energy per e-h pair (eV)	Mobility-Lifetime Electron (cm^2/V)	Mobility-Lifetime Hole (cm^2/V)
Si	2.33	0.02	3.61	0.42	0.22
Ge	5.32	0.72	2.98	0.72	0.84
CZT	5.82	3.07	5.0	3×10^{-3}	5×10^{-5}

2000).

Trapping and recombination effects due to the presence of impurities can also affect the total collection of charge and worsen energy resolution. Electrons and holes can be captured by impurities that contain energy states in between the valence and conduction bands. In one case of trapping effects, these charge carriers are trapped and released, but after the measurement of the pulse. In the case of recombination, an electron and hole recombine and annihilate in the region of an impurity. There can be also structural defects, such as point or line defects, in the semiconductor that can contribute to trapping and recombination. These combined effects contribute to the loss of charge and can cause a decrease in the measurement of the true energy of x-rays and gamma-rays. This in turn can negatively affect the energy resolution of the detector (Knoll, 2000; Barber, 1996)

Table 2 lists the properties of select semiconductors used for nuclear imaging. Silicon is an appropriate detector for x-ray, CT, and low energy gamma-ray applications, but is not directly applicable to the work of this document. CZT and HPGe are discussed in greater detail in the following sections.

1.2.2.1 Cadmium Zinc Telluride

Cadmium Zinc Telluride, a compound material of Zinc Telluride and Cadmium Telluride, is a popular room temperature semiconductor. CZT is a highly dense material with a density of 6.2 g/cm^3. Its band gap energies can range from 1.53 eV to 1.64 eV, depending on the ZnTe and CdTe concentrations. Electron mobility is much better at 1350 cm^2/Vs than its hole mobility at 120 cm^2/Vs. CZT has a measured energy resolution as good as 1.7% at 662 keV and ionization energy of 5.0 eV per electron-hole pair (Knoll, 2000). These properties allow for more compact systems with superior energy resolution at room temperature than NaI(Tl) scintillators.

However, CZT suffers from charge carrier transport issues and has high industrial costs. Improvements have been made through designing different detector geometries and additional signaling processing with added electronics to account for the poor hole transport, however, it is unclear if these improvements would work with large volume detector-arrays. Energy resolution for CZT detectors has been shown to be superior to most scintillators. Even with better resolution, spectra of CZT can comprise of long tails that span to the low energy side of the photo peak. This effect is caused by charge carrier trapping, pixel non-uniformity in charge collection between the center and boundaries of the pixel, and the slow drift velocity of holes. The low energy tailing effect can be mitigated by utilizing small pixels sizes in CZT detector systems. The weighting potential strength near the small contacts with preferential absorption of gamma rays allows for only negative charge carriers to

contribute to signal generation and removes the influence of hole drifting. Adding collimator walls around the individual pixels to shield against boundary and pixel sharing effects also improves spectral quality (Wagenaar, 2004; Barrett et al., 1995; Bolotnikov et al., 2005). Arrays of 3D position-sensitive pixilated CZT spectrometers have been developed using Application Specific Integration Circuit (ASIC) readout systems that integrate the energy and timing circuits into a single chipset, but the spectrometers still suffer from variations in electron trapping, electronic noise, nonlinearity and nonuniformity between pixels (Zhang et al., 2004, 2005).

1.2.2.2 Germanium

Germanium (Ge) is another semiconductor material with major use in several disciplines requiring gamma-ray spectroscopy. Originally grown using lithium drift methods as Ge(Li) (read:Jelly) detectors, the development of zone refinement techniques led to ultrahigh purity Germanium, known as HPGe. Ge has a moderate density of 5.32 g/cm^3 with a low bandgap of 0.665 eV at 300 K. The mobilities of electrons and holes in Germanium at room temperature are superior to CZT with values of 3900 and 1900 cm^2/Vs. However, the low bandgap of Germanium results in thermal excitations of charge-carriers, making Ge detectors nonoperational at room temperature. For this reason, traditional Ge detectors are cooled using liquid nitrogen or other refrigeration methods to 77 K. This improves Germanium performance by increasing the mobility of charge-carriers to 3.6×10^4 and 4.2×10^4 cm^2/Vs for elec-

trons and holes, respectively. Combined with generating 2.96 electron-hole pairs per eV absorbed, Germanium yields the best energy resolution of any radiation detector at <1% at 140 keV (Knoll, 2000; Johnson et al., 2011a). The challenges of keeping HPGe detectors at liquid nitrogen temperatures hindered their development. However, attempts at fabricating and evaluating HPGe gamma cameras have been made in past and are highlighted in section 1.3.

1.3 Germanium Gamma Camera History

Original designs for Germanium detectors included orthogonal strip contacts on monolithic slabs of germanium for position sensitivity. One of the first position sensitive HPGe detectors was first tested in the 1960s. J. F. Detko evaluated a 20 mm × 20 mm × 10 mm orthogonal-strip HPGe in the late 1960s. The system had a 3.27% energy resolution at 122 keV and a measured spatial resolution of 3 mm (Detko, 1969). Several other HPGe detectors were evaluated by other groups for spatial and energy resolution, including a detector with a 2 cm × 2 cm area and a thickness of 10 mm. Typical spatial and energy resolutions measured with these detectors were between 2.2-4.0 mm and 2.5% @ 140 keV on average, respectively (Schlosser et al., 1974).

These properties were attractive for nuclear medicine, so work towards a clinical system was pursued. The first clinical tests on a prototype gamma-camera were constructed from lithium-drifted germanium that was 44 mm × 44 mm in area and

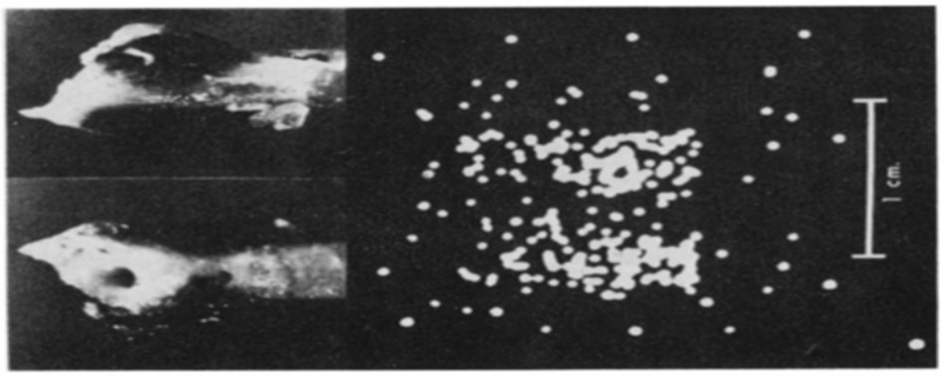

Figure 2: An in-vivo image of a rat thyroid acquired with an orthogonal-strip HPGe camera developed by J.F. Detko. I-123 was injected into the tail vein and a 10 minute/7200-count image was obtained. Anterior and Posterior views of the excised thyroid are displayed above the acquired image. Figure reproduced from Ter-Pogossian and Phelps (1973).

6.5 mm in useful thickness. Rat and human imaging of the thyroid with ^{99m}Tc-pertechnetate was performed and compared against the standard Anger camera (McCready et al., 1971; Detko, 1973). As shown in figure 2, localization of the thyroid was observed with the HPGe system, with an intrinsic resolution of 3 mm (Ter-Pogossian and Phelps, 1973). Another example of HPGe imaging system development for clinical application was accomplished at Vanderbilt in collaboration with Lawrence Berkley Laboratories. The system utilized a 9 element array of HPGe detectors in a tomographic imaging system. Favorable results for animal and patient imaging were observed (Patton et al., 1978).

Even with excellent intrinsic properties, early HPGe detectors suffered from disadvantages that made them impractical for nuclear medicine. Temperature and vacuum instability caused variations in detector and subsequent imaging performing (Ter-

Pogossian and Phelps, 1973). These designs used diffused dopant contacts, which were required to sit within cut channels in the detector material to reduce capacitance effects between electrodes and impaired detector efficiency. Also sorting out multiple-hit events was difficult and often worsened energy resolution. These difficulties halted the development of HPGe cameras for medical imaging applications (Barber, 1996).

During the mid-90s and through the turn of the century, amorphous-semiconductor contacts for Germanium detectors were further developed from work completed in the 1970s (Luke et al., 2000; Hansen and Haller, 1977). The fabrication of these new contacts is described as a simple process which provides finer pitch electrodes than diffused Lithium metal contacts (Luke et al., 2000). These new contacts have led to the development of prototype position-sensitive germanium detectors for imaging applications in many fields (Amman and Luke, 2000).

The process for obtaining position information from orthogonal strip detectors is through pulse shape analysis of signal waveforms, shown in figure 3. The electron-hole pairs generated from absorbed photons induce full signals on the collecting strips. However, the induction of short-lived transient signals on adjacent neighboring strips are also generated during charge carrier travel towards the collecting strips. Using *a posteriori* knowledge of the ratio between the difference in the maximum or integral of these transient signals and the deposited energy, position estimation and spatial resolutions finer than the physical width of the strips can be achieved. Depth in-

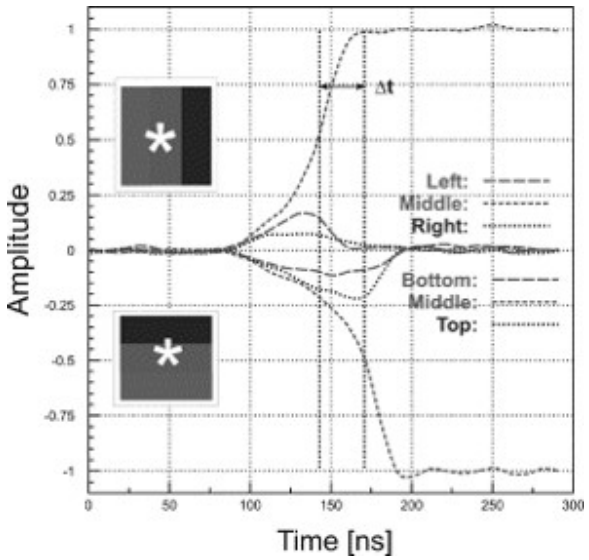

Figure 3: An example waveform characterizing a single event absorbed in a double-sided strip Germanium detector. Full charge collection over a set of orthogonal strips forms the large amplitude signals, while charge-carrier motion through electrode potential induces transient signals on neighboring strips. Real charge is not collect on neighboring strips, resulting in the quick rise and fall of transient signal. Ratios of the transient signals are used for inter-strip interpolation. Figure reproduced from Vetter et al. (2004).

formation of photonic interactions can be gathered from the difference in the time of max signal from charge-carrier collection. Pulse shape analysis of collected signal waveforms ultimately enables position sensitivity in all three dimensions (Burks et al., 2004; Vetter et al., 2004).

A disadvantage to double-sided strip detectors is their gaps between the strips. While wider gaps can decrease capacitance between strips, the additional space can lead to the trapping of charge-carriers and eventual charge loss. Events that undergo charge loss are typically deemed unusable and are excluded. Moreover, Compton events that propagate to adjacent strips or lead to trapped charge-carriers in gaps are excluded from processing, ultimately decreasing detection efficiency. A significant amount of work to correct for charge loss due to gaps has been accomplished by Hayward and Wehe (2007, 2008a,b). They found that interactions that occur within the gap are complicated by: (1) incomplete charge collection; (2) signal variance due to charge-carrier cloud size and motion; (3) distinguishing between single interactions and multiple close interactions to the gap. Haywood and Wehe developed correction methods for single site interactions and close Compton events depend on the measured energy from the adjacent strips.

Others have also explored the use of HPGe detectors as imaging cameras. One study modeled and compared the performance between a Germanium Orthogonal Strip Detector (GOSD) and an Anger camera with NaI(Tl) scintillation crystals in a simulated breast study. Their results suggest that GOSD will provide better contrast,

SNR and superior spatial resolution with a small sacrifice in sensitivity. However, the superior energy resolution of Germanium compensates for its relatively modest linear attenuation coefficient and offers moderate sensitivity compared to the Anger camera (Gombia et al., 2002).

A group at the University of Liverpool has been exploring the use of Germanium detectors for pre-clinical and other imaging applications. The Small Animal Reconstruction Tomography for Positron Emission Tomography (SmartPET) system was developed originally as a proof of principle by using two 20 mm thick HPGe detectors to measure coincident 511 keV events of ^{22}Na sources. The study lead to the advancement of event categorization using pulse shape analysis to determine the order of interactions in each detector. Even with decent energy and spatial resolution, sensitivity measurements were poor for 511 keV photons (Cooper et al., 2009). The Liverpool group has explored using the SmartPET system for Compton imaging, which has improved sensitivity for SPECT radionuclide photon energies. The system may best be optimized when HPGe is used as the scattering detector or as the analyzing detector (Harkness et al., 2009).

1.4 Breast Cancer Imaging

1.4.1 X-Ray Mammography

Mammography is a radiographic examination that is specialized for detecting breast tumors. For over 60 years, mammography has been the medical standard for

breast imaging for the screening of breast cancer. Although the technique of mammography has not changed since the mid-1950s, several technologic components have seen advancements and improvements for better contrast and detail. X-ray mammography takes advantage of the differences between healthy tissue and cancerous tissue in the breast. X-rays are sensitive to the changes in electron density of these tissues, causing linear attenuation differences across the range of x-rays energies. Bombarding x-rays through the breast to analog or digital film produces a planar image of the attenuation differences, where microcalcifications or other irregularities can be identified (Bushberg and Boone, 2002).

There are several advantages that make mammography the current standard for breast imaging. It has a low cost and is widely available across the globe. Using x-ray mammography, many trained medical professionals are able to deduce and identify whether a patient is positive for tumors and its level of malignancy or benignancy. This yields to a high sensitivity percentage of correctly identifying cancers. Most importantly, mammography delivers a very low dosage of radiation to the body. In a recent study comparing the absorbed dose in different nuclear breast imaging modalities, the cumulative radiation dose associated with annual screening mammography in women between 40 and 80 years young was estimated to induce 20-25 cases of cancer per 100,000 patients. Mammography is the only technique that has been proven to lower the risk of terminal breast cancer in women (Hendrick, 2010).

However, mammography is greatly limited in a sub-section of women with dense

breast tissue. In these mammographically dense breast patients, the rate of false-negatives (the misdiagnosis of no cancer when breast tumors are actually present) increases, causing sensitivity to fall off considerably. Furthermore, the specificity, or the ability to accurately detect the presence of no cancer or detect benign tumors, is said to be very low in mammography. This is due to the lack of metabolic or functional information from mammograms (Rosenberg et al., 1998). Because the detection of cancer can be poor or inconclusive, an increase of biopsies, a very invasive procedure that involves removing living tissue to test for the presence of disease, is seen. Avoiding unnecessary biopsy procedures with severe complications in the case of false-positive cases (when a cancer diagnosis is given for a healthy patient) can lower hospital cost, patient cost, and save the patient a load of grief. At the core of the problem, medical professionals and their patients require novel breast imaging techniques that will better allow them to identify disease.

This has been the motivation for the improvements made in the technology and techniques of breast imaging. There is a plethora of breast imaging techniques that have been developed and seen success in the clinical realm. Many of these modalities are outside the scope of this paper, as its focus is the development of radiation detectors for the measurement of single-photon emitting tracers. The following section will briefly highlight alternative breast imaging techniques and how they compare to mammography.

1.4.2 Alternative Imaging Modalities

1.4.2.1 Ultrasonography

Ultrasonography (US) is an ultrasound based technique used to non-invasively visualize internal structures of the body. When first applied to breast imaging in the mid-1960s, it was referred to as ultrasound mammography. Ultrasound works through the emission and absorption of sound waves that propagate through the body and interact at the boundary of regions with varying density and acoustic properties. Collection of these reflected waves is used in the reconstruction of an image.

Advantages to breast ultrasonography are its ability to image with decent spatial resolution and sensitivity with the lack of ionizing radiation dose to the patient. However, there is a trade-off between the resolution and the depth which one can image with US. Original work with ultrasonography of breast found that it is more sensitive than screening mammography, but that there are still issues with diagnosing false positives due to the lack of specificity of sound waves to determine malignancy (Baum, 1977; Warwick et al., 1988). Because of this, breast ultrasonography is presently considered a diagnostic tool that can be employed after screening mammography has been done (Silverstein et al., 2005).

1.4.2.2 Magnetic Resonance Imaging

Magnetic Resonance Imaging (MRI) is another technique used for breast cancer screening and diagnostic imaging. Instead of using ionizing radiation like mammogra-

phy and other nuclear breast imaging techniques, MRI uses magnetic fields and radio waves to manipulate nuclear magnetization to visualize internal structures with good spatial resolution and tissue contrast.

MRI has been investigated as a tool for the screening of women with mammographically dense breasts who have a genetic predisposition to cancer. One study showed that in women with a high cumulative lifetime risk for cancer, MRI had a sensitivity of 79.5%, which was more than twice as sensitive as mammography at 33.3% (Kriege et al., 2004). With MRIs superior sensitivity over mammography, another study continued screening at-risk patients and evaluated tumor progression and prognosis against a similar group of patients screened with mammography. MRI discovered smaller, less advance-staged breast tumors than conventional x-ray mammography, and as a result, reduced incidences of late stage tumors by 70% (Warner et al., 2011). Despite evidence that MRI is less specific than other modalities, including mammography, use of MRI screenings enables better differentiation capability of cancer than mammography (Kriege et al., 2004).

1.4.2.3 Positron Emission Mammography

Positron Emission Mammography (PEM) uses the technology of position emission tomography (PET) to acquire tomographic images of the biodistribution of ^{18}F-Fludeoxyglucose (FDG), a glucose derivative highly absorbed in malignant tumors. Early designs of PEM systems used various highly dense, high Z scintillators such

as Bismuth Germanate (BGO) and Gadolinium Oxyorthosilicate (GSO) as planar detectors. Characterization of these systems using breast phantom with simulated tumors revealed this technique's advantages. Overall, the systems are very sensitive and specific to cancerous tissues with spatial resolutions down to 2 - 4 mm. When light compression of the breast is applied, as opposed to standard prone or supine positions, detectability of lesions increases such that 5 mm tumors were visible (Thompson et al., 1995; Raylman et al., 2000). When a BGO PEM system was first brought to clinical trials with a small number of subjects, 86% sensitivity and 100% specificity were found (Murthy et al., 2000).

Observations of PEMs limitation were the amount of Compton scatter events recorded ($\sim$12% of events), which only increased as the breast density increased. Increases in breast density also caused a decrease in minimum tumor size detectability to the point where tumors less than 1 cm in diameter were not visible. Furthermore, the radiation dose involved in PEM has a 20 times higher fatal radiation-induced cancer risk than screening mammography for women of age 40 and above (Hendrick, 2010). Absorbed doses can be diminished with better radiation detectors with improved efficiency, such as Lutetium Oxyorthosilicate (LSO) or even semiconductors, which would produce images of similar quality with less injected radioactivity. Consensus among medical professionals states that even though PEM has similar sensitivity and slightly improved specificity to breast MRI, dose and risk concerns make it an adequate adjunct to mammography only when MRI is unavailable or gives contradicting

results from other modalities (Silverstein et al., 2005).

1.4.3 Nuclear Breast Imaging Methods

Nuclear Breast Imaging (NBI) is an umbrella term that is used to encompass breast imaging modalities that utilize internalized radiopharmaceuticals that emit high energy gamma-ray radiation and is measured and localized using solid state detectors. In the following section, the evolution of NBI is outlined with its own advantages over screening mammography and its current limitations as an imaging technique.

1.4.3.1 Scintimammography

Scintimammography is best described as breast-specific scintigraphy, where radionuclide-labeled tracers are injected and more readily absorbed in cancerous tissue than healthy tissue. Scans are performed by having patients lay on a bed in a prone position with general-purpose or whole-body gamma cameras that acquire planar images, an example of which appears in figure 4. The radiopharmaceutical Technetium-99m sestamibi (^{99m}Tc-MIBI), originally a pharmaceutical for investigating cardiac dynamics, is injected as a tracer for tumors. This system and procedure allows for planar images of each breast to be taken in similar projections to complement screening mammography (Khalkhali et al., 1999).

When ^{99m}Tc-MIBI was found to be a suitable radiotracer for the identification of

Figure 4: Photograph of a woman undergoing a conventional scintimammography scan using general-purpose cameras. The patient lies in a prone position with cameras imaging laterally from the body. Photo reproduced from www.imaginis.com.

cancer, several centers studied its usefulness in the detection of breast cancer as a complement to screening mammography. Methods for prone imaging of breast were followed in many studies that compared screening mammography and scintimammography. Khalkhali found that in a study of 147 women with 153 breast lesions, his scintimammography techniques were able to detect 92.2% of the malignant tumors accurately (sensitivity) and 89.2% of the benign tumors accurately (specificity) (Khalkhali et al., 1995). Studies conducted in other centers across the globe (Canada, Spain, and Texas, USA) using Khalkhali's method for prone imaging found very similar results in the performance of scintimammography. Over the course of these studies, the sensitivity to detecting malignant tumors for scintimammography ranged between 83% and 92%, while specificity of benign tumor detection had a wider range of 79% to 94% (Taillefer et al., 1995; Villanueva-Meyer et al., 1996; Prats et al., 1999). Examples of collected images are displayed in figure 5. In many of the studies, patients

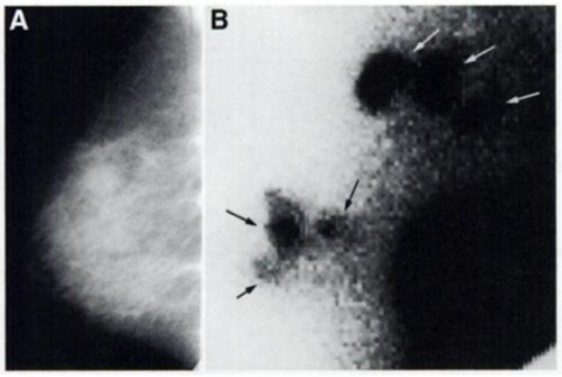

Figure 5: a) A mammogram presents with a malignant mass and architectural distortion with possible metastases at the lymph node. b) The same breast acquired using scintimammography. Black arrows correlate to cancer masses and white arrows point to axillary lymph node involvement. Images reproduced from Prats et al. (1999).

were selected based on mammograms that showed inconclusive or abnormal results, which is a common occurrence in at-risk women with dense breast tissue.

Scintimammography has a couple of advantages over standard x-ray mammography. Most importantly, the technique is independent of breast density due to the use of high energy gamma rays that are better able to penetrate through tissue. The interference patterns observed in standard mammography often shield small breast tumors that go undetected, worsening sensitivity and specificity. As such, scintimammography's sensitivity and specificity are superior to mammography. In the case of indeterminate or inconclusive mammograms, scintimammography is another technique better able to detect the presence of malignant cancers rather than pursuing invasive biopsies.

However, scintimammography also exhibits its own set of limitations. The major reason for its limitations is inherent to the cameras and the camera position during

imaging acquisition. The spatial resolution of the imaging system deteriorates due to the distance between the camera and the object. Along with the degradation of spatial resolution, the general-purpose cameras, designed for whole body imaging, have a large field-of-view. This large FOV can see much of the background from the torso, including hot regions like the heart and liver, which can further blur images. Conclusions of studies comparing mammography to scintimammography reference that cameras with smaller FOVs that center on the breast and chest wall with high resolution could improve imaging performance Khalkhali et al. (1995); Taillefer et al. (1995); Villanueva-Meyer et al. (1996); Prats et al. (1999). This need for breast-specific cameras drove many of the advances in NBI during the turn of the millennium.

1.4.3.2 Breast Specific Gamma Imaging

Breast-Specific Gamma Imaging (BSGI) is a technique currently commercialized by Dilion Technologies (Newport News, VA). Similar to scintimammography, BSGI uses a radiotracer, specifically ^{99m}Tc-MIBI. The key advantage to BSGI over scintimammography is the use of specific radiation detection cameras that have been optimized for the breast (Majewski et al., 2001; Kieper et al., 2003; Garibaldi et al., 2006). These breast specific cameras sit much closer to the body in similar fashion to mammography systems, thus recovering much of the sensitivity and spatial resolution lost in scintimammography. The imaging geometry in practice is shown in figure 6. With light compression applied, short lesion-to-detector distances can

Figure 6: A photograph of a woman undergoing a BSGI scan using the Dilon 6800 system. Photo reproduced from Dilon Diagnostics at www.dilon.com.

improve image quality while acquiring projections similar to those of mammography. The small field-of-view cameras in BSGI also employ the scintillation detector technology described for scintimammography. However, BSGI cameras employ multiple 10 mm thick NaI(Tl) crystals that are separated by thin reflective septa. This pixel-based scintillation camera approach does not suffer from edge effects as the monolithic crystals used in general-purpose cameras (Brem et al., 2002).

Patient studies using breast-specific cameras have quoted higher sensitivity for detecting breast cancer over other imaging modalities. In the pilot study of a BSGI system, 50 patients with 58 tumors were scanned for breast cancers with both general-purpose cameras and an array of 3 mm $\times$ 3 mm $\times$ 10 mm NaI(Tl) crystals optically coupled to position-sensitive PMTs, referred to as High-Resolution Breast-specific Gamma Camera (HRBGC). Results of the study found that the HRBGC outperformed the scintimammography camera by detecting 78.6% (22/28) of all malignant tumors versus 64.3% (18/28) with equal specificity for benign tumors. The salient

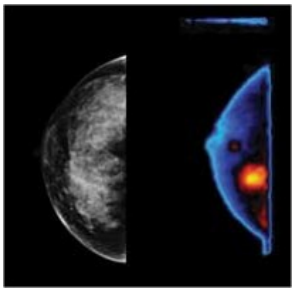

Figure 7: Comparable images of the same patient with mammography and BSGI. BSGI is capable of localizing high metabolic activity, providing clearer visualization of potential disease than standard mammography. Photos reproduced from Dilon Diagnostics at www.dilon.com.

point made in the study was that the HRBGC found 4 tumors less than 1-cm in diameter that were left undetected by the general purpose camera (Brem et al., 2002).

In other patient studies, the BSGI systems of Dilon Technologies were used as adjunct modalities in the determination of benign and malignant breast tumors. In 2005, a study was released where 94 high risk women between the ages of 36 and 78 years young with normal mammograms underwent scintimammographic exams. Those who had abnormal results from BSGI had cancer confirmed with ultrasonography (US) or biopsy. Results showed that 16 women with normal mammograms had some abnormal finding. In 14 of those cases, findings of benign tumors were confirmed with US or biopsy, while two cases had invasive carcinoma under 1 cm in size diagnosed with US-guide biopsy (Brem et al., 2005). A retrospective review of 146 women undergoing BSGI and biopsy has also been performed. Out of 167 lesions, BSGI detected 80 out of 83 malignant tumors for a sensitivity of 96.4%. Of the other 84 benign tumors, BSGI confirmed 50 of them for a specificity of 59.5%.

However, even with high sensitivity and moderate specificity, approximately 30% of abnormal results were false positives and 3 (∼5%) true negatives were not detected. Of great importance, BSGI accurately identified 16 of 18 cancers under 1 cm in diameter. Thus, an argument can be made that using breast specific gamma cameras can detect early stage cancers with high sensitivity (Brem et al., 2008).

The performance of the cameras of BSGI is intrinsically limited by the performance of scintillation crystals. NaI(Tl) has been the industry standard for radiation detection, however, its properties are not ideal for medical imaging. One disadvantage of NaI(Tl) is its fluorescence time of approximately 230 nanoseconds, which limits the level of radioactivity that can be measured. Another limitation in scintillator performance is the process of converting optical photons to a measurable electrical signal. On average in scintillators, 100 eV is required to create a single charge carrier. In addition, the poor light collection yield of the PMT can play a role in the degradation of energy resolution. Ultimately, these processes limit the energy resolution of NaI(Tl). A general assumption about detector response is that the energy input is typically linear to its output, which validates the theory that the peak centroid is proportional to the number of charge carriers created per ionization event. If the FWHM stays relatively constant, then the energy resolution could be improved with use of a material that creates more charge carriers per event (Ter-Pogossian and Phelps, 1973; Knoll, 2000).

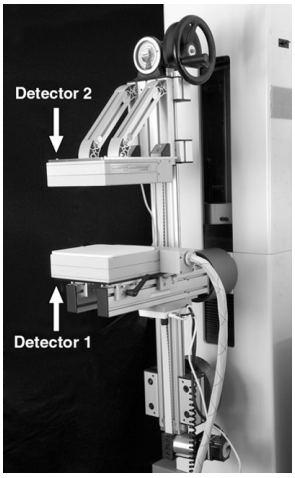

Figure 8: A photograph of the MBI dual-head system, the LumaGem 3200S, which utilizes CZT detectors. Photo reproduced from Hruska et al. (2008).

1.4.3.3 Molecular Breast Imaging

Molecular Breast Imaging (MBI) is another NBI technique whose investigation is led by the Mayo Clinic. It is currently marketed not as a replacement for x-ray mammography, but as a diagnostic technique when mammograms are inconclusive. MBI utilizes dedicated small field of view gamma cameras for detecting breast cancer. The design and technology used in MBI is very similar to the techniques of BSGI, however, MBI employs the room-temperature semiconductor Cadmium Zinc Telluride crystals instead of conventional scintillation crystals. An example of a modern MBI system is the LumaGem 3200S, shown in figure 8.

The initial question that the Mayo Clinic addressed was the role of energy resolution for NBI. As previously stated, semiconductors have superior energy resolution over scintillators, but does the improvement in energy resolution truly translate into improved image quality and detectability of cancer? In theory, the better energy

resolution of CZT should provide better scatter rejection capabilities and separation between primary photons that do not undergo scatter and scattered photons, which have lost energy and their original position information. Exclusion of these scatter photons could reduce its contribution to background levels and improve contrast.

Using pixellated CZT modules, two studies were conducted to investigate energy resolution's role in NBI. In their first study, the performance of two NaI and CsI scintillation imaging systems was compared to a prototype CZT system and a commercial CZT system. A breast phantom with four spherical hot spots of various sizes representing tumors was employed to acquire images. The energy resolutions of the two CZT systems were 17.5% and 5.8% at 140 keV and energy windows from ±10% to -5%/+10% were used for creating images with 250,000 counts. Results showed that the CZT systems outperformed the NaI and CsI systems in terms of detectability and tumor contrast of hot spots. However, tumor contrast was similar between the two CZT modules of differing energy resolution. Contrast did improve when narrower energy windows were utilized (Hruska and O'Connor, 2006a).

The second study modeled an MBI experiment in simulation. A CZT camera, comprised of 96 × 128 1.6 mm × 1.6 mm × 5 mm thick pixels, had its energy resolution vary from 20% to 3.8% at 140 keV to image a half cylindrical breast/torso phantom with three tumors placed close to the chest wall, in the center of the breast and close to the surface. Influenced by previously conducted patient studies, activity concentrations of the breast, tumors and torso organs were modeled. Tumor to

Background ratios varied from 10:1 and 5:1 with varying depths of tumors within the breast. To make the performance of pixilated CZT more accurate, its tailing effect was also modeled. Simulation results confirmed that varying the energy resolution had little effect on the tumor contrast. The authors theorize that this is due to the low levels of scattered photons that contribute to the images. Without great amounts of scatter, the superior energy resolution of CZT goes unutilized (Hruska and O'Connor, 2008a).

The Mayo Clinic evaluated CZT imaging systems for MBI applications. One of their original designs used a single head camera with field of view of 20 cm $\times$ 20 cm, using 6400 pixels with dimensions of 2.5 mm $\times$ 2.5 mm and 5 mm thick. The detector was equipped with either a general-purpose collimator (35 mm long bore) or a 50 mm long bore collimator, both with square holes of 2.3 mm $\times$ 2.3 mm and 2.5 mm pitch. The system was evaluated for detectability of tumors of various sizes (<1 cm) and tumor to background ratios in breast phantoms and in clinical studies. When performance was compared to a conventional Anger camera, the CZT system demonstrated better contrast and sensitivity to tumors under 1 cm in diameter (Mueller et al., 2003).

Over time, the Mayo Clinic began exploring optimization methods for improving the sensitivity of breast imaging systems. This included incorporating an additional opposing dual-head CZT imaging. In simulation, the group developed methods to use both camera heads to quantify tumor size and depth within breast given various

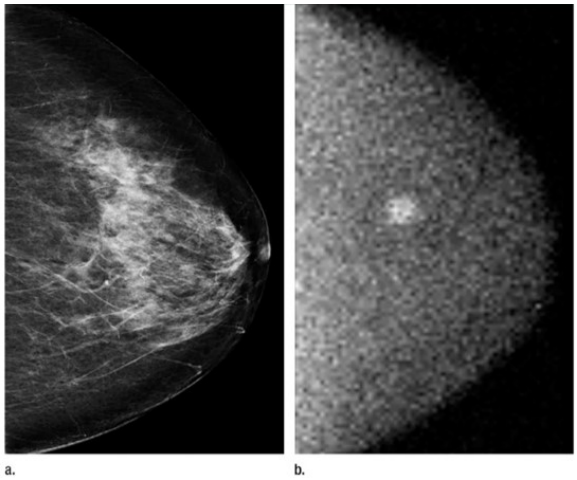

Figure 9: Direct comparison of the same breast imaged using a) standard x-ray mammography and b) MBI. The location of the breast tumor is clearly seen in using MBI, while there is some uncertainty associated with the mammogram. Images reproduced from Rhodes et al. (2011).

tumor to background ratios (Hruska and O'Connor, 2008b). In a clinical study, sensitivity to tumors under 10 mm in diameter was increased from 68% in single-head camera to 82% using the opposing dual-head system (Hruska et al., 2008). Another study provided evidence for using MBI for diagnostic imaging with screening mammography. Example images from this study are shown in figure 9. Women with mammographically dense breast underwent mammography and dual-head gamma imaging procedures and observed that combining both techniques increased the detectability of cancers in 7.5 per 1000 women screened (Rhodes et al., 2011).

From these studies, Molecular Breast Imaging excels as a technique for diagnostic breast imaging. However, there are disadvantages to the technique. One of the primary disadvantages in MBI is the low energy tailing observed in the energy spectra of CZT. This effect is due to the poor transport properties of CZT, specifically, the

holes. In contrast to an electron drift mobility of $\sim$1000 cm^2/Vs, the hole drift mobility is much worse at $\sim$200 cm^2/Vs. Corresponding $\mu\tau$-products of CZT are $\sim 3\times10^{-3}$ cm^2/V and $\sim10^{-5}$ cm^2/V for electrons and holes, respectively. These differences in the charge-carrier properties lead to trapping and recombination effects within the CZT crystals, which leads to incomplete charge collection. The amount of charge collected then registers as less than the energy of the photon that created the charge-carriers, leading to a tail on the lower energy side of the photopeak in the energy spectrum (Bolotnikov et al., 2005). The low energy tailing effect can be eliminated by utilizing smaller pixels sizes in CZT detector systems that remove the influence of hole drifting, creating an electron charge-carrier detector. Known as the small pixel effect, using CZT pixels with small sides in relation to the pixel's thickness can lessen the tailing effect and improve CZT's energy resolution (Wagenaar, 2004).

Another concern with NBI in general is the high risk of radiation exposure and absorbed dose. In annual screening digital and film mammography, there is an average glandular radiation dose of 4.2 mGy. This correlates to a Lifetime Attributable Risk (LAR) for fatal breast cancer of approximately 25 cases per 100,000 cases for women between the ages of 40 and 80 years. For NBI, the recommended injected activity of ^{99m}Tc sestamibi, the radiotracer used in NBI, is 20-30 mCi. According to this study, this level of radioactivity has a LAR of fatal breast cancer that is 20-25 times higher than the LAR for annual screening mammography in women between the ages of 40 and 80 (Hendrick, 2010). The large difference between these LAR values can be

contributed to the differences in the imaging techniques. Mammography uses x-rays that only contribute dose to the breast, while NBI uses a radiotracer that perfuses throughout the body and emits 140 keV gamma rays that contributes dose to multiple organs and tissues. Mammography is the only technique that has been proven to lower the risk of terminal breast cancer in women. It is for this reason why NBI techniques are only advertised as diagnostic tools to accompany screening mammography rather than a replacement for mammography (Rhodes et al., 2011).

In response to the high radiation dose of NBI scans, proof-of-concept studies varying the injected activity of ^{99m}Tc sestamibi down to 4 mCi were performed in phantoms and patients. Energy windows were widened (-21%/+10%) to provide additional enhancements to sensitivity. In phantoms, enhancements in contrast to noise ratio for tumors at 1-cm and 3-cm depths were observed, in addition to sensitivity gains at a factor of $\sim$3 compared to standard imaging protocols, but at the detriment of spatial resolution (Hruska et al., 2012a). In a blind observer clinical trial, similar improvements in contrast were observed in patient images. Sensitivity and specificity metrics were constant across low dose images, but evidence for increased false negatives was present (Hruska et al., 2012b).

1.4.4 Limited-Angle Nuclear Breast Tomography

Current clinical protocols use planar imaging techniques to acquire breast projections at set angles without applied reconstruction algorithms. However, select groups

are exploring limited-angle acquisition schemes to generate tomographic breast images. Limited angle tomography (LAT) refers to the limited angular sampling range around an object. The central slice theorem dictates that imaging 180° around an object fully samples fourier space. Failing to satisfy this criterion leaves portions of fourier space unmeasured which can generate artifacts in image reconstruction (Davison, 1983; Barrett, 1990). In addition, the organs within the torso would contribute greatly to projections, suppressing breast signals of interest. Therefore, LAT approaches to breast scanning may provide informative tomographic images. The following sections highlight the technology and acquisition development for dual-modality emission and x-ray systems using limited angle nuclear breast tomography.

1.4.4.1 Hybrid SPECT-CT

Progression of hybrid SPECT-CT system has been led by Martin Tornai at Duke University. This system acquires breasts tomographic images with the patient in a prone position while the SPECT and CT systems scan underneath the patient bed. Figure 10 shows a photograph of the hybird SPECT-CT system.

Initial work with the SPECT device focused on optimization of vertical axis of rotation (VAOR) trajectories around the prone breast. One major concern for these trajectories was satisfying Orlov's criterion for untruncated projection completeness. To accurately reconstruct a source volume, the arc mapped by the unit vector of the collecting parallel-hole camera must intersect every great circle on a directional

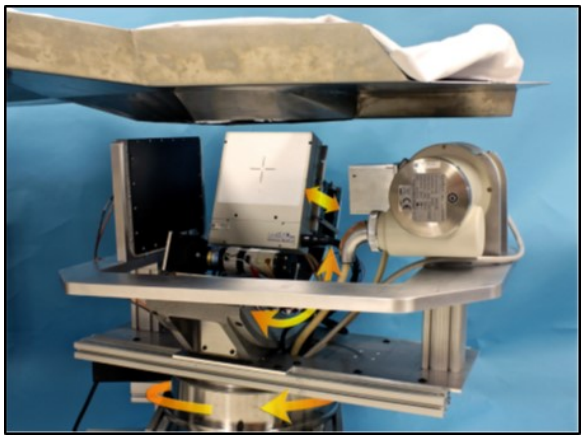

Figure 10: Photograph of the hybrid SPECT/CT breast imaging system. Patient lie in an prone position with the breast suspended in air. The gamma camera follows a path that contours to the breast shape. Picture reproduced from Cutler et al. (2010).

sphere (Orlov, 1975). Through experimental and simulated testing of various orbits with a commercial NaI(Tl) camera, it was determined that VAOR trajectories with additional orthogonal arcs using a polar-tilted camera head and larger pixels provided better contrast and SNR of hot spots within phantoms compared to planar imaging techniques (Pieper et al., 2001; Tornai et al., 2003, 2005). Applying a small number of iterations in an OSEM reconstruction algorithm provided better SNR and contrast, as these metrics were inversely correlated to iteration number (Tornai et al., 2003).

With improvements in manufacturing and stability, a CZT-based detector, the LumaGEM 3200-S, was substituted for the NaI(Tl) detector for SPECT imaging. Detector characterization and imaging performance with tilted-parallel beam (TPB) and projected sinusoidal (PROJSINE) trajectories around breast phantoms were accomplished with the CZT-based system. Results from (Brzymialkiewicz et al., 2005) concluded that TPB and PROJSINE both provide good contrast and SNR for hot

spots under 1 cm in diameter in breast phantoms. In addition, (Brzymialkiewicz et al., 2006) showed that when imaging varying breast sizes that TPB trajectories can potentially visualize smaller tumors during screening scans, while PROJSINE orbits can be more useful for imaging near the chest wall. Additional support of Brzymialkiewicz conclusions came from later work using contrast-detail and syringe phantoms. Overall, TPB orbits were better able to visualize smaller hot spots than PROJSINE orbits, but PROJSINE trajectories contained projections with a larger FOV and provided better quantification of reconstructed volumes with less blurring than TPB orbits (Cutler et al., 2010; Perez et al., 2011).

1.4.4.2 Dual Modality Tomosynthesis

The development of the Dual Modality Tomosynthesis (DMT) system has been explored through the collaborative efforts between the University of Virginia led by Mark Williams and Jefferson Labs. This system combines the functional information acquired from a BSGI scan, named Gamma Emission Breast Tomosynthesis (GEBT) and the structural information provided by X-ray Breast Tomosynthesis (XBT), a limited angle x-ray imaging technique, to better correlate and localize disease between separate x-ray and emission images without moving the patient. Figure 11 shows a version of an upright DMT system.

An initial phantom study by Moré et al. (2007) introduced and tested the first DMT system to best optimize the scanning protocol for performance. For a fixed

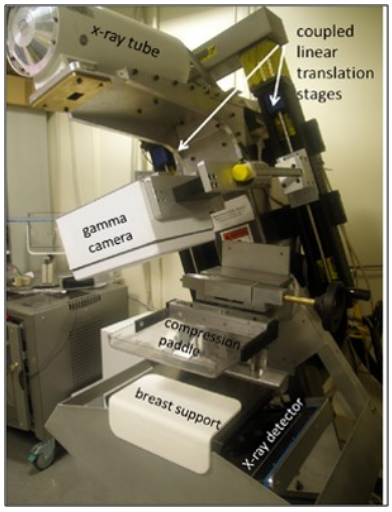

Figure 11: A photograph of the Dual Modality Tomosythesis system. The imager is capable of acquiring x-ray transmission data for tomosynthesis and functional data from the gamma camera with the breast under mild compression. Photography reproduced from the University of Virginia (http://faculty.virginia.edu/mbwlabwebsite/DualModalityTomosynthesis.html).

number of detected photons, the number of projections/views and the angular range of those projections were evaluated by calculated contrast and SNR of reconstructed images. Additionally, DMT with a dual-head gamma cameras was explored, but not utilized any further in future studies. Results suggest that a shorter angular range for the GEBT and tomosynthesis scans provide the best contrast and SNR for hot spheres, but at the cost of trans-axial spatial resolution.

In a pilot human study using DMT, 17 women with 21 biopsied lesions were scanned using XBT followed by an GEBT scan using NaI(Tl) cameras in an limited angle imaging geometry ($\pm 12°$, 13 projections) for XBT and $40°$ (5 projections) for GEBT. Lesions were classified for malignancy using histology and board-certified radiologists scored lesions based from tomosynthesis and GEBT images alone and

combined to determined performance metrics. For thresholds listed, x-ray tomosynthesis and GEBT generally had equal sensitivities, but GEBT always provided better specificity. Results showed that the better specificity provided by GEBT increases the overall performance of DMT to an accuracy of 95% while better localizing tumors (Williams et al., 2010).

In an effort to improve upon the quality and quantification of GEBT images under a limited-angle geometry, an MLEM reconstruction algorithm that utilizes a priori information was explored. Regularization was applied to object based on XBT data and attenuation and resolution recovery coefficients were used for projection operators. Using SIMIND, a Monte Carlo radiation transport simulation package, projections from a grid pattern of hot spots and a uniform object were generated to model GEBT scans and reconstructed with and without regularization, attenuation correction or resolution recovery. Compared to planar projections and previous DMT studies, accounting for these factors improved quantification of lesion activity and imaging performance improved with increased angular range, contrast to a previous DMT study (Gong et al., 2012; Moré et al., 2007).

The use of DMT has proven to be effective clinically in localizing and identifying malignant tumors. However, the reconstruction algorithm evaluated in Gong et al. (2012) as of this writing has yet to be applied to clinically acquired data. In addition, scatter correction normally accompanies attenuation correction and is noticeable absence from projection operators. The models and phantoms used in Gong et al. (2012)

did not include out-of-view activity, where scattered photons may become more of a concern for DMT. Nevertheless, DMT may potentially become a valuable clinical tool for detecting breast cancer.

CHAPTER II

GENERAL RADIATION TRANSPORT AND ANALYSIS METHODS

2.1 Monte-Carlo N-Particle Simulator

2.1.1 MCNP5 Overview

The radiation transport code used for the duration of this thesis is Monte Carlo N-Particle, version five (MCNP5) developed at Los Alamos National Laboratory and distributed by the Radiation Safety Information Computational Center (RSSIC) at Oak Ridge National Laboratory (ORNL). The MCNP5 code is capable of neutron, electron, photon, or simultaneous transport of all three particles through geometries defined by the user. The strength of this code is the extensive library of point-wise cross sectional data, which is employed to determine particle interactions. The MCNP5 code includes all of the physical processes for neutron, electronic, and photonic interactions, however, only gamma-rays in the low energy regime (< 511 keV) are simulated in this work. For that reason, neutron and electron dynamics are not considered. The physical processes included in the MCNP5 code for photons are photoelectric absorption, incoherent (Compton) and coherent (Thomson) scatter, and fluorescence. Pair production does not occur in this energy regime and, thus, is excluded.

The geometry of MCNP is defined in terms of the union, intersection and comple-

ments of first and second degree surfaces that bound 3D volumes or cells. The user defines the physical properties of the cells, including position, elemental composition, and mass density. The initial conditions for radiative transport, such as the sources particle type, emission energies, distributions and directions are also defined. Finally, the user can call a variety of tally types that output information on the particle dynamics, such as surface flux, and pulse-height spectral measurements. The documentation that accompanies MCNP5 is extensive, however, the following sections will outline the basic structure of the MCNP5 input files, which are the cell, surface, and data cards that define the geometry, source distributions and simulation outputs. It is recommended that the MCNP5 manual and other primers are consulted for further details not discussed in this document (Brown et al., 2002; Shultis and Faw, 2011).

2.1.2 MCNP5 Inputs

2.1.2.1 Surface Cards

Surface cards are the building blocks for MCNP simulation geometries. Surfaces are defined either by functions in Cartesian space $[f(x, y, z) = 0]$ or by a series of known points that lay on the surface. In this work, defining surfaces functionally is sufficient to describe all simulation geometries. Table 3 provides a few examples of simple surfaces cards that have been used in this work. Flat planes, spheres, cylinders, and other second degree shapes are called using their designated mnemonic and describing the appropriate coefficients or constants that satisfy the function.

Table 3: MCNP5 Surface Cards

Mnemonic	Type	Description	Equation	Card Input
P	Plane	General Plane	$Ax+By+Cz-D=0$	$ABCD$
PX		Normal to X-axis	$x-D=0$	D
PY		Normal to Y-axis	$y-D=0$	D
PZ		Normal to Z-axis	$z-D=0$	D
SO	Sphere	Centered at Origin	$x^2+y^2+z^2-R^2=0$	R
S		General Sphere	$(x-x_0)^2+(y-y_0)^2+(z-z_0)^2-R^2=0$	$x_0\ y_0\ z_0\ R$
C/X	Cylinder	Parallel to X-axis	$(y-y_0)^2+(z-z_0)^2-R^2=0$	$y_0\ z_0\ R$
C/Y		Parallel to Y-axis	$(x-x_0)^2+(z-z_0)^2-R^2=0$	$x_0\ z_0\ R$
C/Z		Parallel to Z-axis	$(x-x_0)^2+(y-y_0)^2-R^2=0$	$x_0\ y_0\ R$
CX		On the X-axis	$y^2+z^2-R^2=0$	R
CY		On the Y-axis	$x^2+z^2-R^2=0$	R
CZ		On the Z-axis	$x^2+y^2-R^2=0$	R

For example, a generalized sphere has the mnemonic, S, and the functional form $(x-x_0)^2+(y-y_0)^2+(z-z_0)^2-R^2=0$. To fully describe the generalized sphere, the coefficients x_0, y_0, z_0, and R are used as inputs. However, a sphere centered at the origin in Cartesian space would only need R defined, as x_0, y_0, and z_0 are known to be zero. This has another unique mnemonic, SO. Surfaces have positive and negative sides, where $f(x,y,z)>0$ and $f(x,y,z)<0$ are satisfied. For example, considering a plane normal to the X-axis (PX) at $x=3$. For MCNP, the functional form for this plane is $f(x,y,z)=x-3$. Considering the Cartesian point $(1,1,1)$, this would have a negative designation, as $1-3=-2$. This concept becomes very important in defining cells in MCNP scripts.

In addition to surfaces, an alternative way to identify cells is with macrobodies, a

short hand method for describe 3D regions, comprised of standard surfaces without explicitly defining each side. This can be accomplished with simple 3D parallelograms, cones, and cylinders. Like standard surfaces, the space within the macrobody has a negative designation, while all space outside is positive. Taking advantage of macrobodies when identifying simulation geometries can shorten the MCNP script and simplify the identification of cells. The following macrobodies described are used within this work.

RPP: Rectangular Parallelpiped, surfaces normal to major axes

RPP Inputs: $Xmin\ Xmax\ Ymin\ Ymax\ Zmin\ Zmax$

SPH: Sphere, equivalent to surface equation for general sphere

SPH Inputs: $Vx\ Vy\ Vz\ R$

where $Vx\ Vy\ Vz = x, y, z$ coordinates of center

$R =$ radius

RCC: Right Circular Cylinder

RCC Inputs: $Vx\ Vy\ Vz\ Hx\ Hy\ Hz\ R$

where $Vx\ Vy\ Vz =$ center of base

$Hx\ Hy\ Hz =$ cylinder axis vector

$R =$ radius

RHP or HEX: Right Hexagonal Prism

RHP Inputs $v1\ v2\ v3\ h1\ h2\ h3\ r1\ r2\ r3$

where $v1\ v2\ v3 = x, y, z$ coordinates of the bottom of the hex

$h1$ $h2$ $h3$ = vector from the bottom to the top

$r1$ $r2$ $r3$ = vector from the axis to the middle of the first facet

The surfaces and macrobodies described here are combined to define and identify the cell cards. Cell cards are discussed in the next section.

2.1.2.2 Cell Cards

The cell card defines the physical shape, properties, and particle track importance of an object in the simulation universe. Each cell is uniquely identified by a cell number, the material or elemental composition, and its mass density. The material can be substituted for zero to indicate a void cell with no particle track importance, such as vacuum. Each cell is defined by the surfaces that bound that region. The surfaces that encapsulate the cell are listed using Boolean logic operators that represent the unions intersections and complements of surfaces. The union operator (:) is analogous to the logical OR, while the intersection operator, an empty space ( ), serves as the

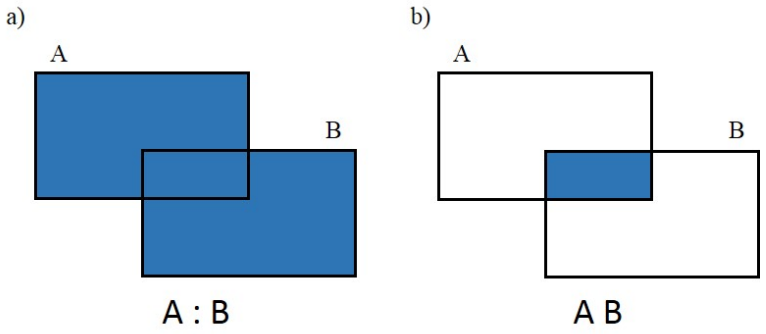

Figure 12: An schematic illustrating Boolean Operations in MCNP5. a) The union of A and B. b) The intersection of A and B

logical AND. This is best illustrated with figure 12. The command underneath each figure describes the highlighted region. The complement operator (#) is analogous to the logical NOT. Thus the statement #(A B) represents the regions that are not shared by A and B.

To illustrate how to build cell cards from a set of defined surfaces, a simple example will be considered. Figure 13 shows two concentric spheres next to a single sphere. The number inside circles correspond to surface cards and the square numbers are associated with the cells cards to be built. To start, the surfaces cards for this geometry are the following.

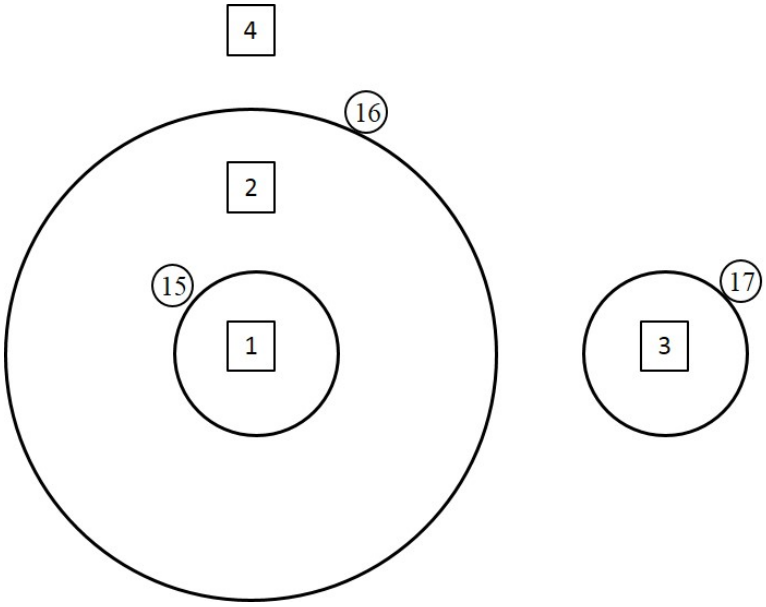

Figure 13: A simple MCNP geometry consisting of spheres. Circle numbers are surfaces and square numbers correspond to cells.

15 SO 1.25 $ 1-inch diameter sphere at origin surface

```
16      SO      3.75      $ 3-inch diameter sphere at origin surface
17      S       6.25  0  0  1.25      $ 1-inch diameter sphere along X-axis surface
```

The identification numbers 15, 16, and 17 are used in the in cell cards to define the separate 3D regions. Text behind the $ are comments, ignored by MCNP. For simplicity, the spheres will be void regions with photon importance, but the region outside the spheres will have no particle importance. The easiest cells to describe are 1 and 3, as these are just the interior of the spheres.

```
1       0       -15       IMP:P=1       $ 1-inch diameter sphere at origin cell
3       0       -17       IMP:P=1       $ 1-inch diameter sphere along X-axis cell
```

Recall that the negative in front of the surfaces correspond to inside of the surfaces, where $f(x, y, z) < 0$. Cell 2 is simply the union of the outside of surface 15 and the inside of surface 16.

```
2       0       15    -16       IMP:P=1       $ 3-inch diameter sphere at origin cell
```

Finally cell 4, the region outside both spheres, is just the intersection of the outer sphere surfaces.

```
4       0       16 : 17       IMP:P=0       $ Outerspace
```

There are special cell parameter cards that allow for repeated structure capability within a simulation geometry. The purpose of these cards is to describe a set or lattice of cells only once, then define identical structures with slightly different properties based on the original set. A relevant example of this utilized in this work is defining the camera collimation, which has several identical septa and bores that

would be strenuous to describe individually. The repeated structure capability functions through the Universe Card (U), the Fill Card (FILL) and Lattice Card (LAT). Cells are given an universe designation with the U card to which those cells belong. The LAT card can be used to generate a square or hexagonal lattice of cells that can extend out infinitely within an universe. The FILL card is then used to fill another cell with the set or lattice of cells within a universe. In the case for collimation, a septum and bore cell are placed in a universe, which is used to generate a lattice of septa and bores to fill a rectangular space. These cell parameter cards simplify the process of generating repeated structures.

2.1.2.3 Data Cards

The data cards include the inputs for the problem type, source definitions, tallies, materials with element compositions, additional peripheral cards, and the problem cutoff. One noteworthy peripheral card is the Particle Track Output (PTRAC) card, which serves as the primary output for these simulations. However, the other data cards mentioned will be discussed first.

The MODE and PHYS cards are required for specifying which particles are created and tracked, and what physical processes are needed for the simulation. Both cards use any permutation of the inputs N, E, and P to signify neutrons, electrons, or photons particles. The PHYS card has addition inputs for energy and physical process cutoffs to ignore uninteresting interactions and limit computational burdens. For this

work, only photons were required for radiation transport, thus, only MODE:P and PHYS:P were called for these simulations.

The material specification card (M) is used to define the elemental composition of cells in the simulation. The inputs for the material card are ZAID values corresponding to the atomic number (Z), atomic mass number (A), an identifier (ID), which is not used in this work, and the atomic fraction or element abundance for that particular isotope. Another option for specifying materials includes calling neutron cross sectional libraries, however, these and other cards are not required for gamma ray transport. The following examples of material cards were used in this work. For natural water, the ZAID values and material abundances are

```
M1     1000   2
       8000   1
```

where 1000 and 8000 correspond to hydrogen (Z=1) and oxygen (Z=8) with 1 oxygen for every 2 hydrogen atoms. A simple material to define is High-Purity Germanium (Z=32), which is specified as

```
M2      32000   1.
```

A more complex material to model is air, which is comprised of a mixture of Carbon (Z=6), Nitrogen (Z=7), Oxygen, and Argon (Z=18) with atomic fractions of 0.000108, 0.7808, 0.209792, and 0.0093 respectively. Air can be specified in MCNP as

```
M3      6000   -0.00108
        7000   -0.7808
```

8000 -0.209792

18000 -0.0093

where the negative signs denotes atomic fraction instead of element abundances.

The most important and complex data card is the source definition, SDEF. Within the SDEF card, the user can specify the particles, energies, starting location, emission direction, and probabilities of emissions in the simulation with source variables. Table 4 shows a condense version of the source variable offered by MCNP5 used in this work. These variables can be called explicitly as a single value, as an independent distribution (D), or as a function of another variable distribution. When single values are not used, but either an independent or dependent distributions are, the source information (SI), probability (SP), and bias (SB) cards are employed to describe the distribution. Employing these variables allows for a series of source definitions, ranging from mono-energetic, isotropic radioactive point sources, or multi-energetic, collimated volumetric sources.

For this work, the majority of simulated sources are mono-energetic, volumetric, and isotropic photon emissions, where different cells or objects have different emission probabilities. Thus, a single energy emission is called using ERG equal to a single value and the PAR variable is set equal to 2, signifying only photon emission. The CEL card is used in combination with a distribution number to identify the source emission probabilities for each cell. The CEL distribution was then used as the dependent variable to identify the volumetric distribution of the sources. For example,

Table 4: MCNP5 Source Variables for the SDEF card

Variable	Meaning	Default
CEL	cell	Determined from Location and possibly direction
ERG	Energy (in MeV)	14 MeV
DIR	μ, the cosine of the angles between VEC and the direction of the source emission	μ is sampled isotropically
VEC	Refercen vector for DIR	Require unless isotropic emission
POS	Reference point for position sampling, normally center of objection	The origin: 0,0,0
RAD	Radial distance of the position from POS to AXS	0
EXT	Distance from POS along AXS	0
AXS	Reference vector for EXT and RAD	No direction
X Y Z	X-coordinate of position Y-coordinate of position Z-coordinate of position	No X No Y No Z
PAR	Particle type	1 = neutrons 2 = photons 3 = electrons

a box object, like the torso, has its source distribution uniformly defined using the X, Y, and Z source variables and providing the x-, y-, and z-range for the torso. For a spherical object, like a tumor or lesion, the POS and RAD variables are called to identify a sphere's central position and radius vector, from zero to the radius magnitude. These variables are called with FCEL, or as a function of the CEL distribution, such that the source probability within the torso and tumor depend upon the appropriate volume. In short, the spatial distribution of emission within a

cell is defined to be uniform, but its probability of emission is dependent upon the cell.

Tally cards are called to specify output information from simulations. There are numerous tallies that are useful for various applications, but related to this work, two specific tallies are pertinent. The F2 tally calculates the flux average over a surface in units of particles per centimeter squared. Employing this tally on the front and back surfaces of a detector can offer insight on the count efficiency of the detector. The F8 tally generates a pulse height distribution of energy deposited into a detector. Two cards that should be used in combination with the F8 tally are the energy binning card (E), for sorting out irrelevant low energy interactions and appropriately binning relevant energy domains, and the Gaussian energy broadening card (FT), to provide an energy-dependent energy resolution to the pulse height tally. These tallies and support cards can provide complementary information to the output and analysis of the PTRAC card.

The final cards required for the MCNP script are the history cutoff (NPS) and the random number generation card (RAND) cards. The NPS limits the number of particles to run for the simulation, such that NPS 5000 would end the simulation after 5000 generated particles. RAND specifies the random number generator used to initialize the simulations. The GEN keyword uses a type of pseudorandom number generator, while conversely, the SEED keyword can be used to specify a seed number to repeat initial conditions.

2.1.3 Particle Track Output Card

The Particle Track Output (PTRAC) card is a peripheral card that generates an ASCII or binary file that lists the entire interaction history for user-filtered events. PTRAC offers a wealth of information about particle histories that cannot be known in realistic radiation detection and measurement task. For every collision in a particle history, the Cartesian position, cell number, material, direction, energy, collision type and time of interaction for the particle is listed. Without any keyword filters placed on the PTRAC card, every particle's event history would be saved, resulting in an extremely large file with irrelevant information. PTRAC files can be limited by output control keywords such as MAX, which sets the maximum number of written event histories, or WRITE, which controls whether all event information or only position and cell numbers are written to the PTRAC output file. In addition to output control keywords, event and history filters can be placed on the PTRAC card to only store relevant events. In particular to this work, only events that deposit energy in the radiation detector are written to a file. To facilitate event filtering, the EVENT, TYPE, and TALLY filters are utilized to save necessary information for pulse-height spectra and image generation. The EVENT keyword specified that the source emission, collisions, and terminating history are written to the output file. The TYPE keyword specified that only photons are saved, and the TALLY keyword ensured that any event that contributed to the pulse height tally on the detector would write the entire event history to the PTRAC file.

The format of the PTRAC output file is nontrivial, but necessary to understand and extract the pertinent information for an event. Given the filters placed on the PTRAC card, the output file has the following format for each event.

Particle header: [Particle Number Source Flag (1000) Triggered Filter]

Source header: [Collision flag (4000 or 5000) Node Number Source Type Cell Number Material Number Number of Collisions]

Source information: [Position Coordinates Direction Vector Energy Weight Time]

1st collision header: [Collision flag (4000 or 5000) Node Number Cross Section Info Collision Type Cell Number Material Number Number of Collisions]

1st collision information: [Same format as source information]

...

nth collision header: [Collision flag (5000) Node Number Cross Section Info Collision Type Cell Number Material Number Number of Collisions]

nth collison information: [Same format as source information]

final header: [Collision flag (9000) Node Number Termination Type Branch Number Cell Number Material Number Number of Collisions]

nth collision information: [Same format as source information]

The particle header consists of the particle number, the source emission flag (1000),

and the filter which cause the event to be written to file, in this work, the pulse height tally. The source header, and most other collision headers, consists of either the collision flag (4000) or particle termination flag (5000), the type of collision, the cell and material the photon originated and a single value indicating the number of collisions in the event thus far. Source and collision information consists of the Cartesian coordinates or position of the collision, the direction the particle travels, the energy of the particle, and a time since the beginning of the current event. The nth collision header and final header have some redundant information, however, the final header has the final event flag (9000) to indicate that there are no more events listed in the particle history. After the final head and collision information, the PTRAC output file would continue with the next particle history, repeating the PTRAC format.

There is a wealth of information within MCNP5 tallies and the PTRAC that is not related to parsing the output file for generating images, including cross sectional library calls, flags for indicating interaction nodes, particle weights, and even timing information. However, the position, energy, and types of events listed in each particle history is important and required for generating energy spectra and images. Reducing the PTRAC output to imaging data requires an understanding of the PTRAC format, its included information and a method for parsing through all the particle histories. In the next section, the method and scripts for parsing the PTRAC output from MCNP5 will be discussed.

2.2 MATLAB PTRAC Parser

The program MATLAB (short for MATrix LABoratory) (The MathWorks, Inc, Natick, MA) was employed for much of the data analysis in this work. Its built-in functionality makes MATLAB a versatile tool for a range of applications, including reading ASCII files, image processing, and analysis. The MATLAB script for parsing through MCNP5 PTRAC output files has been adopted from code used by Dr. Benjamin McDonald. A generalized method for parsing the PTRAC output file for energy deposited into the detector is described.

1. Open the file for line by line reading. Skip through the PTRAC header and locate the first particle history by searching for the source header flag, 1000. Initialize a while loop that tests for the end of the file.

2. Scan/Read the source header line and save as a variable. Initialize another while loop that will test for the end of the particle history. This can be the next source header flag, 1000, or the final event header 9000. Setup an alternating scan/read line commands that reads and saves the collision headers and collision information. This should end with the termination header and collision information that follows.

3. Determine the energy deposition: For every collision event, first determine if the interaction occurred in the detector cell. If so, then in general, the energy deposition for the event is the difference between the particle energy before and after the collision. If the interaction process is a fluorescence event, then the energy deposition is zero for the event. If the collision flag has a value of 5000, then the energy deposition is the

energy for that event. Any event that follows a 5000 flag that is not accompanied by a final event flag indicates a re-emission, and thus, energy deposition is the negative of the event energy. After parsing the particle history, sum the energy deposition from each event for the total energy deposited.

Once the energy deposition is determined, energy blurring can be applied to simulate energy resolution and that final energy can be binned to generate the total pulse-height spectrum. The information within the particle history can also be used to determine other properties of the particle track, including the type and number of interactions (photoelectric, incoherent and coherent scatter), x-ray fluorescence events from shielding, and interaction locations within the detector. Once the location of flags for user-defined cells and interactions processes within a particle event are known, it is trivial to extract that information for use. The relevant properties of the particle histories for imaging that are scored for this work are discussed in the next section.

2.3 Imaging Metrics and Analysis

2.3.1 Pulse Height Spectrum

The total pulse height spectrum can be generated from binning the individual energy depositions for each particle history. Knowing the entirety of the particle track and its interactions enables us to categorize details about energy spectra that are normally occult from experimentally-acquired spectra. Within the NBI simulations,

we can investigate the nature of scatter contributions and image contamination from out-of-view sources. Scattered photons that contribute to images have lost their origin information, becoming a source of noise which could degrade image quality. Scatter order, or the number of Compton scatters outside the detector, is determined by totaling the number of incoherent interaction flags (-1) when the cell number is not equal to the detector cell number. The photon origin is indicated by the cell number within the source information line of the particle history. With this information on scatter order and photon origin, specific pulse height spectra can be plotted along with the total pulse-height spectra. Given an energy discrimination cutoff, or energy window, around the primary photopeak, scatter and torso fraction can be determined as the fraction of scattered and torso counts compared to the total number of counts within the energy window. Lower scatter and torso fraction are desired, as this signifies more accurate projections and less out-of-view contamination of collected images.

2.3.2 Image Formation

The main purpose of detecting and collecting photons is the formation of an image that describes the anatomic and functional differences within a subject. An energy window is set for events to contribute to images. For events that satisfy the energy cutoff criterion, the position of the first particle collision within the detector is taken as the event location. Spatial blurring of the Cartesian coordinates, representing

the spatial resolution of the detector, may be applied to simulate detector response or could be omitted for a detector system with perfect spatial resolution. The new coordinates of the events are binned to generate an image. For visual display, a 3×3 mean filter is convolved with projection images to highlight prominent features, however, any imaging-metric calculations are performed on initial, unfiltered images.

The method for visualizing the size and intensity of image features is accomplished by drawing line profiles through those objects. Line profiles provide a sense of relative intensity between tumor signal compare to the background of the images, as well as image noise. In essence, line profiles provide a qualitative assessment of the object contrast and SNR. Quantitative measures of tumor contrast and SNR can be found by drawing ROIs (Region of Interest) around areas of background and hot spots and calculating their average intensity. The following equations are applied to those averages to determine image contrast and SNR.

$$Tumor\ Contrast = \frac{Mean\ Tumor\ Signal - Mean\ Background}{Mean\ Background} \tag{3}$$

$$Tumor\ SNR = \frac{Mean\ Tumor\ Signal - Mean\ Background}{STD\ Background} \tag{4}$$

In general, higher contrast values correspond to detectable variations, which may be indicative of anatomical or functional changes in the subject. For SNR, the Rose criterion dictates that tumor SNR values of approximately 5 have a 100% detectability rate, while SNR values < 5 have a lower chance of detectability (Bushberg and Boone,

2002; Cherry et al., 2012).

2.4 Chapter Summary

This chapter describes the generalized simulations methods utilized in this body of work. The MCNP5 simulation package was described, covering the basic components for building and evaluating simple imaging geometries. The PTRAC card and output file are described, which enables the user to save a list of particle histories that satisfy certain conditions of interests. MATLAB is used for parsing the PTRAC output and performing analysis upon generated pulse height spectra and images. The energy spectra are broken down into scatter order and photon origin to determine the source and magnitude of scatter and artifacts. The methods for generating and analyzing images with line profiles and image contrast and SNR is also described. These methods and metrics are utilized for all projection imaging tasks. Other methods specific to a particular task are described in their chapter in which the method is applied or employed.

CHAPTER III

GERMANIUM DETECTOR CHARACTERIZATION

3.1 Introduction

For the last several years, our research group has collaborated with Pulse Height Detectors Company (PHDs Co.) (Knoxville, Tennessee) in their efforts to fabricate position-sensitive Germanium cameras for various applications. A large part of this collaborative work involves rigorous detector and camera characterization of their systems. Figure 14 shows a timeline of the HPGe systems PHDs Co. has developed in recent years. The earliest HPGe systems had attached LN_2 dewars, making it impractical for some imaging applications. Later systems substituted the heavy dewars for a mechanical cooler, reducing the weight of the detector and making it more compact. The MI4-series shifted the detector to the front and moved the electronics behind for an improved imaging geometry, but exposed wires, components and an outlying power controller made for a less than aesthetic system. The most recent HPGe detectors, the GGC-series, are general-purposed systems, entirely packaged and compactly sealed with mobile capabilities and integrated mounts for pinhole or parallel-hole collimation. These advancements have propelled these traditional spectrometers to commercially viable imaging systems.

In previous studies, our group has characterized the performance of different HPGe

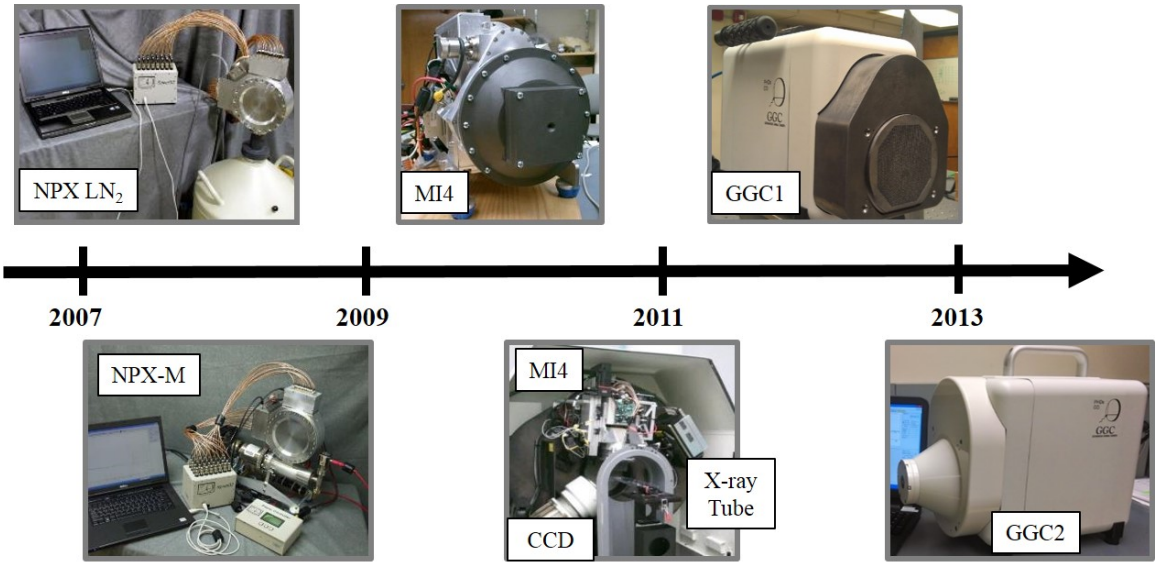

Figure 14: A timeline illustrating the HPGe systems fabricated and developed by PHDs Co. Within this time period, HPGe systems have progressed from requiring heavy LN_2 dewars attached, to compactly packaged, mobile systems.

detectors, including the NP-, MI4-, and GGC-series (Johnson et al., 2011a,b, 2012; Campbell et al., 2013). In this chapter, the characterization methods for the MI4.2 and GGC1.1 detectors are discussed, hereafter refer to as MI4 and GGC unless specified. At the time of characterization, the objectives differed between the two detectors, resulting in slight variations in performed methods between the MI4 and GGC in this document. The primary goal for characterization of the GGC was to demonstrate its imaging capability, while measurements on the MI4 are used in the development of an HPGe detector model for breast imaging (Chapter IV). Despite this, the intrinsic properties of the HPGe detectors are measured closely, but not strictly adhering, to the NEMA NU 1-2007 standards for gamma cameras, as these

standards are designed for monolithic systems (scintillators) as opposed to segmented detectors (NEMA, 2007). The intrinsic properties investigated for the MI4 and GGC are detector efficiency, spatial resolution, energy resolution, and flood field uniformity. In addition, the planar imaging capabilities of the GGC and MI4 are explored using line sources and hot spheres phantoms.

3.2 Materials and Methods

3.2.1 System Specifications

Displayed in figure 15 and 16 are the MI4 and GGC imaging systems. Even with the differences in packaging, both systems have an equivalent underlying architecture. The MI4 and GGC are cylindrical double-sided strip detectors (DSSD) with physical dimensions of 90-mm diameter and 10-mm thick. The germanium detectors are designed with a set of 16 $\times$ 16 orthogonal strips of 4.75-mm width and 5-mm pitch with 0.25-mm gaps between strips. These strip dimensions yield an active area of 55.1 cm^2. The systems have a forward-facing detector, with a mechanical cryostat capable of cooling down to 60 K, and FPGA-based readout electronics placed behind. For the MI4, a power controller box monitors all system properties, including temperature and HV bias, while digitized signals are read out through a single USB-2.0 port to the custom software, Imager32, packaged with all PHDs Co. systems. For the GGC, all data acquisition, system control, and system monitoring functions are accessed through Imager32 and the USB-2.0 port, without a separate power controller.

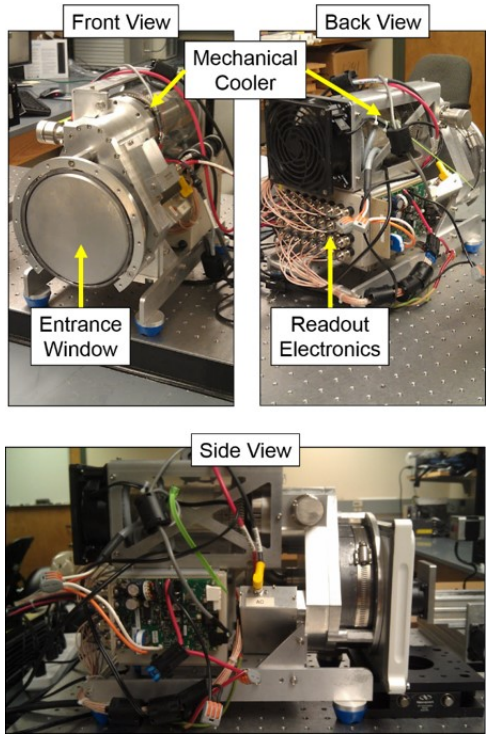

Figure 15: Photographs of the MI4 system from multiple vantage points. The components of the system are labeled, from the mechanical cooler on top, to the entrance window and readout electronics. The parallel-hole collimator lend to our group by Dilon Diagnostic can be seen in the side view photo.

An integrated assembly allows for interchangeable mounting of parallel-hole and pinhole collimators, whose designs were based on simulations for optimizing parallel-hole (Chapter V) and single pinhole collimation for small-animal imaging (Johnson et al., 2011b; Campbell and Peterson, 2011).

As described in chapter I, pulse signal analysis is applied to all events to achieve position interpolation finer than the strip width and detector thickness. Using the 50% CFD time difference on opposite side collection strips, events are sorted into 1-mm depths bins. In addition, the difference in the magnitude of transient signals

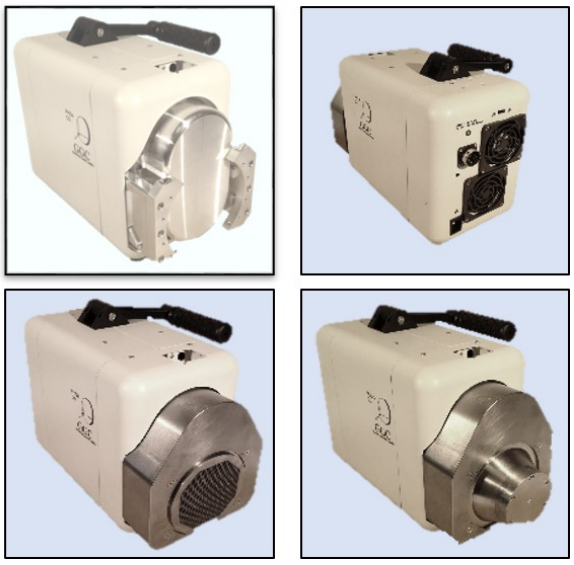

Figure 16: Images of the GGC system from multiple angles. Brackets attached to the entrance window allows for the mounting of parallel-hole collimation or a pinhole aperture. The system is completely self-contained with the mechanical cryostat, lite-readout, and a handle for mobile capability.

induced upon neighboring strips are used to estimate lateral position into nine 530-μm bins.

3.2.2 Intrinsic Detector Measurements

3.2.2.1 Detector Efficiency

Efficiency measurements were performed for the MI4 and GGC systems. For the MI4, a ^{57}Co flood source with an activity of 0.60 MBq was centered and aligned at a 50-cm distance from the detector and imaged for 12 hours to ensure good counting statistics. For the GGC, a 0.22-MBq ^{57}Co source was placed 56 cm away from the detector and imaged for over 24 hours for good statistical quality. An energy window

of ±3 keV around the 122-keV photopeak was used to determine the number of total counts (N). Equations (5) and (6) were used to calculate the intrinsic detector efficiency (ϵ):

$$\epsilon = \frac{N}{S}\frac{4\pi}{\Omega}, \tag{5}$$

$$\Omega = \frac{Area}{d^2}, \tag{6}$$

where S is the number of emitted photons, calculated from the known acquisition time, the branching ratio of 122 keV for ^{57}Co, and its radioactivity, Ω is the solid angle between the point source and detector area, and d is the distance between the source and detector.

3.2.2.2 Energy Resolution

The flood scan performed with the MI4 for intrinsic detector efficiency was also used for determining its energy resolution. Conversely, a flood illumination with multiple radinuclides was performed to measure and demonstrate the energy resolution of the GGC. Approximately 37 MBq of ^{57}Co & ^{99m}Tc, and 20 MBq of ^{123}I were placed 350 cm from the GGC and imaged for 30 minutes. An pulse-height spectrum was generated from the scan and the FWHM of the 122, 136, 140, and 159 keV photopeaks were measured.

3.2.2.3 Intrinsic Spatial Resolution

The intrinsic spatial resolutions of the MI4 and GGC were measured using the Edge Spread Function (ESF) method, similar to acquiring a pre-sampled Modulation Transfer Function in autoradiography (Giger et al., 1986). Using a tungsten block, half of the detector entrance was shielded at a known angle through the center of its FOV. A ^{57}Co flood source was placed 60 cm away from the detector and counts were acquired for 24 hours. Line profiles orthogonal to the edge response were shifted and plotted appropriately to visualize the ESF. A logistic function was fitted to the ESF and differentiated to generate a Line Spread Function (LSF). The LSF was modeled by a Gaussian function, whose FWHM was measured for the intrinsic spatial resolution. This process was completed for both the x- and y- dimensions.

3.2.2.4 Flood Field Uniformity

The flood field uniformity was measured in the useful and the central FOV for the MI4 and GGC in accordance with NEMA protocols. According to NEMA standards, acquired images require a count density $>$ 10,000 counts per cross strip.The UFOV included all collection strips with two neighboring strips, which eliminated the four bordering strips of the FOV. The CFOV was defined as 75% of the UFOV, which corresponds to removing an additional set of strips along the edge of the UFOV. Two 3-hour flood scans were performed using a 37-MBq ^{57}Co source. The first flood scan was conducted without any corrections to the data. This scan was used to generate

normalization factors to correct for non-uniformities in the entire FOV. The second flood scan then applied these corrections. The integral uniformity was calculated for both flood scans in the UFOV and CFOV using equations (7):

$$Integral\,Uniformity = \frac{max - min}{max + min} \times 100\%. \tag{7}$$

where min and max are the minimum and maximum pixel intensities of the image. The differential uniformities in the x- and y-dimensions are determined by the maximum, or worst, uniformity measurements between 5 consecutive pixels in a single row or column.

3.2.3 Camera Measurements

The parallel-hole collimator and the pinhole aperture were mounted on the detector systems to demonstrate their imaging performance. A lead low energy high resolution (LEHR) parallel-hole collimator, loaned to us by Dilon Diagnostics (Newport News, VA, USA), was placed in front of the MI4. This collimator has 1.85 mm hexagonal-shaped holes with 20-mm length and 0.3-mm thick septa thickness. The parallel-hole collimator packaged with the GGC has 1.5-mm wide hexagonal-shaped holes with 0.2-mm septa and 20-mm overall thickness. The single-lead pinhole aperture for the GGC has a 1-mm diameter aperture with a 60 degree opening angle and a focal length of 8 cm. Experiments performed with these collimators were executed based on procedures for gamma cameras outlined in the NEMA standards.

The spatial response of the MI4 and GGC was measured with their parallel-hole collimators attached. Capillary tubes with a 1-mm inner-diameter were filled with a ^{99m}Tc solution and scanned at a distance of 6.0 cm away from the MI4 and 6.7 cm away from the GGC. Projections of these line sources were acquired until more than 10^3 counts were collected in the hottest-intensity pixels. LSFs were generated and fitted to Gaussian functions from a single line source projections by summing orthogonally across three collecting strips. The spatial response of the camera was taken as the average of the FWHM and FWTM of the Gaussian fits. Measurements were made for both the x- and y-dimensions. Comparisons to the expected spatial response were made using analytic formulations for geometric (8) and total system resolution (9) given the measured intrinsic spatial resolution R_i (Anger, 1967):

$$R_g = \frac{d(l_e + x + c)}{l_e} \tag{8}$$

$$R = \sqrt{R_g^2 + R_i^2}. \tag{9}$$

Here, d is the collimator-hole diameter, l_e is the effective collimator length adjusted for attenuation, x is the source-to-collimator distance, and c is the spacing between the bottom of the collimator and the detector material, assumed to be 14.6 mm. Analytic FWTM was assumed to be 1.83 times the recorded FWHM.

One feature of these position-sensitive HPGe detectors worth highlighting is its Depth-Of-Interaction (DOI) capability. To demonstrate this attribute, projections of

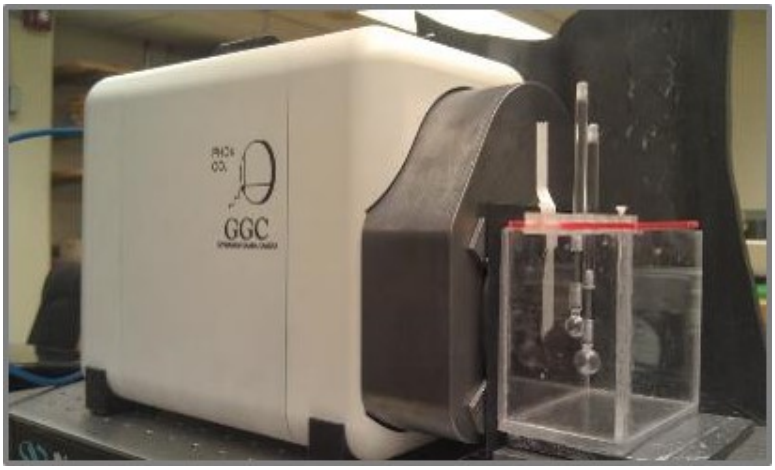

Figure 17: A photograph of the breast phantom. The 10 cm × 10 cm × 6-cm thick plastic box was designed to cover the HPGe camera FOV and mimic an average-sized breast under mild compression. The 1 mL (1.2-cm diameter) and 0.25 mL (0.8-cm diameter) spheres are suspended inside.

two capillaries on and off-axis of the pinhole collimator were acquired with the GGC. A schematic diagram of the experiment appears in figure 25a. The on-axis capillary was placed at a distance of 6.7 cm away from pinhole, while the second was positioned 3.0 cm (25°) off-axis of the pinhole. Projections of these line sources were acquired until more than 10^3 counts were collected in the hottest-intensity pixels. The line source projections were visualized as both an x, y image as well as lateral position versus depth images to demonstrate the DOI estimation capability.

One potential biomedical imaging application for HPGe DSSDs is diagnostic breast imaging. A breast phantom was developed in our lab for modeling planar breast imaging scans with the HPGe cameras (figure 17). The phantom consisted of a plastic box with dimensions of 10 cm × 10 cm × 6-cm thick and a holder to position the plastic spheres anywhere within the volume. In this experiment, two spheres with

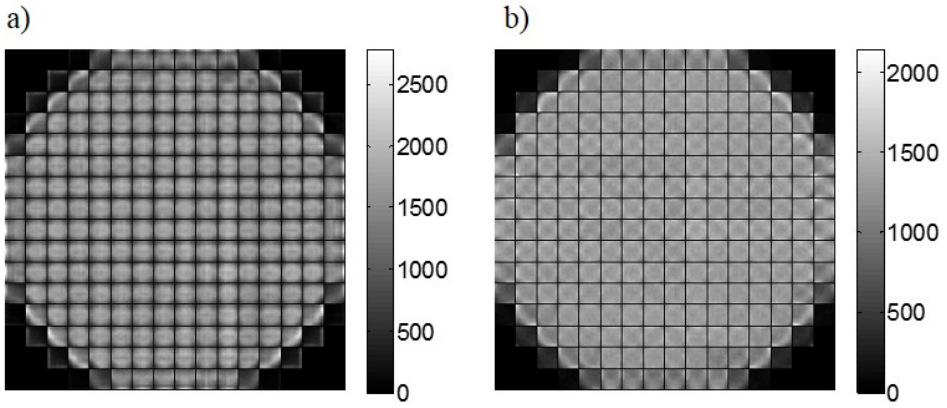

Figure 18: A projection image of the ^{57}Co flood sources acquired with a) the MI4 and b) the GGC. The cylindrical HPGe detectors exhibit an 8-cm in diameter FOV. The black lines correspond to gaps between the strips. These acquisitions employed an energy window of ±3 keV around 122 keV and was used to calculate detector efficiency.

volumes of 1 mL and 0.25 mL were placed in the phantom at a depth of 1 cm from the parallel-hole collimator with ^{99m}Tc activities of 5.9 MBq and 1.3 MBq, respectively. The phantom was imaged with three backgrounds: One with an air background, one with non-radioactive water as a scattering medium, and one with a 488-MBq background of ^{99m}Tc, modeling a tumor to background ratio of approximately 5:1. Each projection image was acquired for one minute with an energy window of ±2 keV at 140 keV with both the MI4 and GGC. Contrast and SNR values were determined by first drawing a 9×9 signal ROI centered on the hot spheres and a 27×27 background ROI adjacent to the hot sphere. Equations (3) and (4) were applied to the ROIs to calculate contrast and SNR.

3.3 Experimental Results

3.3.1 Intrinsic Detector Measurements

The projections for calculating the intrinsic detector efficiency of the two detectors are displayed in figure 18. The intrinsic detector efficiencies of the MI4 and GGC were measured to be ∼53% at 122 keV. These efficiency measurements are comparable to previously characterized HPGe detectors (Johnson et al., 2011a,b). Current pulse processing of events in these HPGe detectors only includes photons with complete deposition of charge within one cross-strip. This also includes events that may Compton scatter followed by photoelectric absorption within a cross-strip, but would exclude any events where charge collection is shared among neighboring strips on either detector side.

The pulse-height spectrum for the MI4 is displayed in figure 19 and the multiple radionuclide spectrum with the GGC is displayed in figure 20. With the MI4 detector, the two photopeaks of ^{57}Co are clearly distinguishable, a feature normally occult in detectors with poorer energy resolution. For the 122 keV photopeak, a FWHM of 1.02% is measured. With the multi-radionuclide scan from the GGC, the main photopeaks of ^{57}Co, ^{99m}Tc and ^{123}I are clearly visible. In addition, the Kα and Kβ characteristic x-ray peaks of lead are also distinguishable. The measured energy resolutions of the 122, 136, 140, and 159 keV photopeaks are 1.28%, 1.01%, 1.11% and 1.02%, respectively. The GGC capability to resolve the 136 keV secondary peak of ^{57}Co and the main ^{99m}Tc peak at 140 keV clearly demonstrates the excellent energy

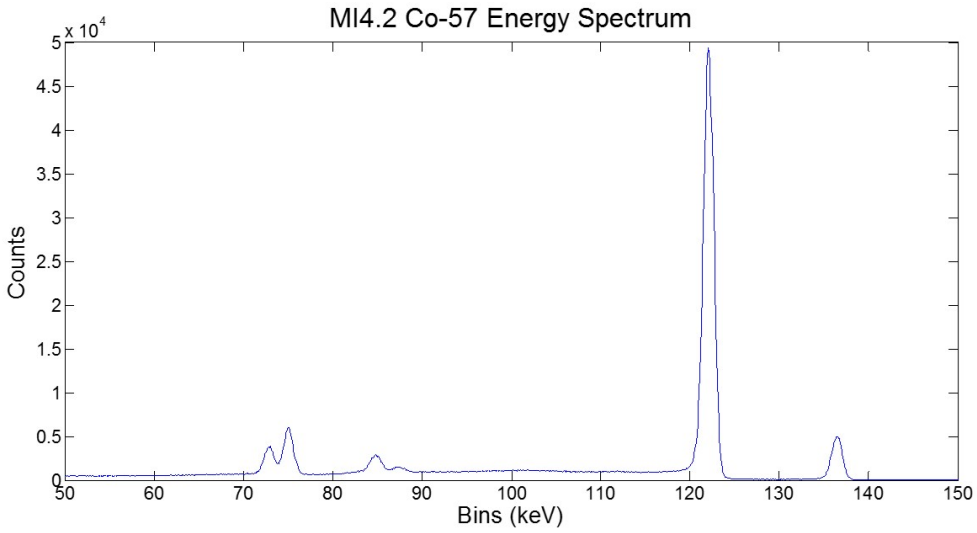

Figure 19: The pulse-heigth spectrum resulting from the flood scan of ^{57}Co with MI4. The excellent energy resolution of HPGe allows for distinguishable Kα and Kβ lead characteristic x-ray peaks, as well as separation between the 122 keV and 140 keV photopeaks, usually indistinguishable with other detectors.

resolution of the system.

Representative results of the intrinsic spatial resolution acquired using the ESF method are displayed in figure 21 and 22, including the logistic fit to the ESF data and the Gaussian fit to the LSF data. The FWHMs of the LSFs were measured to be 1.9 mm and 1.5 mm in the x- and y- dimensions for the MI4, respectively, while the intrinsic resolution of the GGC was 2.5 mm and 2.6 mm for the x- and y-dimensions, respectively.

Representative projections for measuring the flood field uniformity of the MI4 and GGC are displayed in figure 23. The calculated uniformities in the UFOV and CFOV for the uncorrected and corrected projections for both detectors are shown in Table

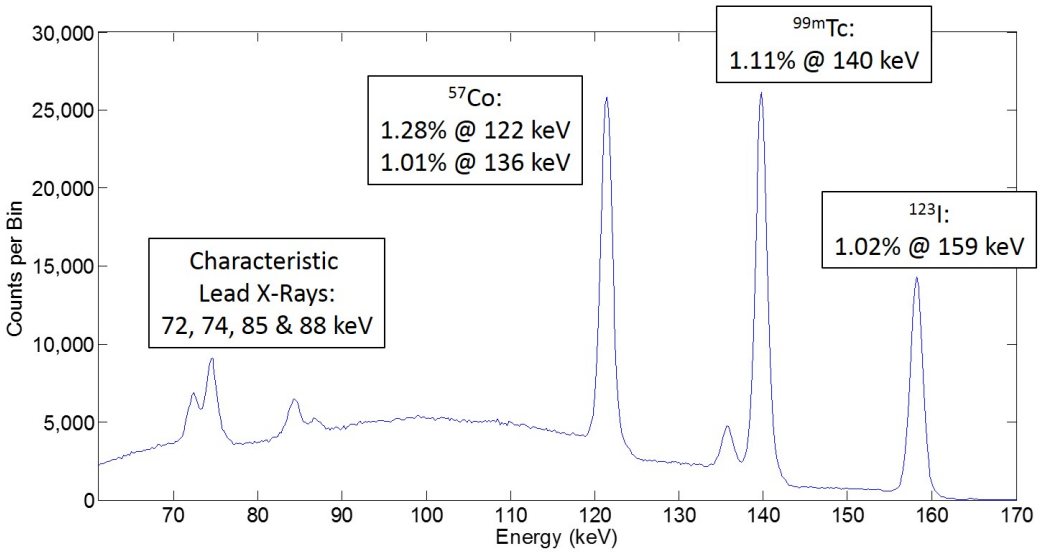

Figure 20: The energy spectrum resulting from the flood scan with multiple radionuclides. Photopeaks are identified and labeled with FWHM measurements. The excellent energy resolution of HPGe allows for distinguishable Kα and Kβ lead characteristic x-ray peaks, as well as separation between the 136 keV and 140 keV photopeaks.

Table 5: MI4 Flood Field Uniformity Measurements

	Standard Flood		Corrected Flood	
	UFOV	CFOV	UFOV	CFOV
Integral	45.90%	45.90%	5.57%	5.57%
Differential Row	29.91%	29.91%	4.13%	4.13%
Differential Column	32.54%	32.54%	3.76%	3.76%

Table 6: GGC Flood Field Uniformity Measurements

	Standard Flood		Corrected Flood	
	UFOV	CFOV	UFOV	CFOV
Integral	22.19%	17.90%	6.12%	6.08%
Differential Row	15.54%	14.75%	4.38%	4.38%
Differential Column	14.69%	14.14%	4.86%	4.79%

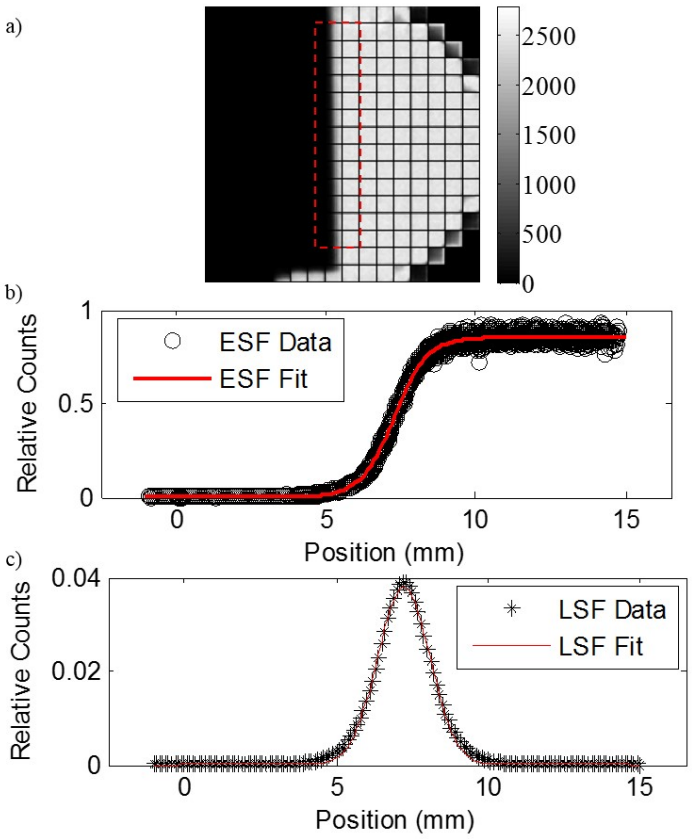

Figure 21: a) A projection image of the partially covered MI4 detector system. The dashed-line box represents the horizontal line profiles that comprised the ESF. b) The ESF dataset and its Logistic fit. c) The LSF was derived by differentiating the Logistic function. The spatial resolution was taken as the FWHM of the LSF.

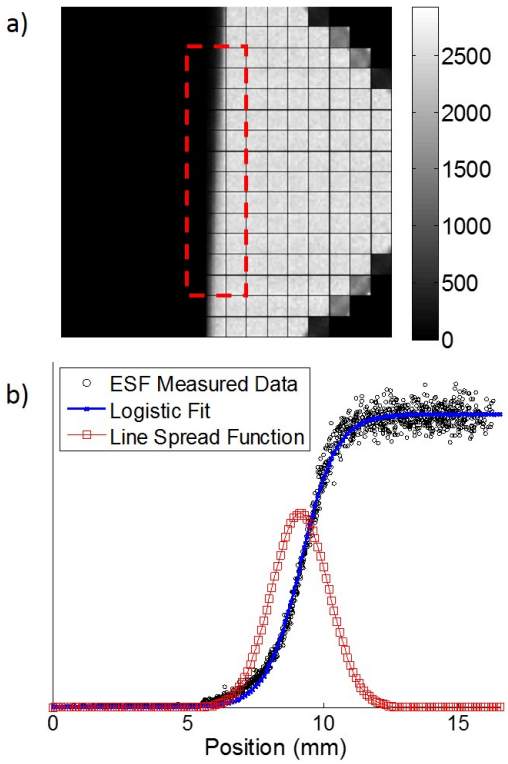

Figure 22: a) A projection image of the partially covered GGC detector system. The dashed-line box represents the horizontal line profiles that comprised the ESF. b) The ESF dataset and its Logistic fit. The LSF was derived by differentiating the Logistic function. The spatial resolution was taken as the FWHM of the LSF.

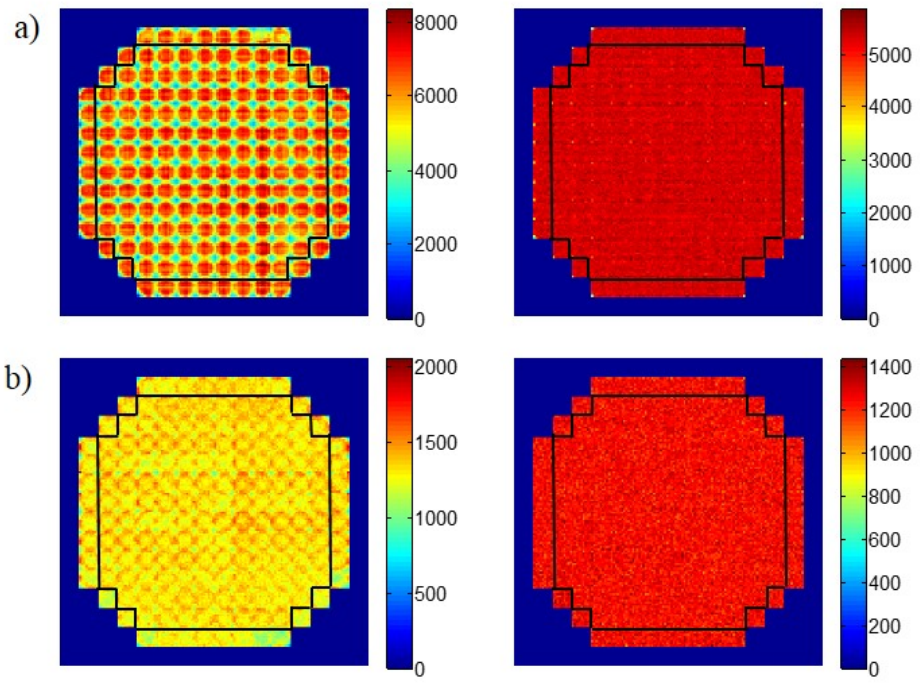

Figure 23: Processed images of the UFOV for determining flood field uniformity. Uncorrected and corrected images of the UFOV from a) the MI4 and b) the GGC. Normalization factors generated using the uncorrected image were applied to correct the subsequent flood. The solid black line outlines the CFOV within each image.

5 and 6. With applied corrections to the CFOV, integral uniformities are between 5-6% for both detectors. However, the differential uniformities for MI4 and GGC are around 4.2% in the x-direction, but an uniformity difference in the y-direction of 3.76% and 4.8% for MI4 and GGC, respectively, is observed.

3.3.2 Camera Measurements

The spatial response of the detectors with the parallel-hole collimator are illustrated in figure 24 and FWHM and FWTM measurements are listed in Table 7 and 8.

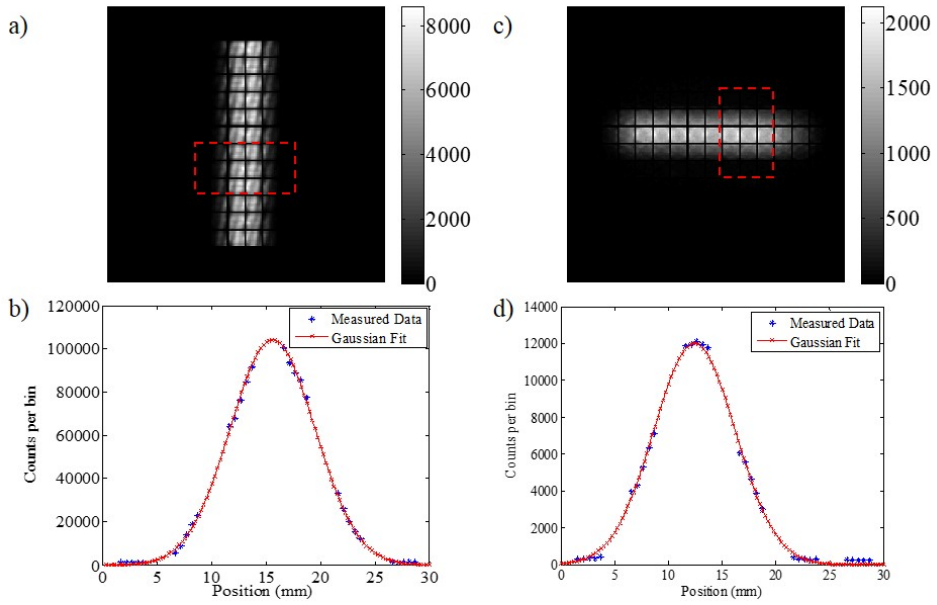

Figure 24: Projection images of capillary tubes and line spread functions demonstrating the spatial response of a,b) the MI4 and c,d) the GGC. The dashed-line box contained the vertical line profiles summed together to form a single LSF, which is fitted to an Gaussian function. The average FWHM and FWTM of the LSfs were taken for the MI4 and GGC spatial response at a depth of 6.0 and 6.7 cm, respectively.

Both detector systems exhibit a slight asymmetry in their spatial response reflected in their different spatial resolutions. Comparing the measured spatial response to the theoretical object resolution, we observe similar values for the response in the x-dimension for both detectors. However, measurements for the y-dimension exhibit less agreement with theoretical predictions, with the largest difference with the FWTM of the MI4.

The results for demonstrating the DOI capability of the GGC are displayed in figure 25b and 25c. The black lines in the depth projections represent to the gaps between the collection strips. With 1-mm depth binning, we observed an angular

Table 7: MI4 Spatial Response at 6.0 cm from the Parallel-Hole Collimator

	X-Resolution (mm)		Y-Resolution (mm)	
	FWHM	FWTM	FWHM	FWTM
Measured	9.11	16.60	9.80	17.85
Expected	9.23	16.90	9.16	16.75

Table 8: GGC Spatial Response at 6.7 cm from the Parallel-Hole Collimator

	X-Resolution (mm)		Y-Resolution (mm)	
	FWHM	FWTM	FWHM	FWTM
Measured	8.31	15.15	7.84	15.50
Expected	8.29	15.17	8.09	14.80

intensity profile from the line source placed off-axis of the pinhole. Without DOI estimation, this angular projection would appear as a blurred column of response, similar to the on-axis projection, but extended laterally.

Projections of the breast phantom with various backgrounds are displayed in figure 26 and contrast and SNR values are listed in table 9. Comparing the images of the spheres suspended in air and water, there was little to no degradation in their overall shape and size observed. When imaging the hot spheres with a warm ^{99m}Tc background, both the 1.2-cm and 0.8-cm diameter spheres were detectable above the background. Considering the Rose criterion for SNR, the 1 mL sphere would have a 100% chance to be detected, while the 0.25 mL is still visible even with a SNR < 5.0. Slight differences in contrast and SNR can be attributed to the different collimators attached to the MI4 and GGC.

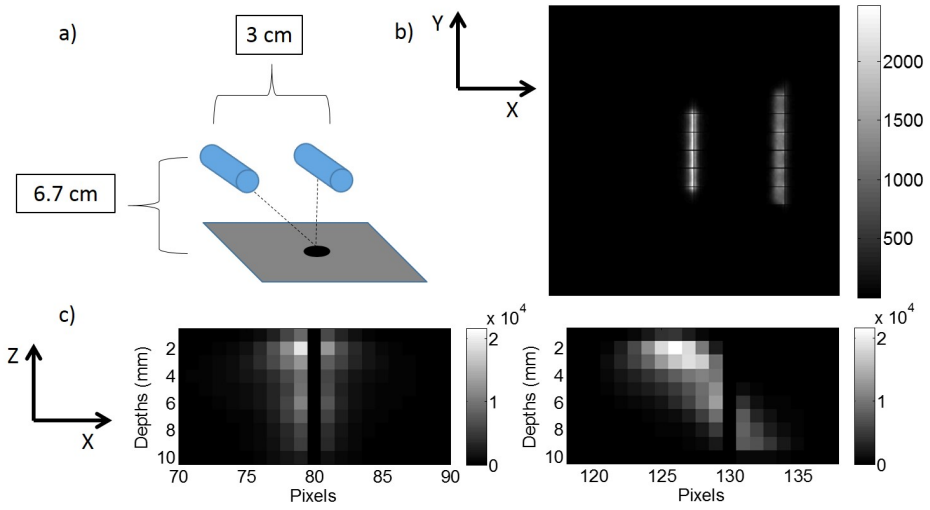

Figure 25: a) A schematic diagram of the DOI demonstration. Two ^{99m}Tc-filled capillary tubes were imaged with different lines of sight, on and off-axis of the pinhole aperture. b) The x,y projection of the two capillaries integrated over all 10 depths. c) The lateral position versus depth profiles of the two capillaries. The off-axis capillary projection exhibits a response at the same angle as the offset capillary. Without DOI estimation, the off-axis capillary would appear as an enlarged, blurred column of response.

Table 9: Contrast and SNR values for hot spheres in images of the breast phantom

	1.0 mL sphere		0.25 mL sphere	
	Contrast	SNR	Contrast	SNR
MI4	1.29	5.61	0.36	1.52
GGC	1.26	7.21	0.42	2.41

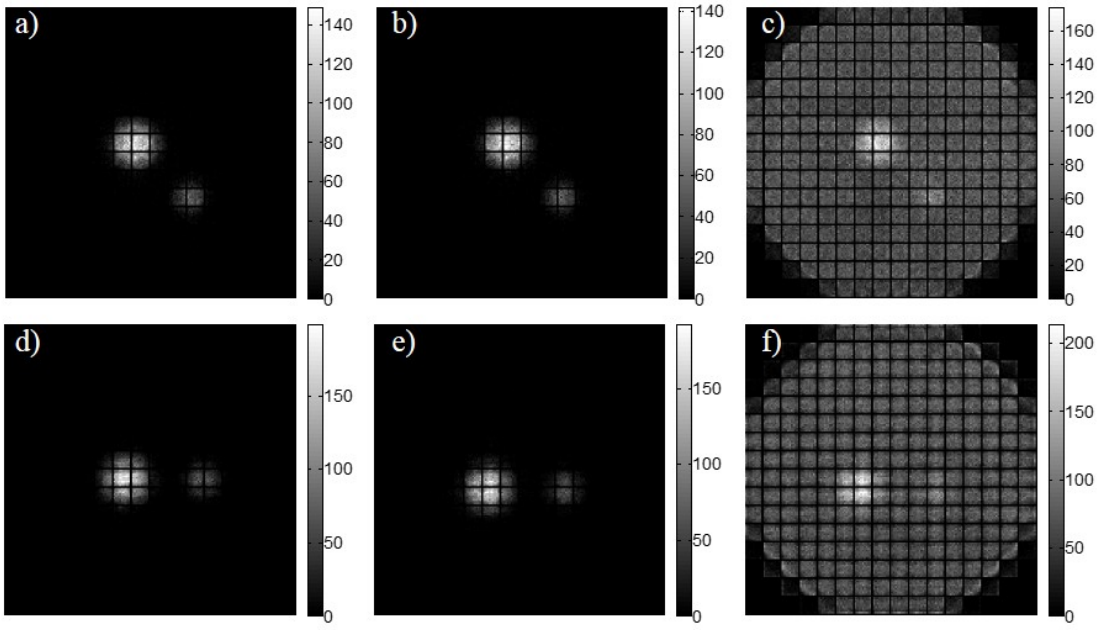

Figure 26: Projection images of the breast phantom containing 1 mL and 0.25 mL hot spheres at a depth of 1 cm from the collimator acquired with the MI4 and GGC. MI4 images with spheres a) suspended in air, b) suspended in a water scattering medium and c) with a 488-MBq ^{99m}Tc background. GGC images with spheres d) suspended in air, e) suspended in water and f) with a hot background. Very little degradation in the spatial response is observed in the presence of a water scatter medium. With a tumor to background ratio of 5:1, both hot spots are visible above background.

3.4 Discussion

The fabrication of the MI4-series of detectors signified the first steps in designing an imaging system with an optimal geometry. However, the GGC is the first version of a compactly packaged HPGe detector integrated with collimators for general-purpose use. This study strove to characterize and evaluate the intrinsic properties and imaging capabilities of these systems. One of the premier features of HPGe detectors is its excellent energy resolution. With ∼1% FWHM at relevant energies for biomedical imaging, HPGe detectors are able to resolve photopeaks separated by only a few keV. This property of HPGe detectors enables multi-isotope SPECT imaging with ^{99m}Tc- and ^{123}I-labeled radiotracers, as well as superb scatter rejection capability; demonstrated when no degradation of object size or shape was observed when imaging the breast phantom. The energy resolution allows for tight energy windows (±2 keV at 140 keV) to be utilized so that low-angle scattered photons do not contribute to acquired images.

Furthermore, HPGe detectors exhibit favorable features for single-photon imaging. Using the integrated parallel-hole collimator, the MI4 and GGC were capable of defining sub-centimeter sized spheres in a 5:1 tumor to background environment at a 1-cm depth. This finding shows the potential for use of these systems in a clinical setting. The DOI capability of the GGC may offer additional benefits for SPECT imaging by enhancing parallax recovery and improving the image quality of reconstructed images.

Even with its current performance, improvements can still be made to the HPGe detectors. The MI4 had a measured intrinsic spatial resolutions less than 2 mm in both x and y dimensions, while the GGC system currently exhibit 2.5 mm resolution. Additionally, current event analysis excludes photons that deposit energy across two collecting strips on either the cathode or anode side of the detector, which reduces efficiency. Work towards employing more sophisticated pulse processing for resolving gap and Compton scattering events is underway. Also, exploring other compact packaging configurations may offer further improvements in GGC performance.

A constant challenge of the HPGe DSSDs are the gap regions in between collection strips. Given the current pulse processing utilized with these systems, events that occur within the gaps regions are not processed, negatively impacting count efficiency. In addition, the effect of the gaps extend to the pixels along the edges of strips, which further reduces count efficiency. This is the major cause of non-uniformity in uncorrected projections, evident with uniformity values upwards of 46% and 25% with MI4 and GGC, respectively. Even in the corrected projections, Poisson statistics can only contribute to errors between 3% and 1.5%, as the mean number of counts in these images is between 1,000 and 5,000 counts per pixel. The remaining error could be attributed to the effects of the gaps, which are still observable in projections even after normalization factors are applied. It is expected that adopting inter-detector scattering event processing would improve system efficiency and uniformity while reducing the effects of the gap regions.

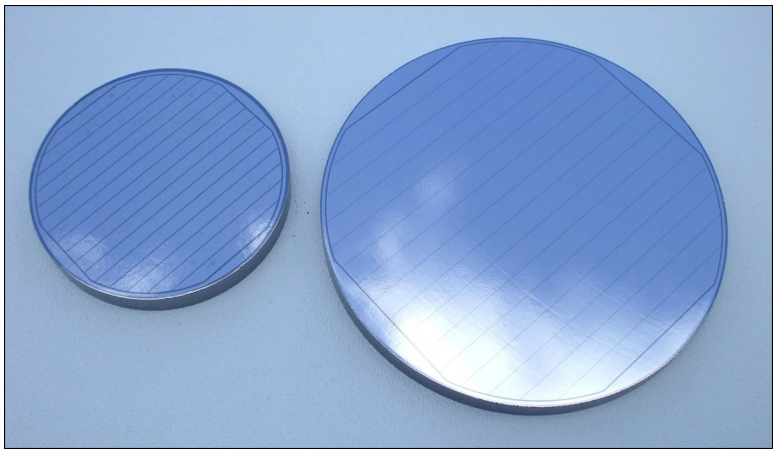

Figure 27: A photograph of the GGC1 detector crystal (left) and the new GGC2 detector crystal (right). The 14-cm diameter crystal of the GGC2 has the largest FOV of any HPGe DSSD to date.

In addition to our efforts of improving current HPGe DSSD performance, construction on the next iteration of compact HPGe DSSDs has been completed. Displayed in figure 14 is the GGC2 detector as well as the GGC1 and GGC2 crystals in figure 27. The GGC2 has a 14-cm diameter FOV, with 7.75-mm strips and gaps of 125 microns, half the size of previous HPGe detectors. The GGC2 is the largest position-sensitive HPGe detector fabricated to date. With an increase in the crystal size and a reduction of the gap width, the larger FOV of the GGC2 may afford increases in absolute count sensitivity, which could improve SNR measurements in pre-clinical and clinical biomedical imaging applications.

3.5 Chapter Summary

In this chapter, the intrinsic properties of the MI4 and GGC HPGe detectors were characterized. Energy resolutions of ∼1% at energies between 122-159 keV were

observed in pulse-height spectra. Flood scans registering only single cross-strip events revealed a detector efficiency of 53% and a corrected uniformity of ∼5% at 122 keV for both detectors. Finally, spatial resolutions of ∼1.5 mm and ∼2.5 mm were measured using the Edge Spread Function method for the MI4 and GGC, respectively. The imaging capabilities were demonstrated with a LEHR parallel-hole collimator with the MI4 and integraed parallel-hole and pinhole collimators packaged with the GGC. Camera spatial response for the GGC was approximately 8 mm for a 1-mm diameter line source at a distance of 6.7 cm away from the collimator and depth estimation with 1-mm bins was sufficient to differentiate oblique sources and demonstrate DOI capability. In addition, sub-centimeter hot spheres were detectable in a 5:1 tumor to background environment with both imaging systems. In chapter IV, the intrinsic properties of the MI4 detector will be applied to the development of a HPGe breast imaging model.

CHAPTER IV

INVESTIGATING POTENTIAL BENEFITS OF GERMANIUM CAMERAS FOR BREAST IMAGING

4.1 Introduction

Mammography has long been the standard technique for the screening and detection of breast cancer. However, mammography performance deteriorates when imaging denser breast tissue (Rosenberg et al., 1998). Nuclear Breast Imaging (NBI), also referred to as Scintimammography, Molecular Breast Imaging (MBI) and Breast Specific Gamma Imaging (BSGI), is a technique that utilizes specifically designed gamma cameras to image the distribution of ^{99m}Tc-sestamibi, which exhibits higher uptake in malignant tissues than healthy tissue (Delmon-Moingeon et al., 1990). These techniques have less dependence on tissue density and higher sensitivity than mammography for the detection of sub-centimeter diameter tumors (Garibaldi et al., 2006; Tornai et al., 2004; Mueller et al., 2003; Robert et al., 2011; Judy et al., 2010).

One benefit of using semiconductor detectors for NBI is that their superior energy resolution (ER), compared to scintillators, allows for better separation of scattered photons from primary counts. Cadmium Zinc Telluride (CZT) is a room temperature semiconductor, typically pixilated into millimeter-scale elements, that has seen use in biomedical imaging (Mueller et al., 2003; Robert et al., 2011). Utilizing small pixel

[0]The work in this chapter has been published in the IOP journal, Physics in Medicine and Biology. The text of this chapter has been altered to fit the context of this document.

sizes for CZT provides good spatial resolution while also diminishing the contribution of holes to the signal generation (small-pixel effect), thereby reducing its low-energy tailing (Barrett et al., 1995). Current CZT imaging systems offer ER of ∼4% FWHM at 140 keV, compared to Sodium Iodide scintillators which offer ∼10% ER at 140 keV (Mueller et al., 2003; Robert et al., 2011).

High-Purity Germanium (HPGe) detectors offer the best ER of any conventional radiation detector with ∼1% FWHM at 140 keV (Johnson et al., 2011a). However, these detectors require cooling to liquid nitrogen temperatures for optimal performance, making a compact imaging system for clinical and pre-clinical settings unrealistic in the past. Recent technological advances have given rise to compact, mechanically cooled HPGe gamma cameras that do not require bulky liquid nitrogen dewars. We have worked with an HPGe detector of 10-mm thickness that offers ∼1% ER at 140 keV and ∼1.5 mm intrinsic spatial resolution (Johnson et al., 2011b). While this particular detector does not have a sufficiently large active area for NBI, in this work we investigate whether an HPGe detector of this type might offer benefits for NBI.

One area in which improved detector performance might enhance lesion detection is adjacent to the chest wall, where out-of-field activity is high and small-angle scatters from the heart and torso can end up in breast images. In theory, better scatter rejection should improve image quality and the visibility of lesions in close proximity to the torso and heart. While it has been argued that the scatter content in NBI is small enough that the ∼4% ER at 140 keV of CZT does not greatly improve image

contrast compared to detectors with worse ER (Hruska and O'Connor, 2006a), the even narrower energy windows afforded by the ∼1% ER of HPGe might offer some benefit. Furthermore, HPGe, unlike CZT, does not suffer from low-energy tailing, so there is potential also for enhancements in sensitivity compared to CZT due to the higher photopeak fraction. The main objective of this work is to investigate whether the better ER offered by HPGe might translate into improved breast imaging performance. We conduct simulations to compare the imaging performance of HPGe and CZT systems. To ensure accurate results from the simulations, the intrinsic properties and performance of the HPGe detector are validated experimentally using a compact HPGe camera.

4.2 Monte Carlo Model Development

Measurements of the intrinsic properties of the MI4 HPGe detector were used as inputs for our Monte Carlo model (See chapter III). The Monte Carlo N-Particle (MCNP5) package was used to conduct simulations (Brown et al., 2002). Its PTRAC card records the event history, including interaction positions, interaction types, propagating direction, and deposited energy, of particles that meet selected criteria. This information was used within a MATLAB (MathWorks, Inc.) parser script for the generation of energy spectra and, subsequently, planar images from events falling within chosen energy windows.

4.2.1 HPGe Camera Model

For these simulations, we modeled our HPGe detector following the simulations of a CZT-based imaging system described in Hruska and O'Connor (2008a) and the architecture of the MI4 HPGe detector. The LumaGEM (Gamma Medica, Salem, NH) CZT system contained a matrix of 96 × 128 CZT pixels with dimensions of 1.6 mm × 1.6 mm × 5 mm each for a total active area of 15 cm × 20 cm. Surrounding the detector was 4-mm thick lead shielding, and a 4-mm thick lead compression pad was located on top of the breast. For this study, we maintained the 15 cm × 20 cm active area of the CZT detector, the lead shielding and compression pad, but swapped the CZT for an HPGe detector, which includes an aluminum entrance window and a vacuum inter-detector space.

We modeled the 1-cm thick HPGe detector with 0.50-mm by 0.50-mm pixels within the 15-cm × 20-cm active area. The collimator used was a conventional low energy high resolution (LEHR) parallel-hole collimator with hexagonal shape, 1.85-mm hole-diameter, 0.3-mm septal thickness and 20-mm bore length. Event positioning was determined as the first interaction within the camera model. No explicit modeling of the strip readout or the gap regions between strips was performed. Spatial blurring was added to the model on an event-by-event basis using a Gaussian distribution for the x- and y-dimensions prior to binning. The FWHMs of the Gaussian blurring functions were the measured ISR of the MI4 in the x and y dimensions. To compare HPGe and CZT images, the HPGe projections measured were rebinned to 1.5-mm ×

1.5-mm pixels by summing 3 × 3 groups of the original 0.50-mm × 0.50-mm pixels.

A model for determining the energy-dependent energy blurring for energies under the primary emission of ^{99m}Tc is required for accurate energy spectra and subsequent images. The energy resolution for energies below 140 keV was estimated using (10) for events that lost energy due to Compton scatter within the collimator, HPGe detector or phantom:

$$FWHM(E) = E_{Res} \times E \times (\frac{140}{E})^{\frac{1}{3}}. \tag{10}$$

E_{Res} is the experimentally measured energy resolution at 140 keV (described in section 4.2.2) and E is the absorbed energy from an event measured within the modeled detector (Hruska and O'Connor, 2008a). An energy-dependent Gaussian blurring function, shown in (11), was applied to the absorbed energy to determine the total energy recorded:

$$Total\ Energy = Randn \times \frac{FWHM(E)}{2.35} + E. \tag{11}$$

Randn is a random number selected from a normal distribution within the MATLAB script. The total energy was parsed into 0.25-keV bins to generate energy spectra.

4.2.2 Experimental Validation

To determine an appropriate energy resolution for the simulated detector model and validate the energy-dependent energy blurring, a flood illumination using a ^{99m}Tc

volumetric source was performed with the MI4. An activity of 720 MBq was mixed in ∼600 mL of aqueous solution inside a plastic box with length and height of 10 cm to cover the FOV of the detector. The energy spectrum was experimentally measured and the FWHM of the generated 140-keV photopeak was calculated for use in the HPGe model. The same procedure was followed in simulation, using the energy-blurring and HPGe camera models, to generate comparative energy-spectra.

We also validated our HPGe model by comparing the planar sensitivity between the MI4 camera and simulated HPGe camera. The planar sensitivity was acquired based upon procedures outlined in the NEMA standards for characterizing gamma cameras (NEMA, 2007). A petri dish with an inner diameter of 8.6 cm was filled with a thin volume of aqueous ^{99m}Tc with 142.45 MBq of radioactivity. The petri dish was oriented parallel to the camera, placed 10 cm away and imaged for 300 seconds. The same experiment was conducted in simulation with a total of 3.424×10^{10} emitted photons, equivalent to imaging 142.45 MBq of ^{99m}Tc for 240 seconds. Planar sensitivity was determined from the experiment and simulation by summing over counts within equal-sized ROIs in the resulting images and applying (12) for the decay-corrected count rate Rt,

$$Rt = Ct \times exp\left(\frac{(T_{Start} - T_{Cali})\, ln(2)}{T_{Half}}\right) \times \frac{ln(2)}{T_{Half}}\left(1 - exp\Big(-\frac{T_{Acp}}{T_{Half}}\, ln(2)\Big)^{-1}\right), \quad (12)$$

where Ct is the total number of counts in the image, T_{Start} is the start time of the scan, T_{Cali} is the time of activity calibration, T_{Acq} is the scan duration, and T_{Half} is

the half-life of ^{99m}Tc at 21672 seconds. The planar sensitivity, S, was calculated with (13) using the calibrated activity, A_{Cali}, and the results from (12),

$$S = \frac{Rt}{A_{Cail}}. \tag{13}$$

Finally, we validated our HPGe model by comparing the measured total system resolution (combined collimator and detector resolutions) of the MI4 camera to both the simulated resolution and the expected resolution given by analytic calculations. Methods for measuring total system resolution closely followed procedures outlined in the NEMA standards for characterizing gamma cameras (NEMA, 2007). A capillary tube with an inner-diameter of 1.1 mm was filled with an aqueous ^{99m}Tc solution and imaged parallel to the anode and cathode strips from 1 cm to 5 cm distance in 1-cm steps from the collimator face. The same acquisitions were simulated using the HPGe model to generate corresponding projections. Line spread functions of the capillary projections were fit to Gaussian functions to determine averaged FWHM and FWTM for both the experimentally measured and simulated data. To calculate the theorized system resolution, the geometric resolution R_g (Anger, 1967) for parallel-hole collimation was employed and added in quadrature to the ISR, R_i, as shown in (8) and (9). Percent error between the simulated and experimental system resolution at each collimator to capillary distance was calculated and averaged to determine agreement between the simulation model and the HPGe camera.

In the case that the model and camera total system resolution do not agree, ad-

justments to the model must be considered. To compensate for the HPGe model's underestimation of the total system resolution, we increased the simulated ISR in the y-direction to yield the appropriate system resolution. This was calculated by averaging the quadrature differences between the measured FWHM and FWTM from the geometric resolutions for the five measurements at different depths. With matching energy spectra, planar sensitivity, energy and spatial resolution to the MI4 camera, our HPGe breast imaging model is expected to accurately simulate the imaging performance for a clinically-relevant NBI task.

4.3 Nuclear Breast Imaging Simulations

4.3.1 Breast Phantom Parameters

To reiterate, the objective of this work was to investigate whether the better ER offered by HPGe might translate into improved breast imaging performance. We modeled a breast and torso water phantom for the simulation based on the description in Hruska and O'Connor (2008a). The half-cylindrical breast had a thickness of 5.5 cm and a radius of 9.6 cm. Adjacent to the breast was a 20 cm $\times$ 20 cm $\times$ 12.5 cm box representing the torso, which contained a cylindrical heart and the top portion of a cylindrical liver with heights of 9 cm and 14 cm, respectively, and radii of 3.50 cm and 5.25 cm, respectively. The torso and liver objects were truncated to expedite the simulations. The breast contained three 1-cm diameter spherical tumors located near the chest wall at the edge of the FOV of the detector, in the center of the breast,

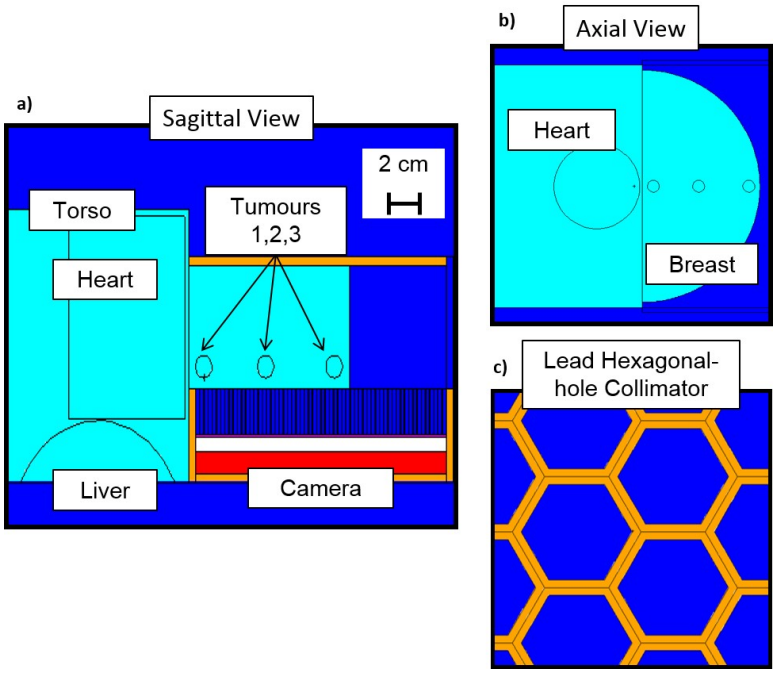

Figure 28: A schematic diagram of the geometry for the Monte Carlo simulation. a) A sagittal view of the detector (red) and the breast/torso phantom (light blue) with 3 spherical tumors. Four-mm thick lead shielding (orange) surrounds the camera and a 4-mm thick lead pad simulates light compression of the breast. b) Axial view of the breast/torso phantom with the heart and three spherical tumors. c) Axial view of the lead hexagonal parallel-hole collimator.

and near the outer edge of the breast. The tumors were either located 1 cm from the camera with a tumor-breast radioactivity concentration ratio (TBR) of 5:1 or 4 cm from the collimator with a TBR of 10:1. All tissues were treated as water. A schematic diagram of the imaging simulation is shown in figure 28. Radioactivity concentrations for the organs were set from clinical studies for uptake of ^{99m}Tc-sestamibi following Hruska and O'Connor (2008a) and appear in table 10.

Table 10: Source definitions for the breast/torso phantom.

Organ	Volume (mL)	Activity Concentration	Emission Probability
Liver	254	80	0.66
Heart	250	15	0.17
Torso	4259	1	0.13
Breast	796	1	0.02
Tumor	0.524	5	8.5×10^{-5}
		10	1.7×10^{-4}

4.3.2 CZT Camera Model

To compare imaging performance between detectors with different energy resolutions, we benchmarked the HPGe detector against the performance of a CZT-based system. The CZT camera was modeled partly from its description in Hruska and O'Connor (2008a) with slight differences from the LumaGEM system briefly described in section 4.2.1. To keep the simulated CZT model design similar to the HPGe model, the same architecture of the MI4 detector was used for the CZT model, including the LEHR collimator, aluminum entrance window and inter-detector vacuum space. An energy resolution of 3.8% at 140 keV was used with an ISR of 1.6 mm (Pani et al., 2006). CZT exhibits a low-energy tailing effect arising from incomplete charge collection due to its poor transport properties (Wagenaar, 2004). Previous work suggests that randomly subjecting 60% of events to tailing best matches experimentally acquired energy spectra (Hruska and O'Connor, 2008a). The distribution for the tailing effect was empirically created by matching simulated energy spectra of a 140 keV source to experimental data. The experimental CZT spectrum was obtained from

published material (Hruska and O'Connor, 2008a), while the simulated spectrum was created from an MCNP5 simulation of an isotropic 140-keV point source. The tailing distribution was then created from the difference in relative counts between the observed and simulated spectra, both of which were normalized, in each energy bin. This tailing model was applied on an event-by-event basis to determine measured energy within the detector.

4.3.3 Simulation Measurements and Analysis

Ten independent simulations of 3×10^{10} generated photons each were conducted for both systems and tumor parameters, equivalent to imaging 49.95 MBq of ^{99m}Tc activity within the water phantom for 10 minutes and yielding clinically relevant count densities of approximately 1000 counts/cm^2 in standard CZT images with a $\pm$10% energy window. Simulated energy spectra parsed by scatter order, the number of scatters within the phantom, and event origin were generated for the CZT and HPGe models. We generated planar images from events falling within energy windows of $\pm$10% and an asymmetric 15% energy window from -5% to +10% for CZT, similar to Hruska and O'Connor (2008a), and energy windows of $\pm$2.5% and $\pm$1.25% for HPGe. Relative sensitivity, or number of counts within the images, was measured relative to the mean counts recorded for the CZT images with a $\pm$10% energy window. We calculated scatter and torso fractions, defined as the fraction of all events within the chosen energy window that scattered in the phantom and the fraction of all

events within the chosen energy window that originated in the torso, respectively. Line profiles were drawn through the horizontal center of the images to assess tumor signal and background levels in CZT and HPGe. Average tumor contrast and signal-to-noise ratios (SNR) for each individual tumor were calculated using a 3×3 pixel ROI centered on the tumors, and a 9×9 pixel ROI of adjacent background and applying (3) and (4).

Statistical analysis using the student-t test with an 95% confidence threshold was performed to compare contrast and SNR between the detector and energy window combinations for each tumor. Additionally, we investigated the quality of HPGe and CZT images with equivalent counts. Images were generated with equal count densities of approximately 1000 counts/cm^2 and energy windows of $\pm$10% and $\pm$2.5% for CZT and HPGe, respectively. These energy windows were chosen for each detector as they offered the highest relative sensitivity for each system. The same image and statistical analysis was performed for images with equivalent count densities.

4.4 Experimental and Simulation Results

4.4.1 Experimental Validation

Normalized energy spectra from the MI4 HPGe detector and modeled HPGe breast camera model are displayed in figure 29. The measured FWHM of the 140-keV photopeak was 1.43 keV, resulting in an ER of 1.02%.We modeled our HPGe detector with a fixed ER of 1.0% at 140 keV, given that the ER of these detectors

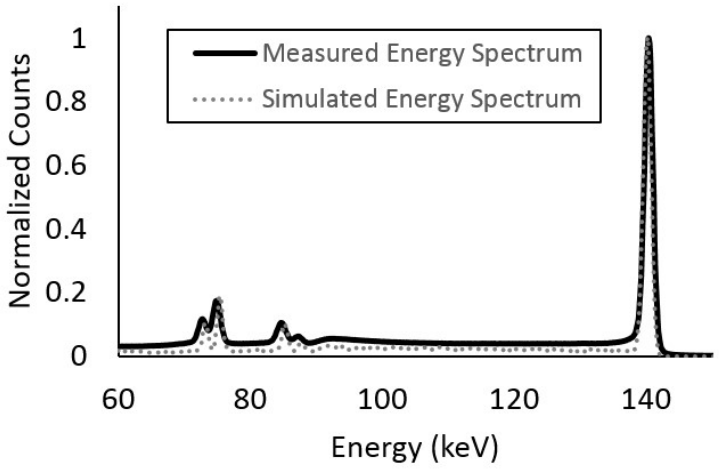

Figure 29: Energy spectra acquired using a ^{99m}Tc source with the MI4 HPGe camera and the Monte Carlo simulation model. The spectra have been normalized for comparison. The two energy spectra correlate well, particularly for the 140-keV photopeak. The small differences in intensity is due to differing amount of lead shielding around the MI4 and modeled breast camera. The equal FWHMs for the peaks signifies that the energy resolution model for varying energies is accurate.

are consistently around 1.0% at 140 keV (Johnson et al 2011b).

The planar sensitivities for the experiment and simulation were 5405 and 10864 cpm/MBq (counts per minute per mega-becquerel), respectively. The current method for processing events excludes those in which charge is collected on more than one strip on either side. The strip readout of the MI4 was not explicitly modeled, but count losses from its effects can be estimated. More than 10% of photons would be expected to interact in or adjacent to gap regions between strips and, therefore, not be included, as these events would result in incomplete charge collection or charge sharing between strips. In addition, approximately 35% of incident photons undergo Compton scattering within the detector, leading to energy deposition across multiple

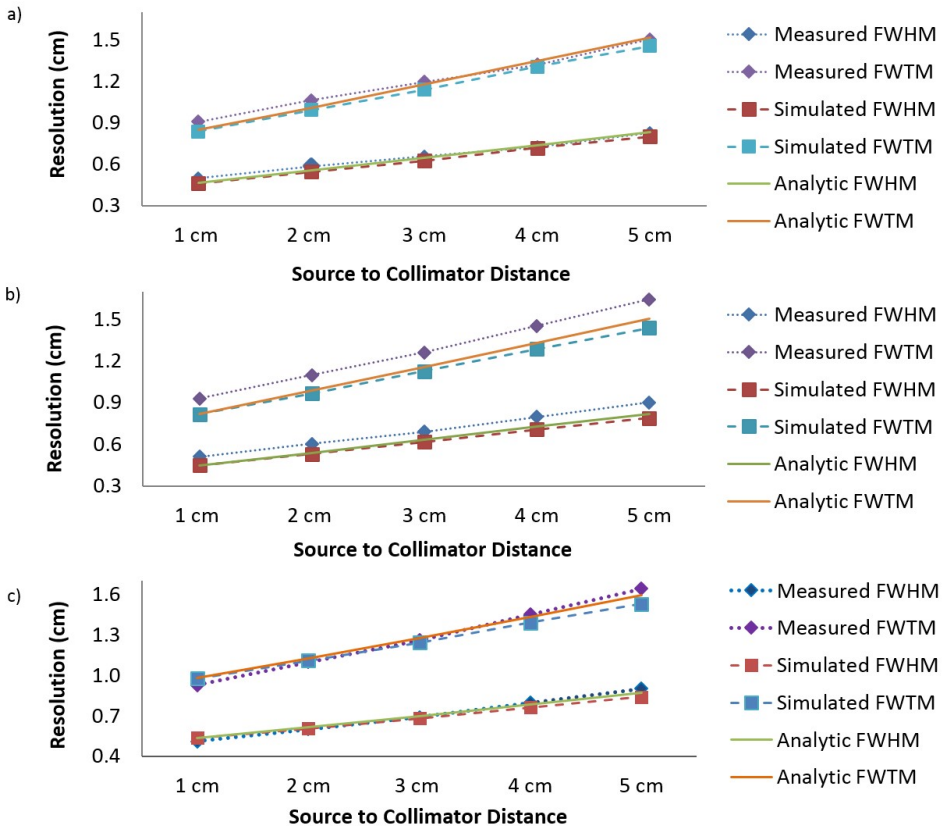

Figure 30: The total system resolution measurements along the (a) x-axis and (b) y-axis. FWHM and FWTM are shown for the experiment, simulation, and analytic calculations. Percent error between the experimental and simulated resolution were 4.4% and 11.5% for the x- and y-axis, respectively. The intrinsic resolution in the y-dimension was altered in the model for more realistic system resolution, shown in (c). The percent error after adjustment was 1.2% in the y-axis, signifying comparable performance between the MI4 HPGe detector and the Monte Carlo model.

strips and exclusion from event totals. Accounting for these count losses in the simulation yields a planar sensitivity of 6189 cpm/MBq, for a 14.5% difference in sensitivity between the model and the MI4 camera. Other factors, such as detector dead-time and edge effects, were not modeled and could also reduce the measured MI4 camera sensitivity.

Figure 30 shows the results for the experimental, simulated, and analytic FWHM and FWTM measurements in the x- and y- dimensions. There is agreement in FWHM and FWTM along the x-axis, where the average percent error was 4.4%. However, an error of 11.5% between the experimental and simulation resolutions in the y-axis was observed, as seen in figure 30(b). After compensating for the difference between simulation and experiment, the intrinsic resolution in the y-dimension was 0.33 cm. Figure 30(c) displays the new total system resolution trends by distance for the y-dimension. In this case, the agreement between measured and simulated resolution improved to 1.2% percent error.

4.4.2 Generated Energy Spectral Analysis

CZT spectra published by Hruska and O'Connor (2008a) and from our CZT model are displayed in figure 31. Benchmarking our simulations to those in Hruska and O'Connor (2008a) was critical to validating our simulation methods employed for the HPGe camera model. The total spectra from each model exhibit similar spectral features and trends. The major differences between the two sets of spectra are the first-order scatter spectrum and the liver spectrum, but these differences can be attributed to the truncated size and emission probability of the liver. Successfully replicating the CZT model developed by Hruska and O'Connor (2008a) provides additional support to the accuracy of our HPGe breast camera model.

Generated energy spectra from one run of the CZT and HPGe simulations are

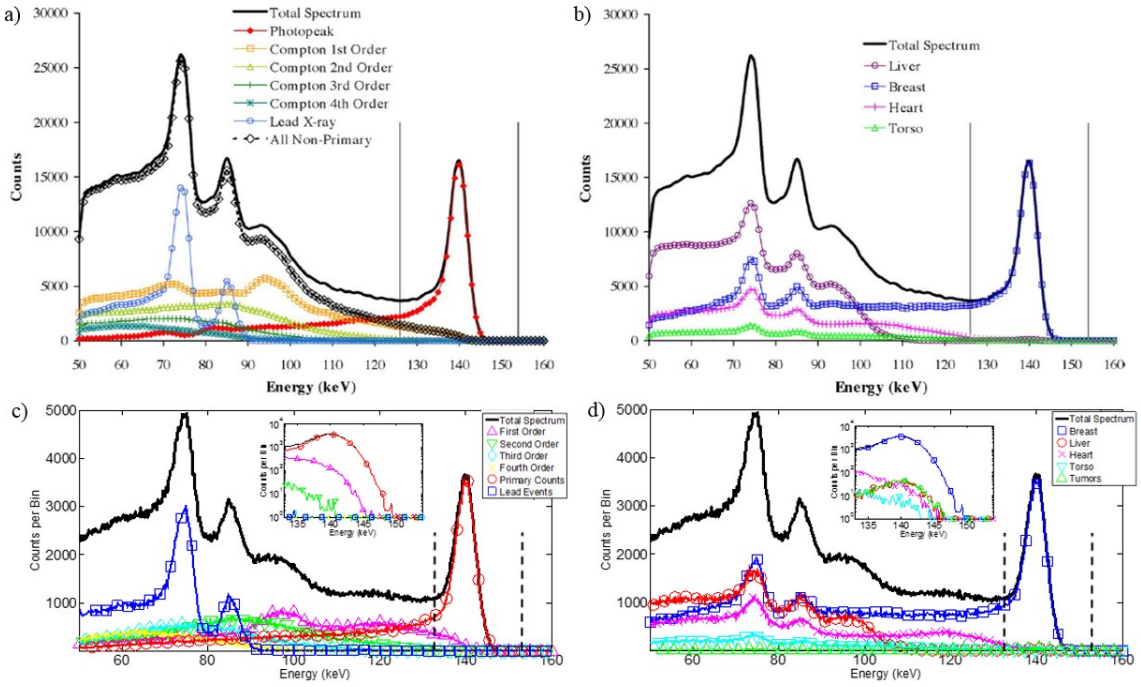

Figure 31: The CZT energy spectra, parsed by scatter order and photon origin, from (a,b) Hruska and O'Connor (2008a) and from (c,d) our developed CZT model. Vertical lines correspond to energy windows. Log-The total energy spectra have comparable features and trends. Differences between spectra are due to the truncated liver in our simulations, which reduces the first-order scatter and liver events. Benchmarking our model against the published model strengthens the validity of the HPGe breast camera model.

displayed in figure 32. Scatter and torso fractions within set energy windows of energy spectra are shown in table 11. Some of the advantages of HPGe can be observed in these energy spectra, including the lack of low-energy tailing and narrower photopeaks. Less scatter and photons originating from the torso fall within the energy windows in HPGe spectra than a CZT spectra. Thus, background from the torso and scatters within the breast or collimator contribute less to generated images.

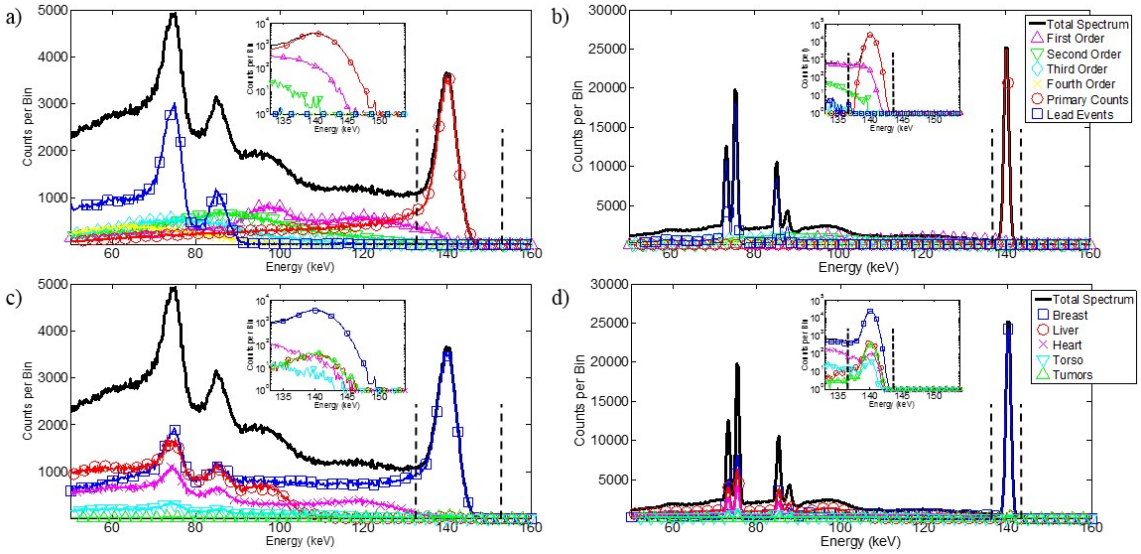

Figure 32: Generated energy spectra from the breast imaging simulations. (a) CZT spectrum parsed by scatter order. (b) HPGe spectrum parsed by scatter order. (c) CZT spectrum parsed by event origin order. (d) HPGe spectrum parsed by event origin. Legends describe plots along same horizontal axis. The vertical dashed-lines signify energy windows of -5%/+10% on CZT and ±2.5% on HPGe placed around the 140-keV photopeak. Log-scale insets of the photopeak are displayed in each plot. The low-energy tailing of CZT removes primary events from the energy window and the image. The 1% ER at 140 keV of HPGe provides sharp peaks that enable the use of narrower energy windows to minimize inclusion of out-of-field radioactivity that undergoes small-angle scattering.

Table 11: Performance measures by detector type and energy window.

Detector System	Energy Resolution	Energy Window	Relative Sensitivity	Scatter Fraction	Torso Fraction
CZT	3.8%	±10%	100.00%	17.22%	7.32%
		-5%/+10%	76.61%	8.63%	3.35%
HPGe	1.0%	±2.5%	123.70%	4.66%	2.83%
		±1.25%	120.45%	2.41%	2.50%

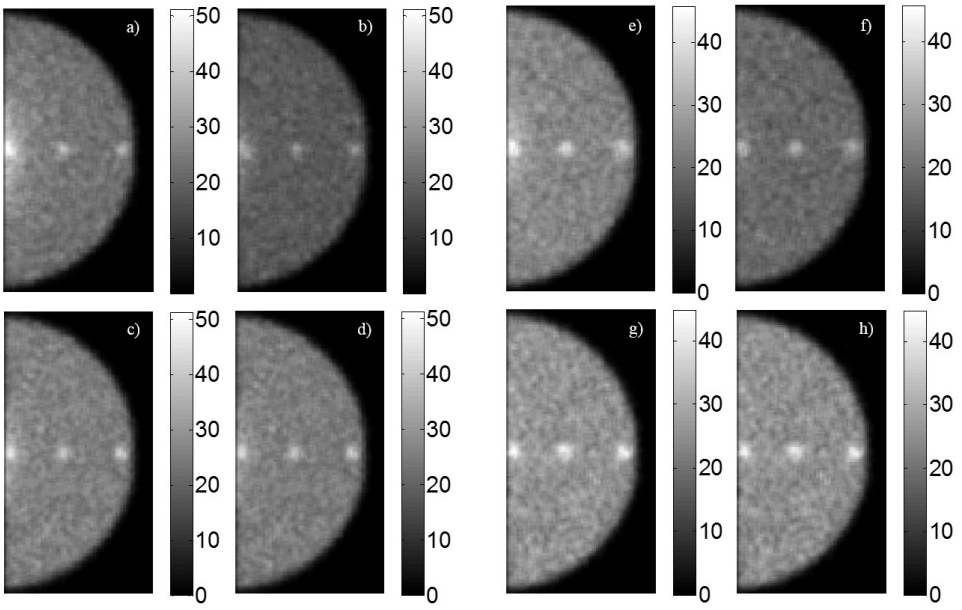

Figure 33: Filtered breast images generated from one simulation run. Figures (a) - (h) correspond to tumors located at a 1-cm depth and (e) - (h) correspond to the tumors at a 4-cm depth. (a), (e) CZT ±10%. (b), (f) CZT -5%/+10%. (c), (g) HPGe ±2.5%. (d), (h) HPGe ±1.25%.

4.4.3 Simulated Images

Representative images from a single simulation run following the application of a 3×3 mean filter are shown in figure 33. The three tumors at both depths within the breast phantom are visible across all the detector/energy window pairings. Line profiles drawn across the center of the CZT and HPGe images in figure 33 are shown in figure 34, confirming that the signal from the tumors rises above the background in CZT- and HPGe-generated images.

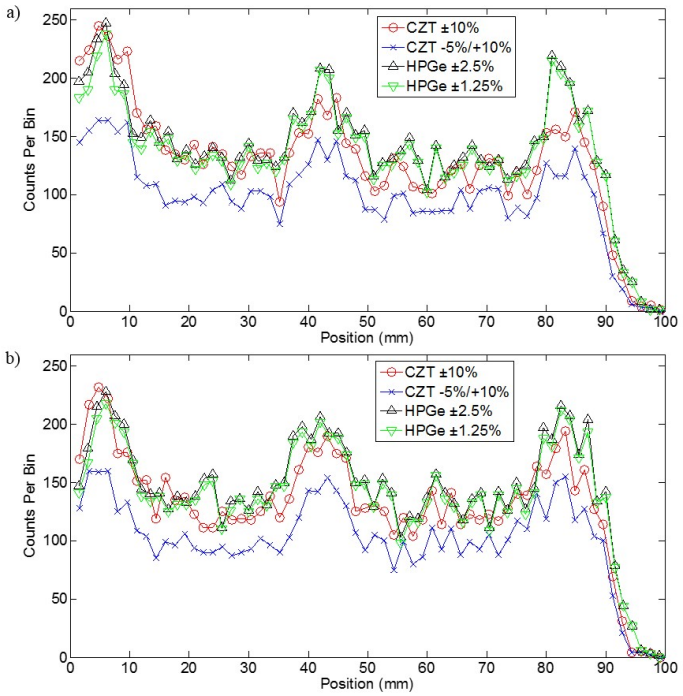

Figure 34: Line profiles drawn through the center of the CZT and HPGe images in figure 33. The zeroth position corresponds to the region nearest the chest wall. (a) Profiles for the 1-cm depth tumors. (b) Profiles for the 4-cm depth tumors. The high intensity peaks are consistent with the position of the three tumors. In general, the HPGe profiles are higher in intensity for the tumors and background regions.

4.4.4 Image Performance

Table 11 also displays the relative sensitivity results from the simulations. Average tumor contrast and SNR for each tumor are compared in figure 35 for each detector and energy window combination at both tumor depths. When comparing image quality between CZT and HPGe for tumors at a 1-cm depth, we observe no statistical difference for both tumor contrast and SNR. For the 4-cm depth tumors, tumor 2 contrast is statistically higher for CZT with the asymmetric energy window than both HPGe-acquired images ($p = 0.02$). Conversely, the SNR of tumor 3 for both HPGe images is significantly greater than CZT-acquired images ($p < 0.005$).

4.4.5 Equal Sensitivity Imaging Performance

With a gain of $\sim$25% for HPGe images, the count-density of those images were reduced by 20% to equal those of the CZT images. Figure 36 shows images for CZT and HPGe with equal count densities and energy windows of $\pm$10% and $\pm$2.5%, respectively. All three tumors at both depths are visible in these images. Figure 37 displays the average contrast and SNR measurements for these detector and energy window pairings. Reducing the number of counts in HPGe images to match that of CZT images yields no statistical differences in contrast or SNR for 1-cm depth tumors. Only tumor 2 at a depth of 4 cm saw a statistically significant difference in SNR between CZT and HPGe ($p = 0.02$).

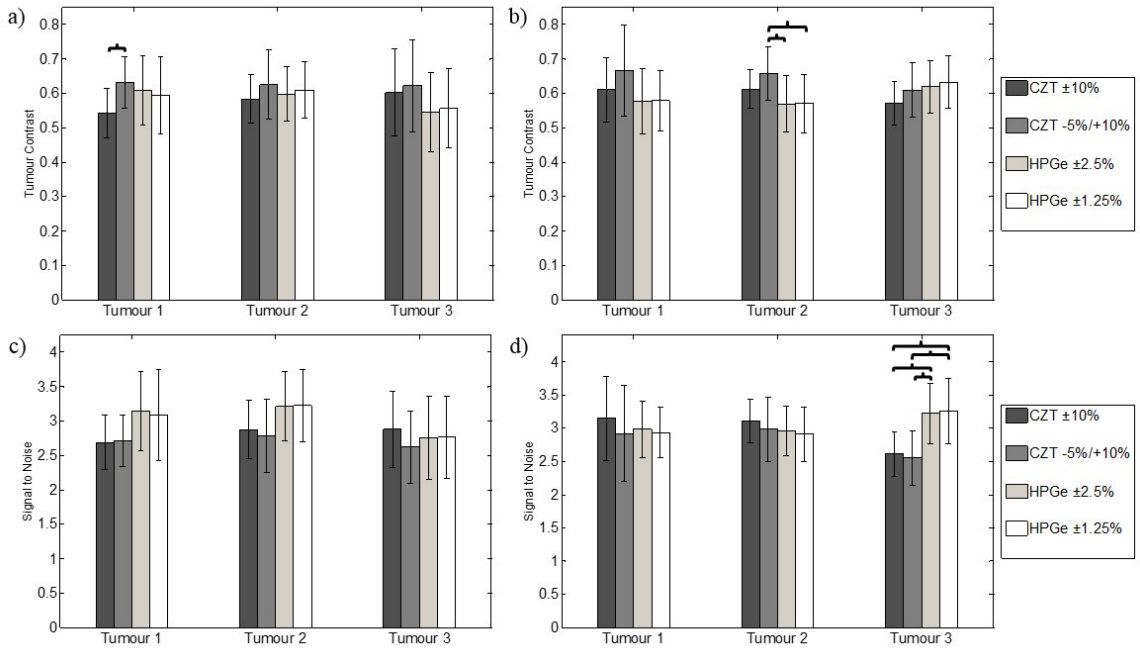

Figure 35: Average tumor contrast and signal-to-noise measurements for all combinations of detector and energy window across ten independent simulations for the (a), (c) 1-cm depth tumors and the (b), (d) 4-cm depth tumors. Error bars represent one standard deviation from the mean. The brackets point to the detector/energy window combinations with significant differences, or p-values < 0.05. With the 1-cm depth tumors, CZT and HPGe exhibit similar performance, while SNR is greater for HPGe-acquired images for tumor 3 at a depth of 4 cm.

4.5 Discussion

This study aimed to simulate a realistic HPGe camera for planar nuclear breast imaging based on the current intrinsic properties of the MI4 HPGe detector. As a basis for comparison, we benchmarked our simulations against an augmented CZT model based on the LumaGEM 3200S as cited in Hruska and O'Connor (2008a). We were interested in comparing the differences in scatter contributions, image quality and sensitivity when the image geometry was kept constant, but the detector crystal

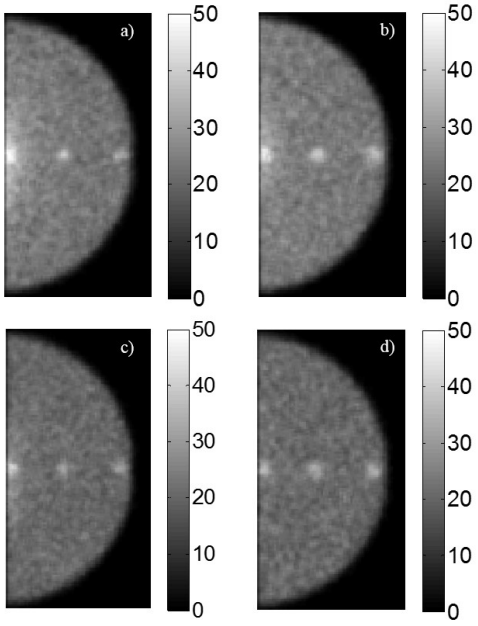

Figure 36: CZT- and HPGe-acquired projections with equal count densities. (a) CZT ±10% with 1-cm depth tumors. (b) CZT ±10% with 4-cm depth tumors. (c) HPGe ±2.5% with 1-cm depth tumors. (d) HPGe ±2.5% with 4-cm depth tumors.

was switched from CZT to HPGe. To evaluate realistic imaging systems, the majority of intrinsic properties for the HPGe and CZT models were consistent with the MI4 (HPGe) and LumaGEM (CZT) systems, including energy resolution, detector thickness, effective pixel sizes, and ISR. We sought to investigate whether the superb energy resolution of HPGe would translate into improved breast imaging performance.

Physical measurements of the intrinsic spatial and energy resolutions made on the MI4 HPGe detector were used as inputs for the HPGe breast camera model. The HPGe camera model was validated using total system resolution measurements across several distances in accordance with NEMA standards. Energy resolution measurements were comparable to previous HPGe detectors, however, ISR in the

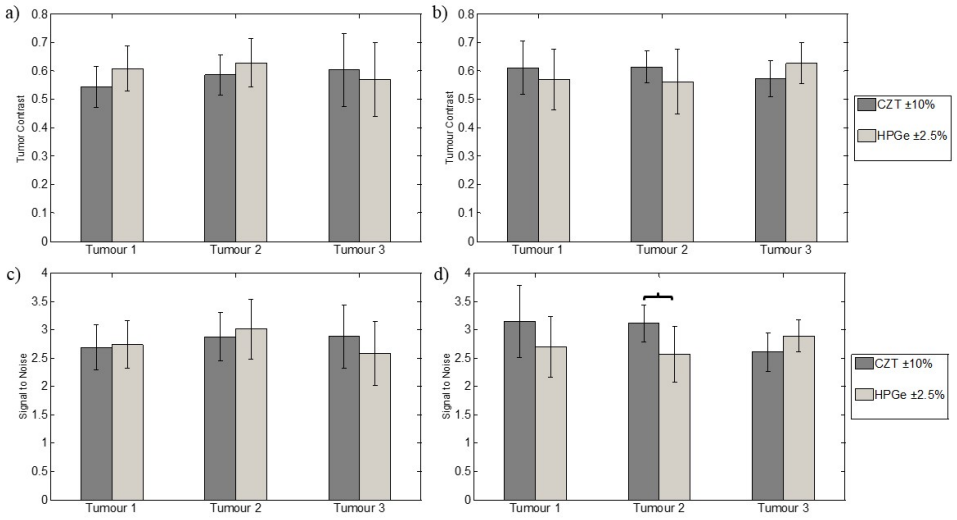

Figure 37: Average contrast and signal-to-noise measurements for the equal count images in figure 36. (a), (c) correspond to the 1-cm depth tumors and (b), (d) correspond to the 4-cm depth tumors. Error bars represent one standard deviation from the mean. The brackets point to the detector/energy window combinations with significant differences, or p-values < 0.05. Equivalent performance between equal count CZT and HPGe images is observed for the 1-cm depth tumors. However, a significance difference ($p = 0.01$) in SNR for tumor 2 at a depth of 4 cm is also observed.

x and y dimensions differed considerably. One explanation for the difference in X and Y ISR is the difference in the electronic noise between the p- and n-sides of the particular detector used in the measurements. In addition to varying ISR, the total system resolution in the y-dimension was initially underestimated. We believe that the underestimation in y-axis spatial resolution is due to some additional blurring that is not accounted for by summing ISR and collimator resolution in quadrature. One explanation for this may be the alignment of the hexagonal-hole collimator to the HPGe detector. The angle between the square pixels of the MI4 and the collimators hexagonal-holes may result in preferential blurring in one dimension.

One major limitation of this study is that a proper experimental validation of the CZT model could not be performed because we do not possess a CZT camera. Also, we do not possess the collimator from the base CZT system, so the HPGe model validation was completed using an available LEHR collimator. The sensitivity of this collimator is 23% lower than the one used in Hruska and O'Connor (2008a). To achieve the same clinical count density as images in Hruska and O'Connor (2008a), the total number of simulated photons is increased by a factor of 1.29, akin to extending the imaging time from 10 minutes to 12.9 minutes. Additionally, without a CZT detector, an empiric tailing model was generated using an experimental CZT spectrum published in Hruska and O'Connor (2008a). The method used for determining the distribution of tailed events was done following Hruska and O'Connor (2008a) as well. Applying their tailing method resulted in similar quality energy spectra, particularly

around the 140-keV photopeak and for the primary count spectral line.

Another change from the previous study was our calculation of contrast and SNR. Differences in measured tumor contrast arise from our use of the average tumor signal in a 3×3 ROI instead of the maximum tumor signal. The average tumor signal over an ROI was used to calculate tumor contrast to reduce the influence of Poisson noise on the tumor contrast. In addition, the tumor contrast and SNR results presented here represent the average over ten independent simulations conducted for each type of detector. Even with these slight differences, our maximum tumor contrast averaged over the ten simulations is within one standard deviation of the maximum tumor contrast reported in Hruska and O'Connor (2008a) (data not shown). Some agreement between this study and Hruska and O'Connor (2008a) is observed in the relative sensitivities when applying $\pm$10% and -5%10% energy windows, but slight differences are seen in scatter and torso fractions. This could be due to the slight changes in the imaging geometry, including the truncated torso and liver regions.

Due to the good charge transport properties of HPGe, there is no low-energy tailing of primary events exhibited in its energy spectra. The ER of HPGe also provides sharper photopeaks than that of CZT. This enables the use of narrower energy windows, which helps minimize the contribution from scatter events originating from the breast and the torso. In both CZT and HPGe, we see some first-order scatter events fall within the energy windows and contribute to the images. The vast majority of higher-order scatter events lose enough energy to fall outside the energy windows for

both detectors, but some second-order scatter contribute to the generated images. We also observe that out-of-field contributions from the heart, liver, and torso fall within the energy windows utilized for both CZT and HPGe. Many of these events are due to gamma-ray penetration through the lead shielding of the detector, but quantitative results show that both the scatter and torso fractions are lower for HPGe than CZT.

CZT-generated images with a ±10% energy window contain regions of high torso background levels along the chest wall. This region extends around the tumor closest to the torso, decreasing its visibility and lowering contrast. Applying a -5%/10% energy window to the CZT spectrum suppresses this torso background and provides a statistically significant gain in contrast ($p = 0.01$) for the 1-cm depth tumor 1 closest to the torso. In addition, applying the asymmetric energy window provides a statistically significant gain in tumor 2 contrast for deep-seated tumors compared to HPGe. The torso background was also observed in HPGe images, but with a lower intensity than the CZT image with the ±10% energy window. The HPGe images with both energy windows yield statistically similar tumor contrast and SNR values to CZT images when tumors are in closer proximity to the camera. However, the image quality of deep-seated tumors yields contradictory results with HPGe-acquired images showing enhanced SNR for tumor 3 over CZT images. One reason for this can be contributed to the superb ER of HPGe that allows for a lower scatter content farthest from the chest wall. This lower scatter content, as compared to the high scatter and torso contribution near the chest wall, corresponds to lower image noise,

which would enhance SNR. This finding agrees with some literature related to the scatter distribution of nuclear breast images and the importance of energy resolution (Pani et al., 1998; Williams et al., 2000, 2002). However, with the enhancement only observed with deep-seated tumors, a case for ER offering little to no benefit to breast imaging can also be made (Hruska and O'Connor, 2006a, 2008a).

One reason NBI techniques are currently not proposed for breast screening is the radiation dose to the body, which can be 5-10 times greater than standard digital mammography (Hendrick, 2010). In an effort to lower the dose to the patient, methods are being developed to increase sensitivity while maintaining resolution and tumor contrast so as to reduce injected radioactivity without the loss of image quality (O'Connor et al., 2010). For this reason, the metrics for performance used in this and other similar studies have been relative sensitivity, tumor contrast, and SNR (Garibaldi et al., 2006; Judy et al., 2010; Hruska and O'Connor, 2006a, 2008a). Clinical dedicated breast imaging protocols measuring ^{99m}Tc-sestamibi distributions with pixilated CZT modules use a $\pm 10\%$ energy window, making it the basis for our comparisons to HPGe with various energy windows (Hruska and O'Connor, 2006a, 2008a). When lowering the count density of HPGe images by 20% to match that of CZT, equivalent image quality was observed for the majority of cases. Only tumor 2 at a depth of 4 cm exhibits a statistical difference ($p = 0.01$) between CZT and HPGe. This implies that a count reduction of 20% for HPGe when imaging centralized tumors far from the camera may be too great to maintain equivalent image quality

to CZT. In the future, a more thorough simulation study investigating the minimal injected activity for clinical breast imaging with HPGe cameras will be performed.

One result of these simulations was that the HPGe system did not demonstrate significant gains in lesion SNR, even with an approximate 50% increase in sensitivity compared to the CZT system with the -5%/+10% energy window. One reason for this outcome may be due to counting statistics and the number of independent simulations conducted. From Poisson statistics, lesion SNR would be expected to increase as the square root of the count sensitivity. Hence, on average, 20% and 50% increases in sensitivity correspond to expected $\sim$10% and 22% increases in SNR, respectively. However, there exists large variations in a single measurement of tumor contrast and SNR. For a single detector and energy window combination, we observed SNR values ranging between 2 and 4. This leads to large error bars on the average tumor contrast and SNR measurements, which diminishes the statistical significance of differences between the image quality metrics for CZT and HPGe. For this reason, there were very few significant gains observed in lesion SNR, even with the higher count sensitivities in HPGe. It is possible that more simulation trials could shrink the error bars on the average contrast and SNR measurements, but these results still offer some insight into the relative performance of HPGe and CZT cameras.

Overall, the HPGe system offers comparable tumor contrast and SNR to the CZT system, but with increased relative sensitivity and less contribution from scattered photons and torso background. It should be noted that the relative sensitivity gains

observed in HPGe over CZT primarily reflect the event-by-event tailing model. Although the tailing model used here was based on published data, energy loss due to tailing varies with the CZT module properties, thus the relative sensitivity gains quoted here are not absolute. However, we believe that the superb charge-carrier transport properties of HPGe does provide relative sensitivity gains, whereas any tailing present in CZT reduces its sensitivity by removing primary events from the applied energy window. With these sensitivity gains, a reduction in the injected dose of radioactivity could be possible with HPGe cameras without sacrificing image quality. This is reflected in the statistically similar image quality between CZT and HPGe images after lowering HPGe count density, akin to reducing the effective radiation dose to the subject and acquiring for the same amount of time. The superior ER of 1% at 140 keV in HPGe enables us to utilize tighter energy windows around a higher quality photopeak, which better delineates primary events from scatter events and provides better suppression of background from the torso. Thus, HPGe detectors and parallel-hole collimators may offer some benefit for whole breast imaging, even without significant gains in image quality.

4.6 Chapter Summary

In this chapter, we conducted simulations to investigate the potential performance of a breast-specific imaging system using 5-mm thick CZT in comparison to the same system with 10-mm-thick HPGe. For equivalent activity imaged, HPGe provides bet-

ter relative sensitivity and similar tumor contrast and SNR while better suppressing small-angle scatter events and background from the torso. HPGe may offer further advantages when employing alternative collimation schemes that open the FOV to look deeper into the chest wall, where small-angle scattering of photons from the torso may be more problematic. In the next chapter, we will conduct simulations of such alternative collimation schemes to assess their value in NBI. We also plan to explore alternative acquisition techniques that utilize the DOI estimation for limited-angle tomographic imaging.

CHAPTER V

PARALLEL-HOLE COLLIMATOR DESIGN AND SELECTION FOR GERMANIUM DETECTORS

5.1 Introduction

We have previously discussed methods for improving the image quality of nuclear breast imaging. The first step in this pursuit was adopting HPGe detectors with ideal properties for single photon imaging. A HPGe breast camera model was developed and found to have comparable performance to a clinical CZT-based imaging system with an enhancement in count sensitivity.

Another way to further improve the performance of NBI with HPGe detectors is to employ optimal collimation. Because gamma- and x-rays cannot be focused with lenses like optical photons, absorptive collimation is required to form meaningful images. The collimator is one of the determining factors in the performance of a gamma camera, as any form of absorptive collimation eliminates upwards of 99.9% of all emissions approaching the detector. Thus, the design of the collimator is crucial to optimizing imaging system performance. An important part of collimator design is considering the trade-off between spatial resolution and count sensitivity. Collimators with long, thick septa will produce higher-resolution images, but high levels of quantum noise may force long acquisition times or increased injected radiopharmaceutical doses. Conversely, short, thin septa will allow more incident photons for low quantum

noise, but images would exhibit low spatial resolution and even image artifacts due to photon penetration (Cherry et al., 2012; Hendee and Ritenour, 2003).

Original scintimammography protocols used a conventional low energy, high resolution (LEHR) collimator (Khalkhali et al., 1999). However, phantom studies by Buvat et al. (2001) suggested that the sensitivity for <15-mm tumors is improved with ultrahigh resolution fan beam collimation, taking advantage of its magnification factor. With the development of dedicated breast gamma cameras, different collimation schemes were explored with closer camera geometries, including pinhole apertures, standard LEHR parallel hole collimators (Smith et al., 2003) and novel light-weight, wire-mesh collimators (Saripan et al., 2009; Saad et al., 2011). Phantom studies investigating the effects of collimator selection for dedicated breast cameras found that high-sensitivity parallel-hole collimation provided higher SNR for sub-centimeter tumors (Gruber et al., 1999; Hruska and O'Connor, 2006b). In addition to highly-sensitive collimation, cameras utilizing short bores matched to detector elements increase the count efficiency of imaging systems (Tornai et al., 1997; Raghunathan et al., 2005). Most recently, work in optimizing the collimator for MBI revealed that tungsten parallel-hole collimation registered to the pixels of a CZT system offers increased sensitivity over conventional hexagonal-hole lead collimators (Weinmann et al., 2009). Optimizing the count sensitivity and spatial resolution tradeoff with the collimator may allow for a reduction in injected radioactivity and decreasing absorbed dose to the patient without sacrificing image quality.

In this chapter, we will investigate the impact of collimator choice with HPGe detectors on breast imaging performance. We will also investigate the imaging differences between select lead and tungsten collimators. The design of potential collimators, influenced by the literature and architecture of the HPGe DSSDs, is described. Monte Carlo simulations of NBI scans with various parallel-hole collimation schemes are conducted to determine the best choice for HPGe detectors.

5.2 Materials and Methods

5.2.1 Collimator Designs

The general geometry of the collimator and detector is displayed in figure 38. A typical parallel-hole collimator used in clinical breast imaging is constructed from lead with hexagonal-shaped holes and dimensions of 1.85 mm diameter, 20 mm length, and 0.3 mm septa thickness. The parallel-hole collimators explored in this study were designed based on results from Weinmann et al. (2009), which used a tungsten collimator registered, or matched, to CZT pixels. The advantage of registered collimator is twofold. First, tungsten is a more dense, higher Z number than lead, providing a larger attenuation coefficient of 32.48 cm^{-1} compared to 26.32 cm^{-1} at 140 keV. The higher attenuation coefficient lowers the probability of gamma-ray penetration through the collimator and suppresses image artifacts. Second, the matched collimation to detector pixels maximizes the exposed active area of the detector, which provides the best sensitivity-resolution tradeoff for the gamma camera. These points

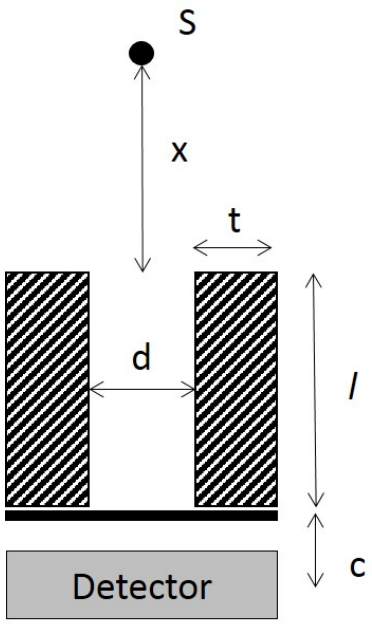

Figure 38: A schematic diagram of the detector and parallel-hole collimator with labeled parameters. The point S represents a radioactive source, the slant pattern blocks represents two septa of the collimator, and the dark block represents the aluminum entrance window to the detector. Variables symbolizing particular distances (c, d, l, t, and x) are represented here and are used with analytic calculations to predict collimator performance.

are strongly considered in designing optimal collimators for HPGe breast cameras.

In designing registered collimators for an HPGe imaging system with orthogonal strips, we consider two opposing criteria: 1. collimation with minimized penetration to suppress image artifacts or 2. matched spatial resolution to the standard collimator. The procedure for collimation design is summarized in figure 39.

1. Because photon interactions in the gap regions exhibit incomplete charge collection (Hayward and Wehe, 2008a), we register the septa of the collimator to the gaps.The width of the gap between detector strips dictates the collimator septal thickness.

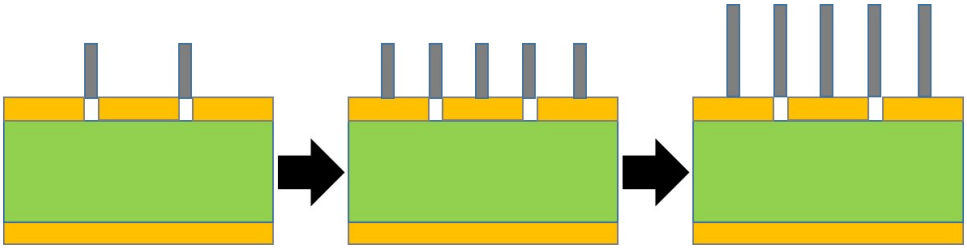

Figure 39: A visual representation of the collimator design process for HPGe cameras. Septa are first placed over the gaps between detector strips. Additional septa are added to divide orthogonal strips into 2×2 or 3×3 regions, followed by adjusting the length of the collimator to minimize photon penetration or match standard collimation spatial resolution.

Knowing that the strip pitch and gap widths of real HPGe detectors, we placed collimator septa over the gaps in 5 mm intervals with a thickness of 0.25 mm to minimize gamma-ray interactions in gap regions.

2. The previous method of septal placement results in large collimator holes of 4.75 mm in width. To remedy this, we divide the exposed strip areas into 2×2 and 3×3 regions separated by 0.25 mm thick septa for reasonable collimator-hole dimensions. This step limits the hole-sizes for our designed collimators.

3. Finally the collimator length is determined based on which criterion is applied.

1) The University of Chicago penetration criterion describes whether an image acquired with a parallel-hole collimator is free of artifacts (Gunter, 2004). The criterion has the following mathematical form:

$$P \leq \mu l(1 - \frac{A_{hole}}{A_{unit}}); \tag{14}$$

where P is a penetration parameter based on the hole shape, μ is the attenuation

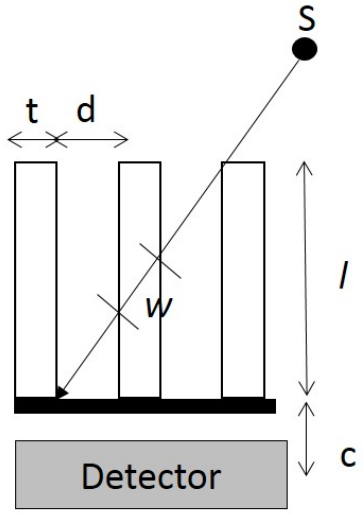

Figure 40: A schematic diagram showing the minimal path length, w, for photon penetration through a collimator septum.

coefficient of the collimator material, and A is the area. For square holes, P is equal to 12.57. Rearranging (14), substituting the terms for the hole and unit areas, and solving for the length, l, yields the minimal collimator length that satisfies the Chicago criterion:

$$l \geq \frac{P/\mu}{1 - \left(\frac{d}{d+t}\right)^2}. \tag{15}$$

As an aside related to collimator penetration, the minimal length for photon penetration through a septum can be calculated analytically. Following from figure 40, the minimal length can be written, assuming that $l \gg 2d + t$, as (16):

$$w = \frac{tl}{2d + t}. \tag{16}$$

The fraction of gamma-rays expected to penetrate the collimator, β, given w can be

calculated by applying (17):

$$\beta = e^{-\mu w}. \tag{17}$$

2) For a specified spatial resolution, the analytic function for parallel-hole collimator resolution is used (see (8)). The length, l_e, is the effective length adjusted for collimator attenuation:

$$l_e = l - 2\mu^{-1}. \tag{18}$$

Combining equations (8) and (18), we have the second criterion to determine collimation length:

$$l = \frac{d(x+c)}{R_g - d} + 2\mu^{-1}. \tag{19}$$

We fix the collimator length for our simulations by rounding up to the nearest tenth of a millimeter from the results of (15) and (19).

The following analytic equations are used to calculate spatial resolution and geometric efficiency of the hexagonal and square collimators to compare their potential performance (Anger, 1967; Weinmann et al., 2009; Smith et al., 2003; Wieczorek and Goedicke, 2006). The efficiencies for hexagonal-hole and square-hole collimation are given by:

$$g_{hex} = \frac{\sqrt{3}}{8\pi l_e^2} \frac{d^4}{(d+t)^2} \tag{20}$$

$$g_{sq} = \frac{1}{4\pi l_e^2} \frac{d^4}{(d+t)^2}. \tag{21}$$

For both hexagonal-hole and square hole collimators, we estimate the total resolution

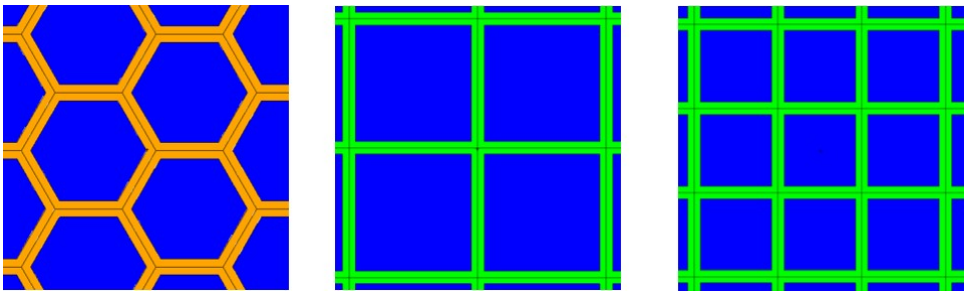

Figure 41: Axial views of the standard lead hexagonal-hole collimator (left) and two tungsten square-hole collimators (center and right). The square-hole collimators are specifically-designed to match collimator holes to the orthogonal strips of the HPGe detector.

Table 12: Collimator Dimensions and Theoretical Properties.

Collimator Scheme	Collimator Material	Hole Length (l)	Hole Width (d)	Septa Thickness (t)	Relative Sensitivity	Collimator Resolution	Penetration Fraction
Hexagonal	Lead	20.0 mm	1.85 mm	0.30 mm	100%	4.47 mm	1.93%
Hexagonal	Tungsten	20.0 mm	1.85 mm	0.30 mm	98.2%	4.45 mm	0.77%
Square 2×2 Pene	Lead	20.0 mm	2.25 mm	0.25 mm	186%	5.34 mm	6.26%
Square 2×2 Pene	Tungsten	20.0 mm	2.25 mm	0.25 mm	183%	5.31 mm	3.27%
Square 2×2 Res	Tungsten	29.7 mm	2.25 mm	0.25 mm	81.5%	4.41 mm	0.62%
Square 3×3 Pene	Tungsten	14.0 mm	1.42 mm	0.25 mm	137%	4.29 mm	2.52%
Square 3×3 Res	Tungsten	12.7 mm	1.42 mm	0.25 mm	167%	4.55 mm	3.55%

at the center of the HPGe detector with an intrinsic spatial resolution of 1.5 mm and using (9), where $c = 14.6$ mm and $x = 10$ mm. In addition, we calculated the expected penetration percent through the collimator using (17).

Recall that we strive to explore the imaging benefits of substituting lead collimation for tungsten. To this end, we select the conventional hexagonal-hole collimator and the most efficient collimator from analytic formulations to investigate the lead and tungsten differences in performance. Top views of the standard and designed collimators are shown in figure 41. Table 12 lists the collimator parameters and analytic properties. These collimators were evaluated in simulations, which are described in section 5.2.2.

5.2.2 Simulation Details

The HPGe detector model utilized in chapter IV was adopted for this collimation study. The model maintained an energy resolution of 1% at 140 keV with an isotropic intrinsic spatial resolution of 1.5 mm. The water breast/torso phantom described in chapter IV is again utilized for Monte Carlo radiation transport simulations. This time, the three 1-cm diameter spherical tumors are kept at a depth of 1 cm with a TBR of 5:1. All other simulation parameters are maintained. NBI scans were simulated for each collimator with 3×10^{10} 140-keV photons emitted from the breast-torso phantom, equivalent to imaging ~44.5 MBq of ^{99m}Tc-MIBI for 10 minutes. Simulated energy spectra from NBI scans were generated and partitioned by scatter order and origin. All images were created with ±2.5% and ±1.25% energy windows around the 140-keV photopeak. Scatter and torso fractions along with tumor contrast and SNR were calculated for each individual tumor from generated energy spectra and images, as well as relative sensitivities for the imaging system with each collimator. Average tumor contrast and SNR for each individual tumor were calculated using a 3×3 tumor ROI and a 9×9 ROI of adjacent background regions by applying (3) and (4). Error propagation using Poisson statistics is applied to the tumor and background measurements as an indication of the spread in contrast and SNR measurement.

In addition to the breast/torso phantom, a contrast-detail phantom was modeled to determine the image quality and detectability of various tumor sizes and activity concentrations. A diagram of the phantom is presented in figure 42. The phantom

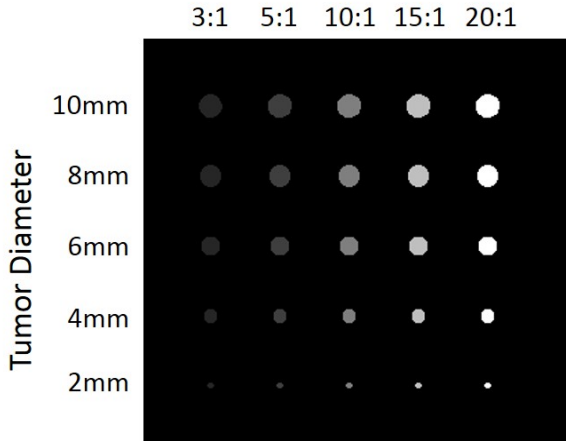

Figure 42: An axial view of the contrast-detail phantom developed for investigating tumor detectability at a 1-cm depth. Tumor diameters are labeled along the right. Lighter color circles denote higher radioactivity concentrations, labeled on top. Tumor diameter and activity concentrations are varied for contrast measurements and line profiles.

consists of a 5×5 grid of tumors at 1-cm depth evenly spaced through the FOV. Tumor diameters vary from 2-mm to 10-mm and TBRs vary from 3:1 up to 20:1. 8.25×10^7 140-keV photons, or ∼3.60 MBq ^{99m}Tc-sestamibi imaged for 10 minutes, were simulated with emissions collimated into a cone with 22.5° half angle towards the camera to minimize computation time. Only a ±2.5% energy window around 140 keV was utilized for image generation, and tumor contrast and SNR were calculated as previously described. Line profiles through select tumors were also generated to assess signal intensities and background noise.

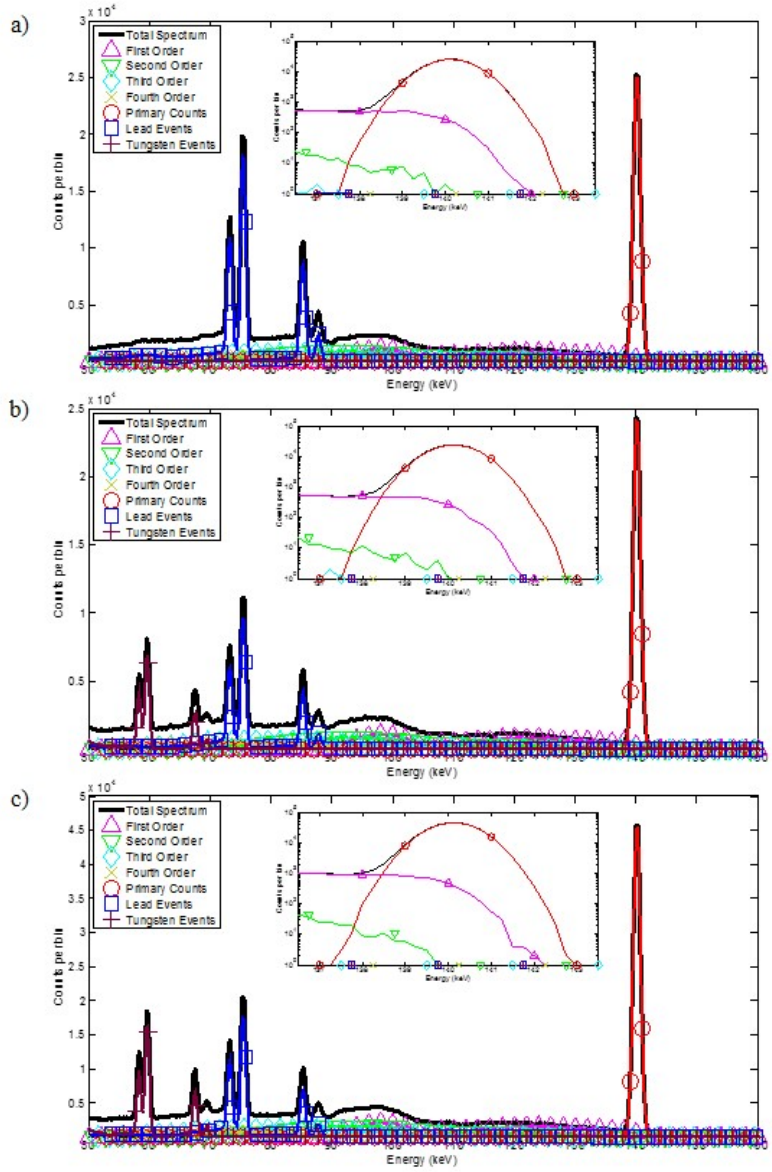

Figure 43: Generated energy spectra parsed by scatter order of the breast/torso phantom acquired with the HPGe detector fixed to select collimators. (a) Hexagonal Lead, (b) Hexagonal Tungsten, (c) Square 2×2 Tungsten Pene. Logarithmic energy spectra insets around the 140 keV photopeak show scatter contributions of generated breast projections. Count scale differences between spectra reflect their count sensitivity differences. Characteristic x-ray peaks for tungsten are observed between 57 keV and 70 keV after substituting out the lead collimator. Applying alternative collimator material and geometry exhibits no differences in relative scatter contributions within the energy windows around the photopeak.

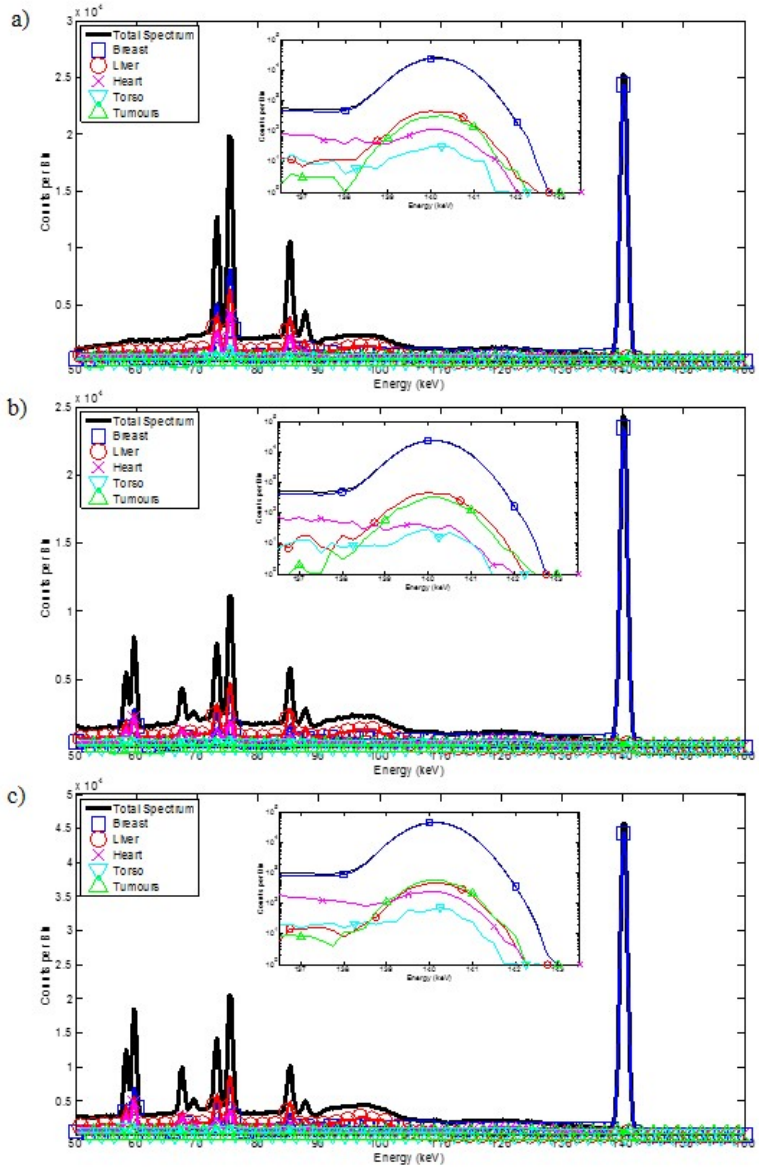

Figure 44: Generated energy spectra parsed by event origin of the breast/torso phantom acquired with the HPGe detector fixed to select collimators. (a) Hexagonal Lead, (b) Hexagonal Tungsten, (c) Square 2×2 Tungsten Pene. Logarithmic energy spectra insets around the 140 keV photopeak show phantom organ contributions of generated breast projections. Count scale differences between spectra reflect their count sensitivity differences. Characteristic x-ray peaks for tungsten are observe between 57 keV and 70 keV after substituting out the lead collimator. Applying alternative collimator material and geometry exhibits no differences in organ contributions within the energy windows around the photopeak.

5.3 Simulation Results

5.3.1 NBI Energy Spectra

Generated energy spectra from the HPGe detector with the standard hexagonal-hole collimator constructed of lead and tungsten and the registered 2×2 square-hole tungsten collimator are displayed in figures 43 and 44. These three energy spectra are compared for spectral differences between equal collimator geometries with an alternative material, and differences between standard hexagonal-hole and registered collimation. As observed in chapter IV, lead collimation produces characteristic x-rays between 75 and 90 keV. Tungsten collimators generate characteristic x-rays between 57 and 70 keV. The characteristic lead x-rays present in the spectrum with tungsten collimation are due to the lead camera shielding.

Similar to previous NBI simulations, the majority of contributions within the specified energy windows around 140 keV are primary counts and first order scattered photons, followed by a small number of second-order scattered photons. Out-of-view organs continue to contribute to generated projections. There are differences in count scale between energy spectra, but this simply reflects the count sensitivity differences between the selected collimators. Overall, there appears to be no qualitative spectral differences around the 140 keV photopeak when tungsten is substituted for lead or when registered collimation is applied.

Normalized relative sensitivities (to the standard hexagonal-hole collimator with the wide energy window), scatter fractions, and torso fractions are shown in tables

Table 13: Collimator performance measures for the ±2.5% energy window.

Collimator Geometry	Collimator Material	Relative Sensitivity	Scatter Fraction	Torso Fraction
Hexagonal Hole	Lead	100%	4.75%	2.89%
Hexagonal Hole	Tungsten	96.11%	4.77%	2.68%
Square 2×2 Pene	Lead	203.45%	4.76%	3.79%
Square 2×2 Pene	Tungsten	181.64%	4.71%	2.27%
Square 2×2 Res	Tungsten	81.39%	4.53%	3.33%
Square 3×3 Pene	Tungsten	133.95%	4.68%	2.26%
Square 3×3 Res	Tungsten	166.26%	4.73%	2.27%

Table 14: Collimator performance measures for the ±1.25% energy window.

Collimator Geometry	Collimator Material	Relative Sensitivity	Scatter Fraction	Torso Fraction
Hexagonal Hole	Lead	97.42%	2.52%	2.58%
Hexagonal Hole	Tungsten	93.61%	2.52%	2.36%
Square 2×2 Pene	Lead	198.09%	2.46%	3.39%
Square 2×2 Pene	Tungsten	176.84%	2.43%	1.88%
Square 2×2 Res	Tungsten	79.41%	2.40%	2.98%
Square 3×3 Pene	Tungsten	130.53%	2.44%	1.90%
Square 3×3 Res	Tungsten	161.81%	2.41%	1.90%

13 and 14. The relative sensitivities observed from the Monte Carlo simulations match those from analytic formulations in table 12. The registered 2×2 square-hole lead collimation with shorter hole length grants the highest count sensitivity, approximately doubling the standard lead hexagonal-hole collimator. Substituting tungsten for lead in this geometry reduces the count sensitivity by ∼20% due to its additional stopping power for gamma rays. For a given energy window, the scatter fractions for each collimator are very similar. There are slight differences in torso fractions between collimators, but overall, the out-of-view contributions are low. In summary, similar to the conclusions of chapter IV, the superb energy resolution of

HPGe detectors allows for high photopeak fractions and tight energy windows for low contributions from object scatter and out-of-view sources.

5.3.2 NBI Projections

The images from the NBI simulations generated with a ±2.5% energy window are displayed in figure 45. There are slight differences in the morphology of the hot spots within each projection image. The collimators with higher resolutions or smaller bore diameters, such as the standard hexagonal-hole and the registered 3×3 collimators, produce narrower hot spots while the thinner, registered 2×2 collimators generally express larger, more spread out, hot spots. Conversely, the high resolution images exhibit higher noise levels compared to the thinner, registered 2×2 collimators. This is seen in the highly-variable background of the tungsten hexagonal-hole collimator and the registered 2×2 with matched resolution to the standard lead collimator. The other alternative collimators exhibit smoother backgrounds due to their high count sensitivities. Most importantly, in terms of tumor detection, all three hot spots are easily observable with each collimator mounted to the modeled HPGe detector.

Tumor contrast and SNR measurements are displayed in figures 46 and 47. Comparing (a) and (b) for both figure 46 and figure 47 shows that utilizing tighter energy windows with the same collimator exhibits a minimal effect on image quality. Due to the large variance on a single contrast and SNR measurement, as signified by the error bars, it is not possible to claim that the image quality of projection produced

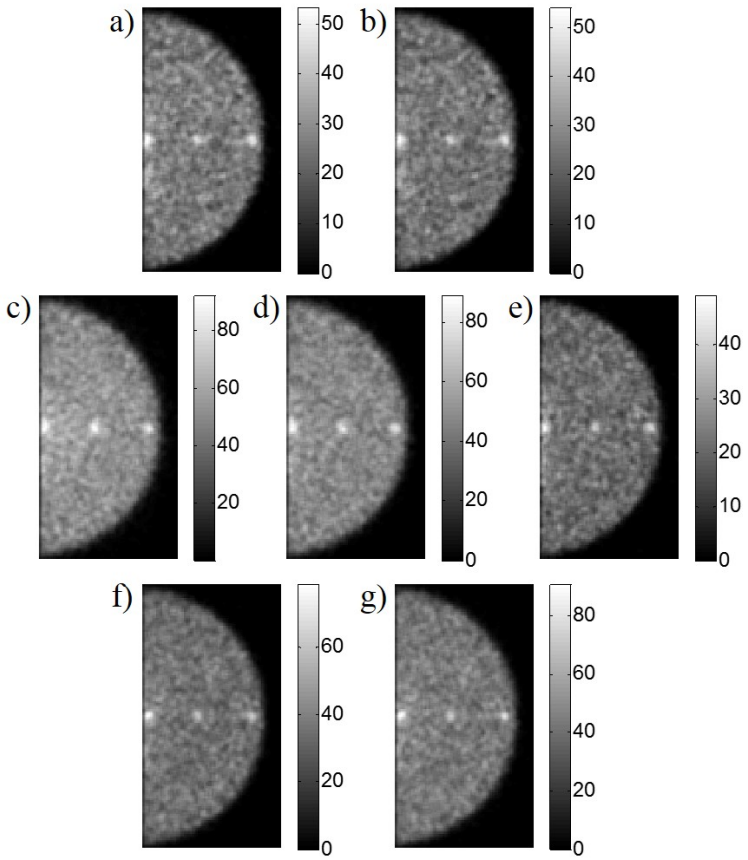

Figure 45: Generated projections of the breast/torso phantom acquired from the HPGe detector with each tested collimator. (a) Hexagonal Lead, (b) Hexagonal Tungsten, (c) Square 2×2 Lead Penetration, (d) Square 2×2 Tungsten Penetration, (e) Square 2×2 Tungsten Resolution, (f) Square 3×3 Tungsten Penetration, (g) Square 3×3 Tungsten Resolution. The three 1-cm diameter tumors are visible in all images. Slight morphological changes in the tumors are observed due to object resolution differences between collimators.

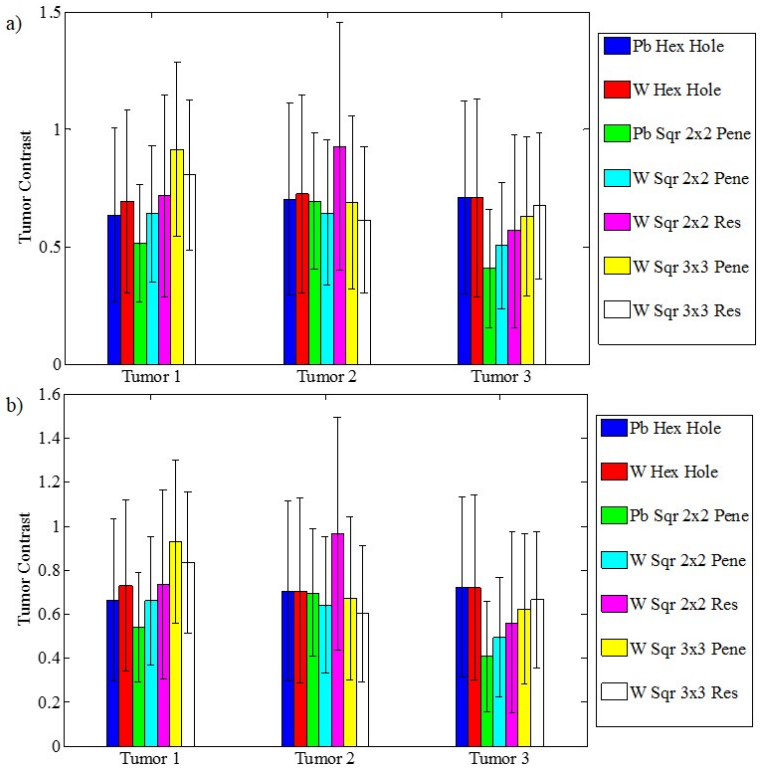

Figure 46: Tumor contrast measurements for the three tumors across each collimator for (a) $\pm 2.5\%$ and (b) $\pm 1.25\%$ energy windows. Error bars correspond to uncorrelated error propagation of Poisson statistics of measured tumor and background signals. There appears to be no change in tumor contrast when tighter energy windows are utilized. Likewise, given the large error bars, there appears to be no difference in tumor contrast between collimators for any given tumor.

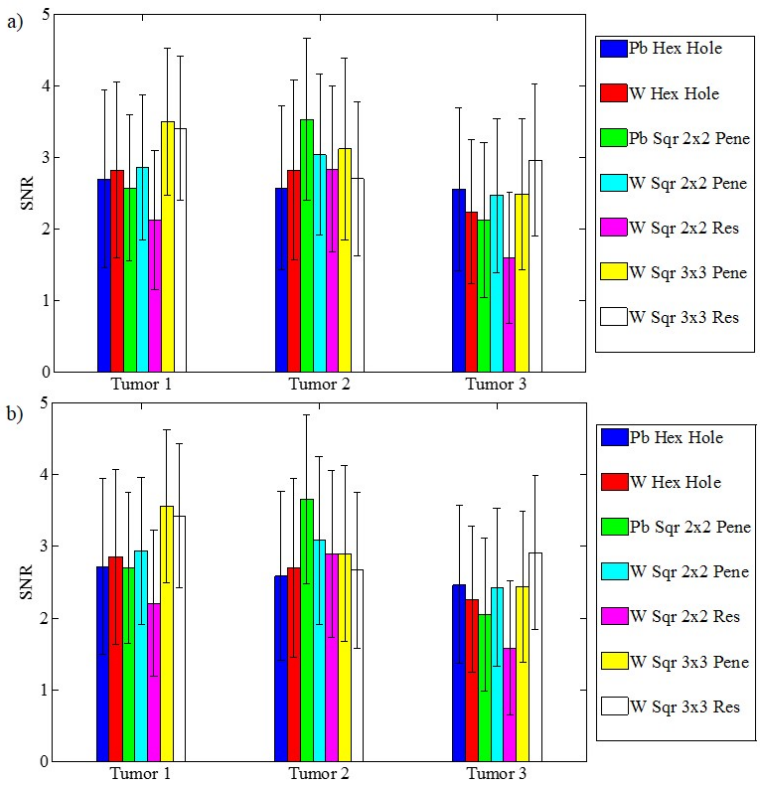

Figure 47: Tumor SNR measurements for the three tumors across each collimator for (a) $\pm 2.5\%$ and (b) $\pm 1.25\%$ energy windows. Error bars correspond to uncorrelated error propagation of Poisson statistics of measured tumor and background signals. There appears to be no change in tumor SNR when tighter energy windows are utilized. Likewise, given the large error bars, there appears to be no difference in tumor SNR between collimators for any given tumor.

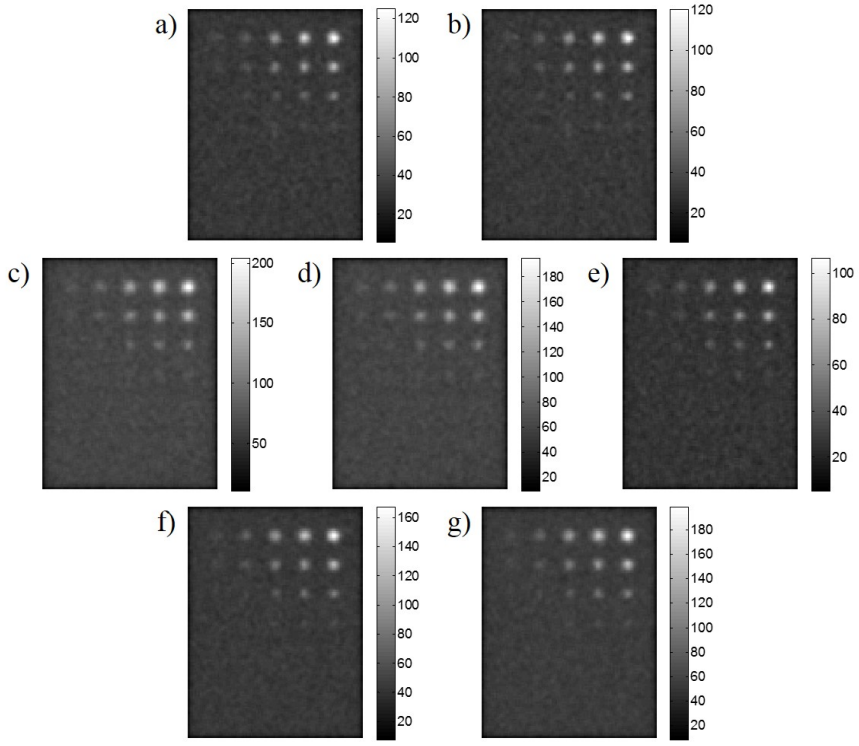

Figure 48: Generated projections of the contrast-detail phantom acquired with the HPGe model with each collimator. (a) Hexagonal Lead, (b) Hexagonal Tungsten, (c) Square 2×2 Lead Penetration, (d) Square 2×2 Tungsten Penetration, (e) Square 2×2 Tungsten Resolution, (f) Square 3×3 Tungsten Penetration, (g) Square 3×3 Tungsten Resolution. The detectability for tumors with each collimator is similar, as the same hot spots are resolved in each image. The collimators are able to resolve 4-mm diameter tumors with TBRs between 10:1 and 20:1, as well as 8-mm diameter tumors with a low TBR of 3:1. The 2-mm diameter tumors are all occult from view.

from one collimator is significantly better than another collimator.

5.3.3 Contrast-Detail Simulations

The images from the contrast-detail simulations generated with a ±2.5% energy window are displayed in figure 48. Line profiles through the centers of the 6 mm tumors and the tumors with a TBR of 10:1 are shown in figure 49. All collimators

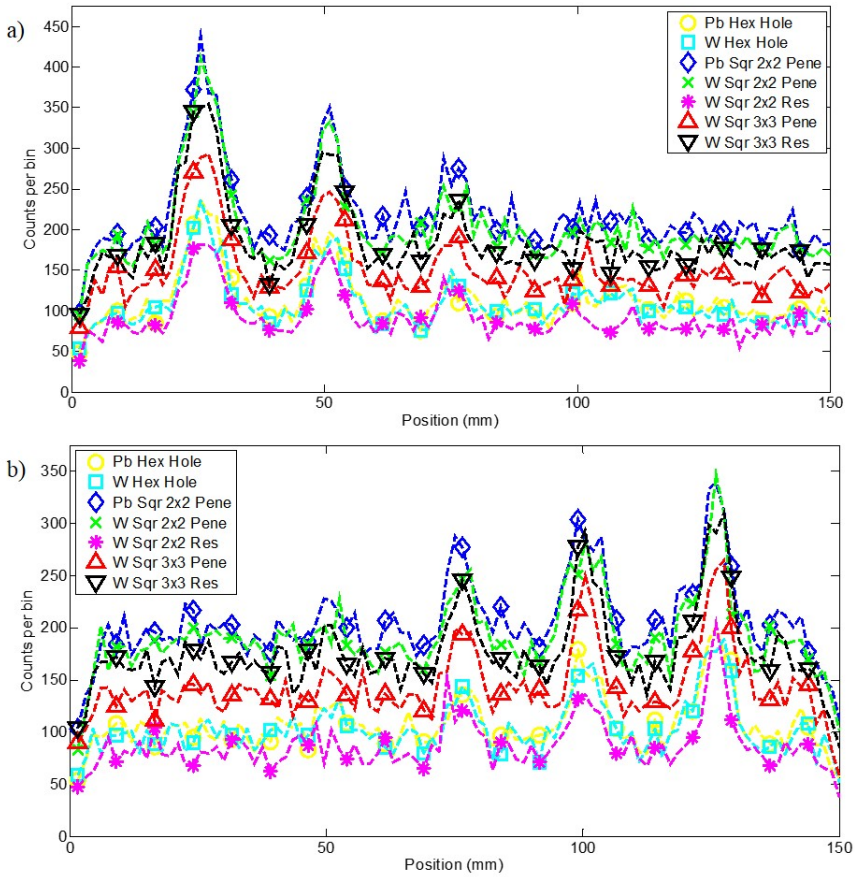

Figure 49: Line profiles through the contrast-detail projections. (a) Vertical line profiles through the tumors with TBRs of 10:1. (b) Horizontal line profiles through the 6-mm diameter tumors. The count sensitivities of the collimators correlate with the background level of each image. The signals from the 4-mm and 2-mm tumors with TBRs of 10:1 and the 6-mm diameter tumors with low TBRs or 3:1 and 5:1 fail to rise above background levels.

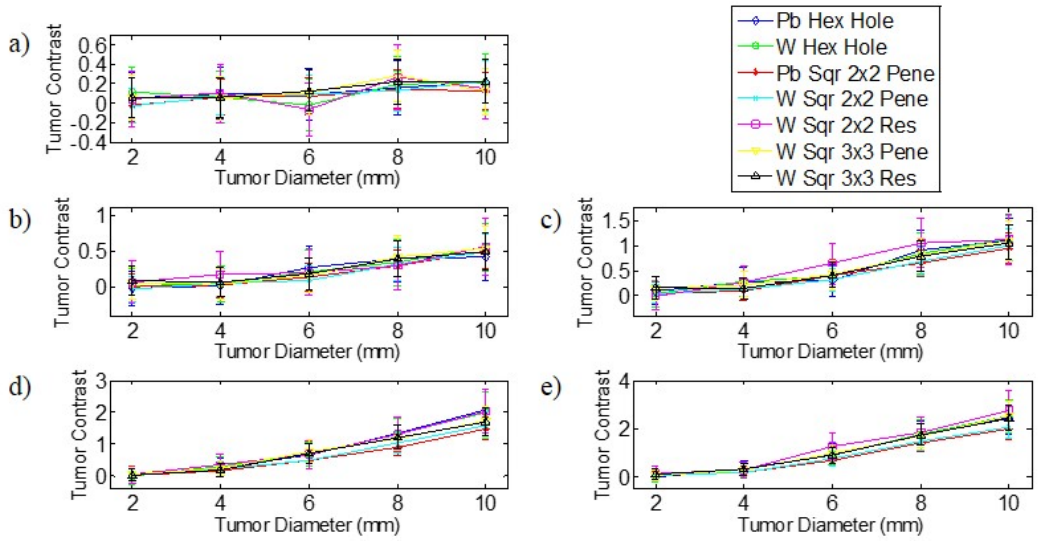

Figure 50: Tumor contrast measurements by tumor diameter from the contrast-detail phantom. (a) 3:1 TBR, (b) 5:1 TBR, (c) 10:1 TBR, (d) 15:1 TBR, (e) 20:1 TBR. Error bars correspond to uncorrelated error propagation of Poisson statistics of measured tumor and background signals. Similar tumor contrast was observed between generated projections.

are able to resolve 4-mm diameter tumors with TBRs between 10:1 and 20:1, as well as 8-mm diameter tumors with a TBR of 3:1. The signals from the 4-mm and 2-mm tumors with TBRs of 10:1 and the 6-mm diameter tumors with low TBRs of 3:1 and 5:1 fail to rise above background levels and appear occult in all images. All 2-mm diameter tumors are also hidden from view. Qualitatively, equivalent performance to detect tumors of various sizes and intensities is observed among the seven collimators.

Displayed in figures 50 and 51 are line plots of the measured tumor contrast and SNR for the various TBR values based on tumor diameter. In general, tumor contrast and SNR increases with tumor size when TBR is held constant. This is not necessarily true for tumors with a TBR of 3:1, as the contrast and SNR values have

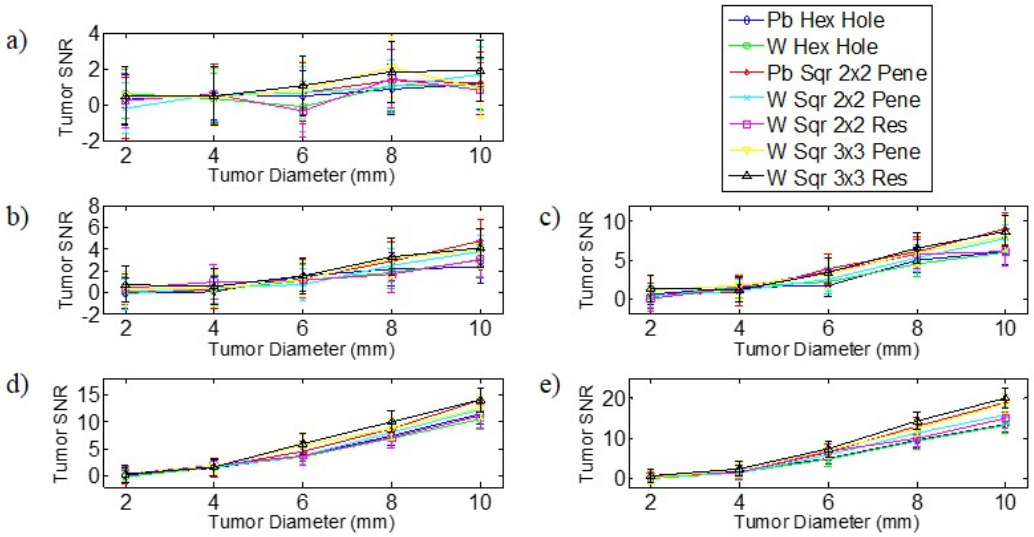

Figure 51: Tumor SNR measurements by tumor diameter from the contrast-detail phantom. (a) 3:1 TBR, (b) 5:1 TBR, (c) 10:1 TBR, (d) 15:1 TBR, (e) 20:1 TBR. Error bars correspond to uncorrelated error propagation of Poisson statistics of measured tumor and background signals. Some separation in SNR is observed for the 10-mm tumors with a TBR of 20:1. All other tumor SNR measurements appear to show no significant difference.

no trend across this diameter range. Generally, the errors associated with these scans signify indistinguishable tumor contrast and SNR between the collimators. There appears to be some separation in SNR for large tumors with high TBR values of 20:1 between some of the registered collimators and the lead and tungsten hexagonal hole collimators. However, for every other case, the image quality of projections acquired with the seven collimators is equivalent.

5.4 Discussion

We have investigated the impact of select, optimal collimators fixed to our modeled HPGe detector on nuclear breast imaging performance. The design of potential

collimators was dictated by registering the square bores to the current size of cross-strip pixels for position-sensitive HPGe detectors, which has been shown to offer the best sensitivity-resolution tradeoff (Tornai et al., 1997; Raghunathan et al., 2005; Weinmann et al., 2009). In addition, we observed the impact of tungsten collimation on imaging performance when swapping lead out and keeping all other physical parameters kept constant. The breast/torso model used in chapter IV and a new contrast-detail phantom were employed to generate projections for these comparisons.

Traditionally, general collimator optimization techniques follow a different procedure than the one employed in this chapter. For parallel-hole collimation, Keller (1968) outlined an approach utilizing the equations of Anger (1967) to optimize the collimator length, bore diameter and septa thickness for a given spatial resolution limit and a certain amount of gamma-ray penetration, usually $\leq$5%. The optimal parameters are independent of hole shape and include terms for material attenuation coefficient, inter-detector spacing, and source distance.

However, this traditional approach does not consider collimator holes registered to the detector pixels, where the sum of collimator bore diameter and septa thickness must equal the pixel pitch of the detector, $p = d + t$. Current HPGe detectors have a strip pitch of 5.0 mm with a 0.25-mm gap between strips. The gaps regions, which are sensitive to charge trapping and incomplete collection, are not explicitly modeled in these simulations, however, we consider their effects and strive to minimize them in the collimation design. Weinmann et al. (2009) used an iterative process to solve for all

collimator parameters by maximizing count sensitivity given a set spatial resolution, minimal penetration, and the registered collimator constraint. Instead of performing an iterative algorithm and allowing for a small range of d and t, the optimal septa thickness was set to 0.25 mm, which fixed the hole diameter at 4.75 mm. This choice of septa thickness should minimize photon interactions within the gap regions beneath the septa and maximize count sensitivity with registered collimation.

A noticeable difference in relative count sensitivity of acquired breast projections was observed between lead and tungsten collimation. With hexagon-shaped holes, the differences were small, only $\sim$4%, while the registered collimator saw a $\sim$20% difference in sensitivity. Because the scatter and torso contributions are relatively equal between the two materials, observed sensitivity differences must be due to more photon penetration through the lead collimators, which is confirmed by the penetration fractions listed in table 12. For a more proper comparison, the parameters for the tungsten hexagonal hole and square 2×2 lead collimators should have been adjusted such that the penetration fractions were equal to their respective counterparts. By merely switching the material and keeping the physical parameters constant, a sensitivity bias was granted to the lead square 2×2 collimator. Considering the image quality of projections acquired with the lead or tungsten collimation, we observed equivalent tumor contrast and SNR. However, the sensitivity gains from penetrating photons in lead collimators can cause unfavorable artifacts in tomographic images when reconstruction algorithms are applied to projections. For this reason, tungsten

collimation is generally preferred over lead collimation.

Only one simulation trial was conducted for each collimator, which is in contrast to the methods of chapter IV, where five trials were conducted for each model. Instead of conducting a statistical analysis to determine significant differences in contrast and SNR, error propagation was performed assuming Poisson statistics and uncorrelated tumor and background signals. Although assuming Poisson distribution for photon counting is reasonable, the assumption of uncorrelated tumor and background signals may be incorrect, as the background signal contributes to the measured tumor signal. For correlated errors to be calculated correctly, a covariance term must be included, which depends upon an unknown joint distribution function of the tumor and background signals. We excluded the covariance term and consider the propagated error as an upper bound on the true error. The true errors may be smaller than calculated, but the errors would need to be reduced by $\sim$50% for clear separation in contrast and SNR between collimators. More simulations will need to be conducted to better understand the true errors on contrast and SNR and definitively determine the image quality of projections for each collimator.

We have observed similar imaging performance among the collimators. For all collimators, nearly equal scatter and torso fractions of approximately 4% and 2% for the larger $\pm$2.5% energy window were measured, respectively. Within propagated error, the tumor contrast and SNR for the breast/torso phantom and the contrast-detail model were equivalent. Moreover, the HPGe detector model was able to detect the

same diameter and TBR range of hot spots within the contrast-detail phantom independent of the collimator used. Even if the errors for tumor contrast and SNR are not accurate, hot spots detection was equivalent across the seven collimators. The only differences in performance between the collimators were observed in measured count sensitivity, where the two thin,registered 2×2 collimators made of lead and tungsten had enhancements of 100% and 81%, respectively, over the standard hexagonal-hole collimator.

Previous studies with other collimator designs determined that high-sensitivity collimation (as opposed to high-resolution collimation) was better for breast imaging (Hruska and O'Connor, 2006a; Gruber et al., 1999). Considering these findings, the results of our simulations suggest that an HPGe camera utilizing a short, registered 2×2 collimator made of tungsten would provide the most benefit for NBI. This collimator provided an enhancement in sensitivity (compared to the hexagonal-hole lead collimator) and low gamma-ray penetration without severely sacrificing spatial resolution, tumor contrast or SNR. Higher resolution breast imaging using the registered 3×3 collimator would still offer improved sensitivity compared to the standard hexagonal-hole collimator, but not to the extent of the registered 2×2 collimator. Ultimately, the sensitivity enhancements using registered collimation may allow for less injected radioactivity, resulting in a reduction of absorbed radiation dose associated with NBI without sacrificing imaging performance.

One feature of the HPGe detector that has not been incorporated into these

simulations is its depth-of-interaction capability. Current pulse processing allows for estimation of absorbed events to 1 mm depths over the 10 mm thickness of the detector. The Hi-Sens architecture for CZT gamma cameras applies an adaptive iterative reconstruction algorithm using the depth information of planar images to further improve the spatial resolution of the system (Robert et al., 2011). This collimation scheme works best with large bore diameters and short collimator lengths, making our choice of collimator a good candidate for investigating a similar strategy with HPGe detectors. Next, we explore similar architectures to take advantage of our depth-of-interaction estimation to further improve the tradeoff between spatial resolution and sensitivity in NBI simulation studies in chapter VI.

5.5 Chapter Summary

In this chapter, simulations were conducted to investigate the feasibility of a realistic HPGe detector with various parallel-hole collimators for NBI. Our choice of registered collimation provided an 81% enhancement in sensitivity and better suppression of events from the torso, heart, and liver than the standard hexagonal-hole collimator, without sacrificing spatial resolution or imaging performance. These results agree favorably with analytic calculations and previously conducted studies using registered collimation in a breast-imaging task. In the next chapter, we exploit the depth-of-interaction capability of HPGe detectors to improve the tradeoff between resolution and sensitivity to ultimately improve the imaging performance of these

systems for NBI.

CHAPTER VI

LIMITED-ANGLE TOMOGRAPHIC BREAST IMAGING WITH A HPGE CAMERA

6.1 Introduction

We have explored registered, tungsten parallel-hole collimators that divide the HPGe orthogonal strips into 2×2 regions with wide acceptance angles that yield improved sensitivity compared to conventional collimators (Campbell and Peterson, 2011). A consequence of selecting large-bore collimation is the sacrifice of geometrical resolution for increased count sensitivity. However, it has been shown that utilizing depth-of-interaction (DOI) information in an iterative reconstruction can compensate for collimator blurring to recover lost spatial resolution, shifting the sensitivity-resolution tradeoff (Guerin et al., 2008). Robert et al. (2010, 2011) showed in simulation that dedicated breast cameras using CZT detectors with electronics that enable DOI estimation, highly-sensitive collimators and an adaptive, iterative reconstruction algorithm can improve count sensitivity by factors between 2-3.3 while maintaining the spatial resolution of standard planar imaging.

The imaging architecture, Hi-Sens, outlined in Guerin et al. (2008) is another form of limited-angle tomography (LAT), where 3-dimensional images are generated without full angular sampling of the object. The contact imaging geometry, as demonstrated with Hi-Sens and in this body of work, has only a single acquisition

view without any camera rotation. Other attempts at limited angle tomographic breast imaging, including the Hybrid SPECT-CT system (Tornai et al., 2003; Perez et al., 2011) and the Dual-Modality Tomosynthesis system (Williams et al., 2010; Gong et al., 2012), have demonstrated some moderate levels of success. These hybrid systems have a limited range of camera rotation around the breast, resulting in reconstructed images with artifacts due to incomplete angular sampling. With poorer angular sampling than Hybrid SPECT and Dual-Modality Tomosynthesis, artifacts may manifest in reconstructed images when contact imaging techniques are employed.

In this chapter, the Hi-Sens architecture is adopted for HPGe detectors. The inherent DOI information collected with HPGe detector projections will be incorporated into our Monte Carlo model. For tomographic imaging, a simulation-generated system matrix will be pre-calculated and utilized with an iterative reconstruction algorithm to form 3D images. We aim to compare the image quality of planar single-photon emission mammography techniques to the 3D position information in a limited-angle tomography scheme with HPGe cameras.

6.2 Methods

6.2.1 Limited-Angle Tomography

A transition from a conventional planar acquisition to a LAT acquisition scheme can be accomplished with 3D position-estimation capability inherent to the HPGe detector and high sensitivity collimation. Figure 52 presents the differences between

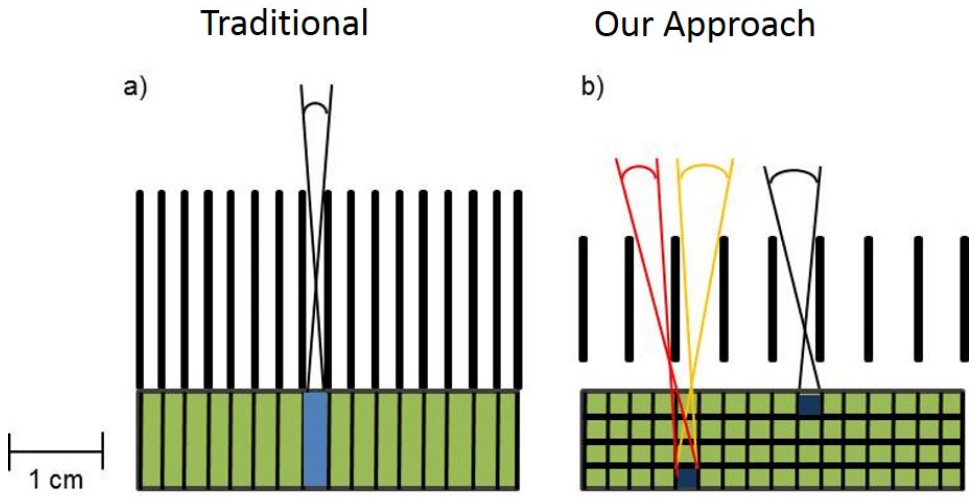

Figure 52: A schematic diagram showing the differences between the (a) traditional planar acquisition and (b) the limited angle tomographic approach. With wider and shorter collimation and a detector with 3D position sensitivity, both non-overlapping and multiplexed data can be collected at different depths for limited-angle tomography.

the traditional planar acquisition with an Anger camera and the novel approach with a detector with DOI information. Wider collimation and position interpolation allows for enhanced angular sampling with varying degrees of multiplexed data by detector depth. An iterative reconstruction algorithm will use the DOI information to compensate for collimation blurring and provide 3D images from a single-view acquisition.

In general terms, tomography is the method of reconstructing a 3D map of some biophysics process within an object from collected 2D projections. Mathematically, this is represented with the inverse linear algebra problem:

$$\mathbf{p} = \mathbf{Hf} + \mathbf{n}, \tag{22}$$

where $\mathbf{p}$ is the projection data collected from the detector, $\mathbf{f}$ is the radioactivity within the object, and $\mathbf{H}$ represents the system matrix that maps or projects the object to the detector. The elements of the system matrix dictate the probability of an event or gamma emission in object voxel f_j is collected in detector voxel p_i. Finally, $\mathbf{n}$ represents the random noise exhibited in projection data. Figure 53 shows a simplified diagram of (22). A solution to the inverse problem can be found using an iterative reconstruction method called the Maximum-Likelihood Estimation-Maximization (MLEM) to estimate $\mathbf{f}$ with the collected projection data $\mathbf{p}$ and some a priori knowledge of the system matrix $\mathbf{H}$ (Rockmore and Macovski, 1976; Shepp and Vardi, 1982; Lange et al., 1984). In element form, the iterative solution of (22) is:

$$f_j^{k+1} = \frac{f_j^k}{\sum_i H_{ij}} \sum_i H_{ij} \frac{p_i}{\sum_j H_{ij} f_j^k}. \tag{23}$$

A vectorized version of (23) can be utilized with MATLAB due to its efficient and expedited matrix calculations:

$$\mathbf{f^{k+1}} = \frac{\mathbf{f^k}}{\sum_i H_{ij}} \mathbf{H^T} \frac{\mathbf{p}}{\mathbf{H f^k}}. \tag{24}$$

In the next section, the method for pre-determining $\mathbf{H}$ will be discussed.

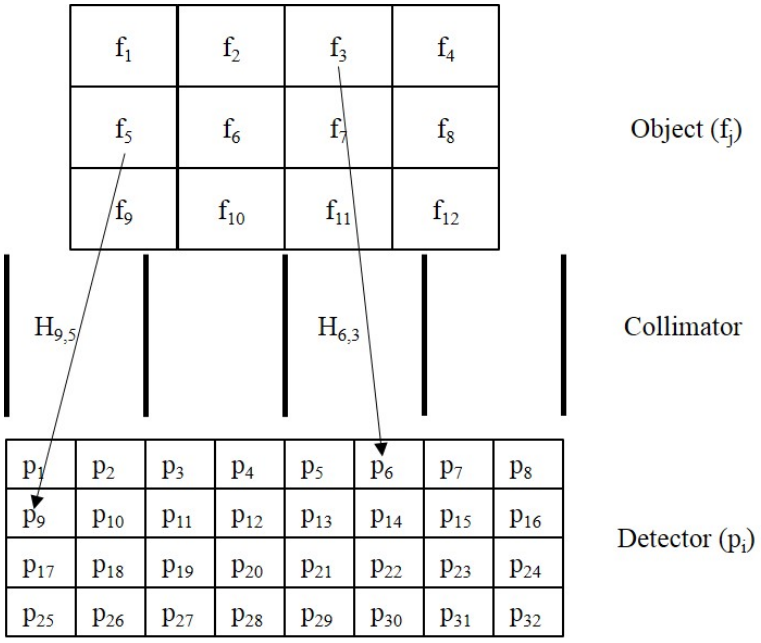

Figure 53: A schematic diagram of the inverse image problem with the voxelized object, voxelized detector and collimator. The elements of the system matrix, **H**, dictate the probability of an event in f_j is collected in p_i.

6.2.2 System Matrix Generation

To apply the MLEM reconstruction algorithm to the HPGe model, a simulated system matrix was calculated. MCNP5 simulations were conducted with a total of 1.9×10^{10} 140-keV gamma rays emitted in an 22.5° cone towards the HPGe detector. Symmetries in the image space allowed for simulating emissions uniformly from only 1/4 of the FOV, which reduced the computational burden. Approximately $5.9\overline{87}\times10^{6}$ gamma rays were emitted from each object voxel to generate point spread functions (PSF). The PSFs originating from 1/4 of the FOV were flipped around the lines of symmetry to produce PSFs for the remainder of the image space. The ratio or fraction of absorbed counts in the PSF to the total number of emissions from an

object voxel determined the elements of the system matrix. 1.82×10^9 total counts comprise the system matrix, with an average of 5,508 counts absorbed across 1,098 detector elements. The 15-cm × 20-cm × 5.5-cm FOV was discretized into 330,000 1-mm × 1-mm × 5-mm voxels. Asymmetrical object voxels were chosen due to the expected poor angular sampling and depth resolution of the FOV. Currently, the 10-mm thick HPGe detectors are discretized into 1-mm depths, so we adopt the same DOI estimation with the HPGe model to have 0.5-mm × 0.5-mm × 1-mm detector voxels. The generated 3.3×10^5 × 1.2×10^6 system matrix was incorporated into the MLEM reconstruction algorithm in order to perform limited-angle tomography using projection data.

6.2.3 Simulation Details

The water breast/torso and contrast-detail phantoms described in chapter V were utilized for Monte Carlo radiation transport simulations. The HPGe detector model described in chapter V was used for this LAT study. To explore the limits and capabilities of the HPGe model in this imaging geometry, given the poor angular sampling and depth resolution, both perfect (no detector blurring) and 1.5 mm intrinsic spatial resolutions were applied to collected projections prior to reconstruction. Only projections from a ±2.5% energy window around the 140-keV were generated. The same projections generated in chapter V were adopted for this work, except the depth information of the collected projections were kept intact. The MLEM reconstruction

algorithm was conducted with 15 iterations. Average normalized mean squared error (NMSE) was calculated using (25) given the known radioactivity concentrations of the breast/torso and contrast-detail phantoms:

$$Average\,NMSE = \frac{1}{n}\sum_{j}^{n}\left(\frac{f_j - g_j}{\overline{g}}\right)^2, \tag{25}$$

where f_j represents a reconstructed image voxel value, g_j is the original phantom voxel value, $\overline{g}$ is the mean value of the original phantom, and n is the number of object voxels within the image, equal to 330,000. Reconstructed images with the lowest average NMSE were selected to generate a reprojected image (projection image integrated by depth) and a maximum-intensity projection (MIP) for comparison to the standard planar projections without DOI interpolation. In the cases that a minimum to the average NMSE was uncertain, contrast and SNR curves by iteration number were generated to determine an appropriate reconstructed image. Contrast and SNR measurements of the reprojected and MIP images were made using (3) and (4). Line profiles normalized by background regions for each contrast-detail image were made to qualitatively assess image quality. Only SNR was calculated for each hot spot for the contrast-detail phantom images. Using SNR as a threshold, detectability curves, showing the number of hot spots with an SNR greater than the threshold value, were generated for each image. A Hough transformation algorithm developed within the Vanderbilt University Institute of Imaging Science (VUIIS) was adopted and applied to detect circles within each image to determine the minimal contrast and size for

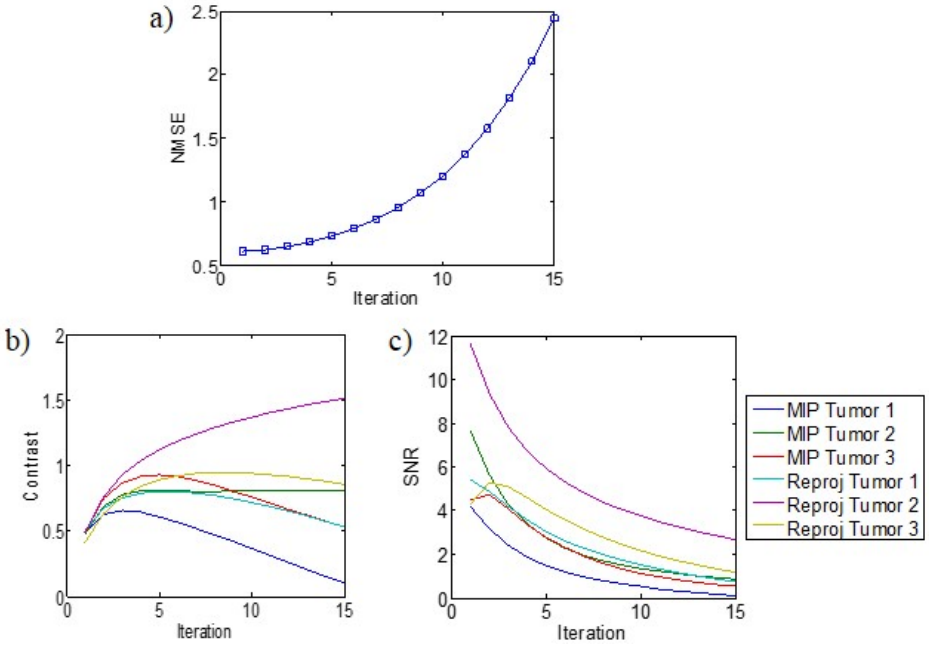

Figure 54: a) The NMSE curve with b) the contrast and c) SNR curves by iteration for the reconstructed breast image with perfect spatial resolution. Because the NMSE curve has a minimum after one MLEM iteration, the contrast and SNR were measured for each reconstruction iteration to determine an accurate image with the best image quality. In general, tumor contrast rises to a maximum after three iterations with some reduction in SNR.

hot spots.

6.3 Results

6.3.1 NBI Simulations

The NMSE and contrast and SNR curves by iteration for the reconstructed breast images with perfect spatial resolution are displayed in figure 54. Because the NMSE has a minimum after a single iteration, there appears to be no benefit to performing a MLEM reconstruction. However, figure 54 suggests that enhancement in tumor

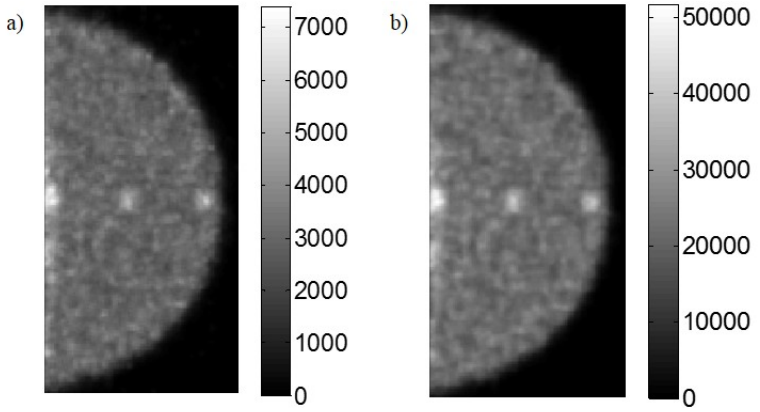

Figure 55: The third iteration of a) the maximum-intensity projection and b) reprojected breast image with perfect spatial resolution after applying a 3×3 mean filter.. Colorbar units are in number of emissions. All three tumors are visible in the reprojected image and MIP, however, image artifacts are observed near the chest wall.

contrast is observed after 3 iterations without large divergence in NMSE or reduction in SNR. Figure 55 shows the reprojected and MIP images from the third MLEM iteration. The breast images appear to be similar, with all three tumors visible above the background. However, the region around tumor 1, near the chest wall, exhibits image artifacts from the heart that suggest either one large tumor or an additional tumor. Tumor contrast and SNR measurements in figure 56 indicate that with perfect spatial resolution, tumor contrast may be similar between the reprojected and MIP images, but that the reprojected image may have some enhancement in tumor SNR.

Figure 57 displays the NMSE, tumor contrast, and SNR curves by iteration. Similar to the case with perfect spatial resolution, NMSE diverges, but tumor contrast improves to a maximum after three MLEM iterations. The resulting planar, reprojected, and MIP breast images are displayed in figure 58. Once again, the breast

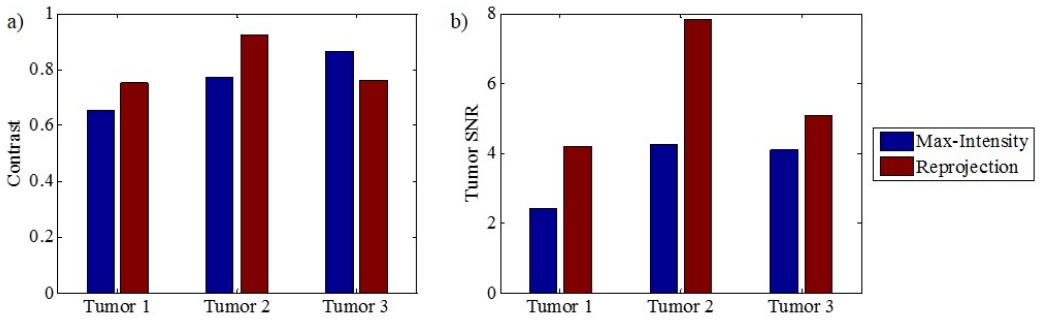

Figure 56: Bar plots of a) tumor contrast and b) SNR measurements for the NBI simulations with perfect spatial resolution. Tumor contrast measurements suggest similar performance between the MIP and reprojected image, however, the reprojected image has superior SNR across all three tumors compared to the generated MIP image.

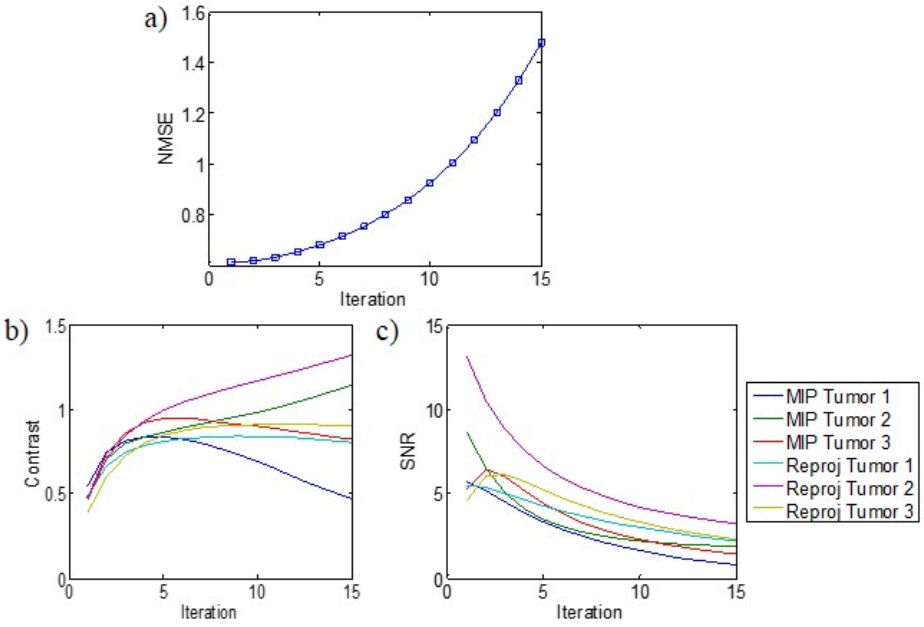

Figure 57: a) The NMSE curve with b) the contrast and c) SNR curves by iteration for the reconstructed breast image with 1.5-mm spatial resolution. Because the NMSE curve has a minimum after a single MLEM iteration, the contrast and SNR were measured for each reconstruction iteration to determine an accurate image with the best image quality. Generally, tumor contrast rises to a maximum after three iterations with some reduction in SNR.

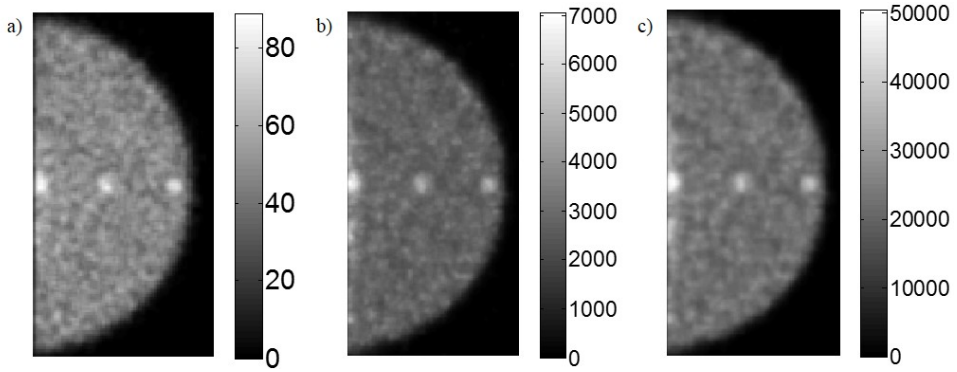

Figure 58: a) The planar projection and the third iteration of b) the maximum-intensity projection and c) reprojected breast image with 1.5 mm spatial resolution after applying a 3×3 mean filter. The colorbar units for the planar projection are counts and the reconstructed images have units of gamma emissions. All three tumors are visible in the planar, reprojected image and MIP, however, image artifacts are observed near the chest wall. The relative background intensity of the planar projection appears higher than the reconstructed images, which could negatively affect contrast.

images display similar information, as all three tumors are visible. The activity originating in the heart contaminates all three images, which could obscure tumors near the chest wall. Qualitatively, the relative background intensity of the planar projection is higher than the two reconstructed breast images, which could negatively affect contrast. The higher tumor contrast and SNR measurements in the LAT breast images, as seen in figure 59, suggest a trend of improved image quality for the MIP and reprojected images over the conventional planar projection.

6.3.2 Contrast-Detail Simulations

Displayed in figure 60 are the NMSE curve, which has a minimum at the 4th iteration, and slices of the reconstructed 3D image with perfect spatial resolution after four iterations. The axial slice of the 3D image resemble previous contrast-

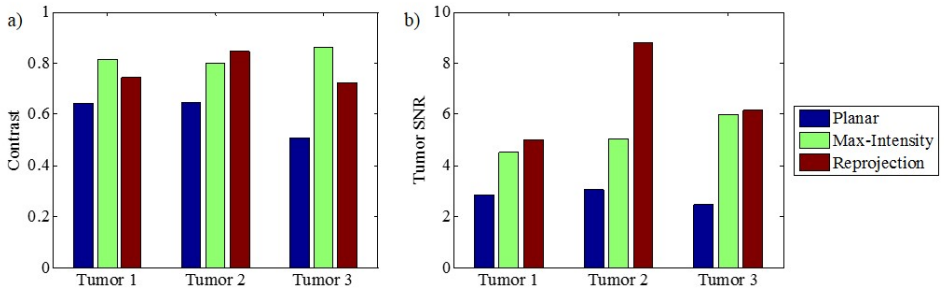

Figure 59: Bar plots of a) tumor contrast and b) SNR measurements for the NBI simulations with 1.5-mm spatial resolution. Once again, tumor contrast measurement indicate similarities between the two reconstructed images, however, both show trends of superior contrast to the planar projections. Likewise, SNR is improved with the LAT images over the planar projections.

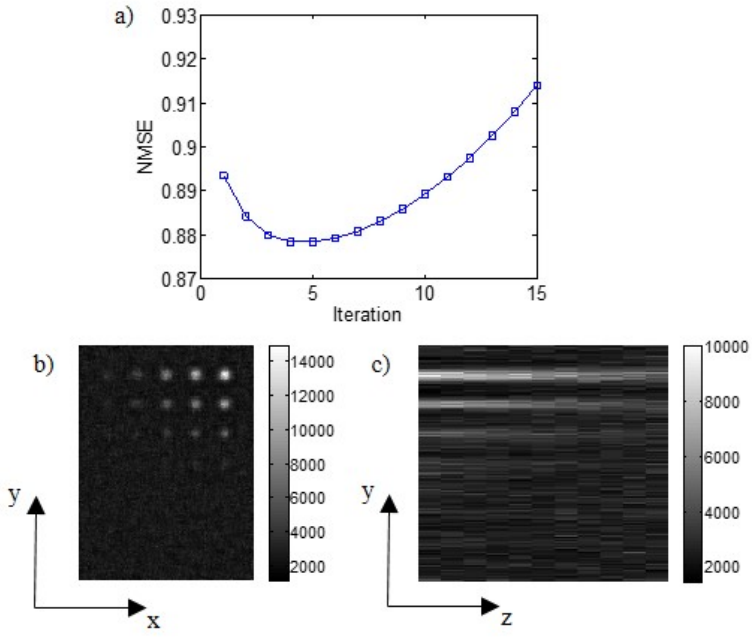

Figure 60: a) The NMSE curve for the contrast-detail image with perfect spatial resolution. The b) axial and c) coronal slices of the 4th iteration, which exhibits the lowest NMSE, are shown. Colorbar units are in number of emissions. The spread of activity along the axial dimension is indicative of the poor angular sampling around the imaging FOV.

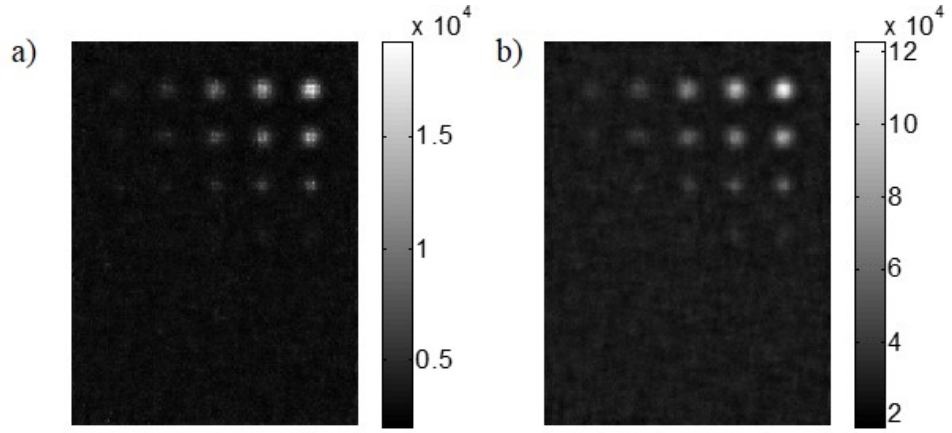

Figure 61: The fourth iteration of a) the maximum-intensity projection and b) the reprojected contrast-detail image with perfect spatial resolution. Colorbar units are in number of emissions.

detail images, however, the coronal slice exhibits blurred activity normal to the HPGe camera due to poor angular sampling around the FOV. Thus, the tomographic image may be unreliable. The reprojected and MIP contrast-detail images, displayed in figure 61, show the 10-mm and 8-mm hot spots with high TBRs above the background, while all the 2-mm and some 4-mm hot spots are occult from view. The line profiles through the 6-mm and 10:1 TBR tumors, shown in figure 62, signify higher signal from hot spots in the generated MIP image over the reprojected image. This observation is mirrored in figure 63, as the hot spots of MIP images tend to have higher SNR measurements than the reprojected image. However, both reconstructed projections have equivalent minimum tumor-detection capability across TBR and tumor diameter ranges.

Introducing the 1.5mm intrinsic spatial resolution has little influence on NMSE,

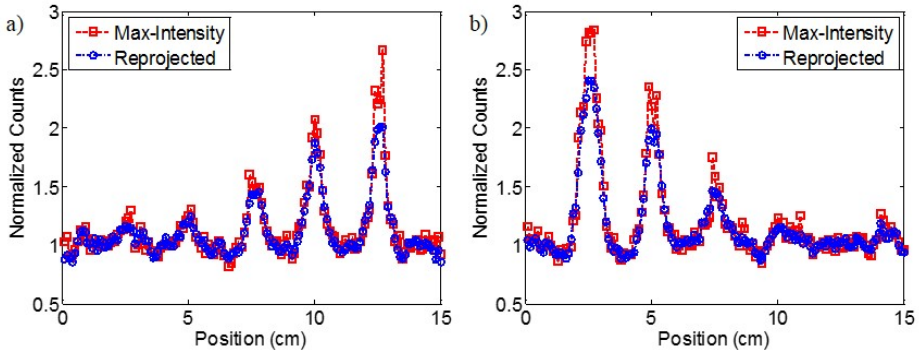

Figure 62: Line profiles through a) the 6-mm and b) the 10:1 TBR hot spots in the reprojected and MIP contrast-detail images with perfect spatial resolution. Each line profile is normalized to its respective background. Generally, signal in the MIP images rises above the reprojected images.

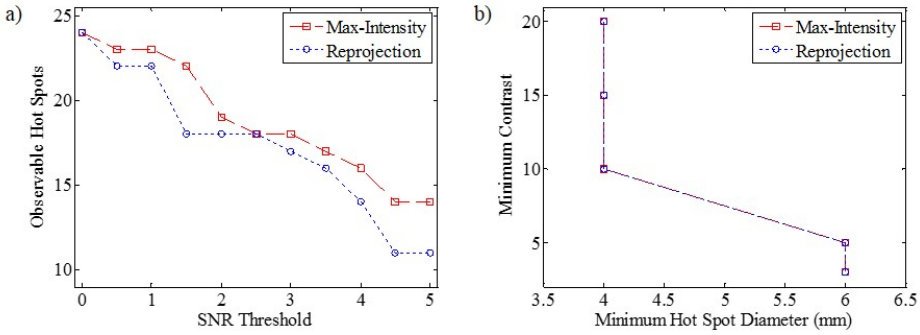

Figure 63: Tumor detectability based upon a) the SNR threshold and b) the minimum TBR and size for the reconstructed contrast-detail projections with perfect spatial resolution. The MIP image shows a trend of hot spots with higher SNR compared to the reprojected LAT image. However, both images share minimum tumor-detection capability.

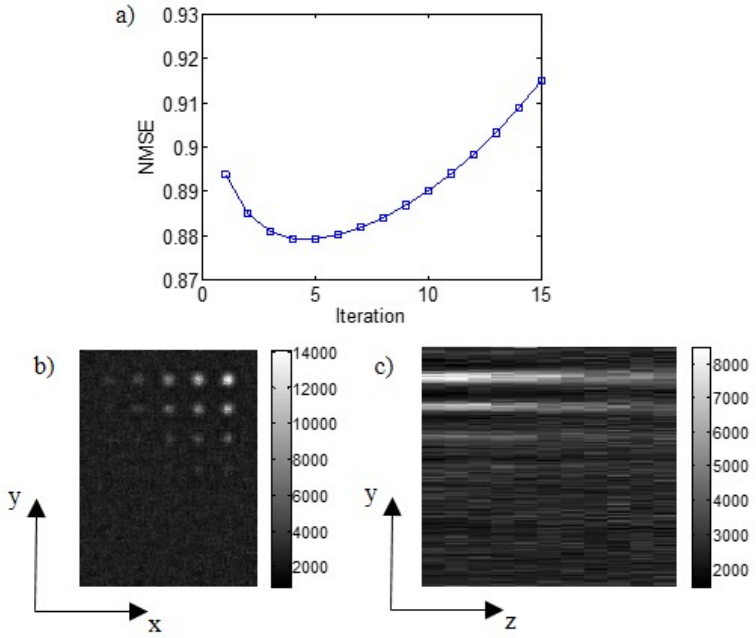

Figure 64: a) The NMSE curve for the contrast-detail image with 1.5-mm spatial resolution. b) The axial and c) the coronal slices of the 4th iteration, which exhibit the lowest NMSE. Colorbar units are in number of emissions. The spread of activity along the axial dimension is indicative of the poor angular sampling around the imaging FOV.

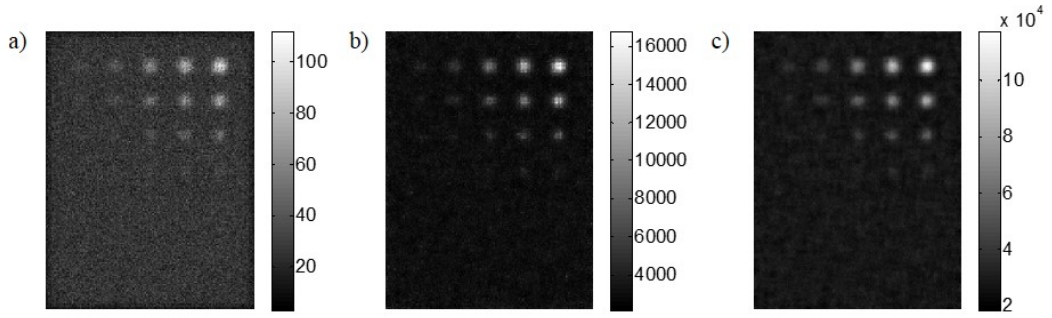

Figure 65: a) The planar projection and the fourth iteration of b) the maximum-intensity projection and c) the reprojected contrast-detail image with 1.5-mm spatial resolution. Colorbar units are in counts for the planar projection and in number of emissions for the reconstructed projections.

as displayed in figure 64. The 4th MLEM iteration still provides the most accurate reconstructed contrast-detail image. The blurred activity normal to the camera still persists in coronal slices, however, the axial slices are reliable. Figure 65 shows the planar, reprojected, and maximum-intensity projections, which have several hot spots present, excluding the 2-mm tumors. Line profiles through the 6-mm and 10:1 TBR tumors in the projections, displayed in figure 66, reveal that the MIP image still grants the highest signal from the tumors over the planar projection and reprojected image. Additionally, the noisy background of the planar projection is prevalent, a feature not exhibited in the reconstructed images. Similar to the detection capability shown in figure 63, figure 67 shows that the MIP continues to exhibit higher SNR than the reprojection and the planar image. Although the LAT images still have equivalent tumor detectability, both the reprojection and MIP outperform the standard planar projection by resolving smaller (6-mm diameter) tumors at a TBR of 5:1 and detecting tumors with TBRs of 3:1.

6.4 Discussion

In this work, an analogous approach to the Hi-Sens architecture described in Guerin et al. (2008) is applied to the HPGe model to investigate the potential benefits of adding DOI information to planar acquisitions. Previous studies exploring the influence of adding DOI information in planar acquisitions with a Cadmium Zinc Telluride (CZT) detector showed improvements to the sensitivity-resolution tradeoff.

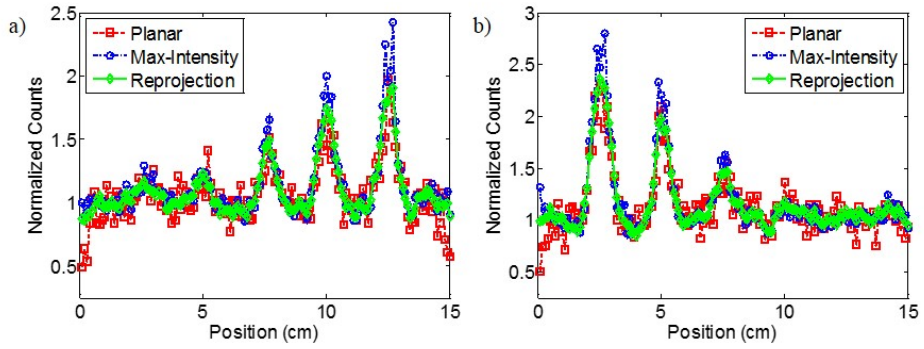

Figure 66: Line profiles through a) the 6-mm and b) the 10:1 TBR hot spots in the planar, reprojected and MIP contrast-detail images with 1.5-mm spatial resolution. Each line profile is normalized to its respective background. Generally, signal in the MIP images rises above the reprojected images. Also, the background of the planar projection is noisier than the LAT images, indicative of lower SNR.

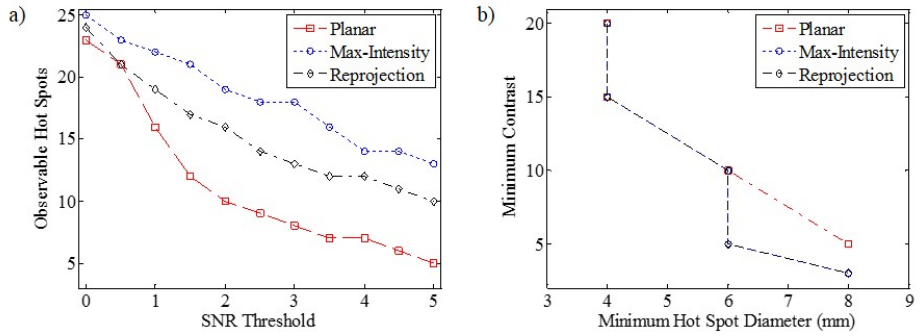

Figure 67: Tumor detectability based upon a) the SNR threshold and b) the minimum TBR and size for the planar, reprojected, and MIP contrast-detail images with 1.5-mm spatial resolution. The MIP image shows a trend of hot spots with higher SNR compared to the planar and reprojected LAT image, however, both reconstructed images have better minimum detection capability than the unprocessed planar projection.

There are several possible advantages to using HPGe detectors in such a scheme. First, our HPGe detector system provides depth information across ten 1-mm depths. Second, because of the good charge transport properties of HPGe detectors, there is potential for higher efficiency due to the lack of energy tailing exhibited in CZT. Finally, because HPGe is a lower-Z, less dense material, counts are more evenly distributed across detector depths, which could improve the quality of the iterative reconstruction. For these reasons, we hypothesize that adopting the limited-angle acquisition scheme would offer additional benefits to image quality.

A weakness in this work is that only one simulation trial is conducted with the breast and contrast-detail phantoms. In contrast to simulations in previous chapters, no error analysis is performed on imaging performance. Normalized mean squared error measurements are made with knowledge of the true emission distribution, but this analysis only assesses the accuracy of the MLEM reconstruction. The MLEM algorithm may introduce additional errors on the reprojected and MIP images other than Poisson noise. Therefore, an error propagation approach may not produce accurate errors for contrast and SNR measurements. For this reason, image quality metrics are only described as trends rather than holding statistical significance.

To explore the potential limitations of image quality and performance, the LAT imaging scheme is applied to generated projections without spatial blurring. The resulting reconstructed images are compared to realistic detector projections with an intrinsic spatial resolution of 1.5mm. The quality of reconstructed 3D images is

equivalent, as evident by the NMSE curves generated. In addition, the trends in image quality are also similar using projections with and without spatial resolution. The minimum detectability measurements suggest that projections with no spatial blurring provide an improvement in the detection of low contrast/TBR tumors compare to projections with 1.5mm resolution. This means that improvements in the lateral position estimation or spatial resolution of HPGe detectors may offer higher sensitivity for tumors with less radiotracer uptake.

Overall, benefits to image quality in the form of improved image contrast, SNR, and detection capability are observed due to the incorporation of DOI information and the iterative MLEM reconstruction. Reprojection of the reconstructed 3D breast images show trends for providing equivalent to higher SNR for hot spots over MIPs. However, MIPs tend to have superior tumor SNR in contrast-detail phantoms. Additionally, the LAT images exhibit better image quality and minimum detection capability for low contrast or TBR tumors than planar acquisitions alone. Therefore, using HPGe detectors with inherent DOI information in a limited-angle tomographic acquisition scheme may offer improved imaging capability for NBI.

The divergence of the reconstructed images from the true emission distribution is a major concern. Improving the quality of images is paramount for developing this acquisition scheme from a specialized screening tool to providing diagnostic information. One reason for the pronounced deviation is the lack of depth resolution in the image space perpendicular to the camera. Potential solutions to address this concern

are numerous. Further refinement of the collimation scheme may provide methods for improving the angular sampling and, thereby, depth resolution and increased quality of reconstructed images. However, an alternative solution may be the addition of a second HPGe camera with an opposing view of the FOV. The second camera would provide high quality image data for regions in close proximity to the camera, as well as enhancements in count sensitivity. We will investigate the performance of a dual-head HPGe imaging system in simulation using our LAT acquisition scheme.

6.5 Chapter Summary

In this chapter, we used simulated data to investigate how employing DOI information in HPGe cameras would affect the quality of generated images compared to conventional planar-projection images. Utilizing a wide-bore collimator and an iterative MLEM reconstruction algorithm with a position-sensitive detector has shown potential for providing equivalent to better image performance for NBI, with higher SNR and detection for low contrast tumors. In the next chapter, we investigate the potential performance of a HPGe breast imaging system using opposing dual-head cameras. We hypothesize that the combining DOI data from two cameras on opposite sides of the FOV may provide enhancements in count sensitivity in addition to improved depth resolution.

CHAPTER VII

A DUAL-HEAD GERMANIUM IMAGING SYSTEM

7.1 Introduction

In previous simulation studies, we investigated using a dedicated HPGe breast camera in a limited-angle tomographic acquisition and observed improved contrast in maximum-intensity projections (Campbell and Peterson, 2012). However, the tomographic images lacked depth information due to the poor angular sampling of the breast. A potential solution to this issue is utilizing a second HPGe camera opposite of the FOV. Dual-head coincidence gamma cameras have been explored and utilized in PET, but using both gamma cameras as stationary single-photon counters for breast imaging has only recently been explored. Opposing dual-head gamma cameras were suggested as the preferred imaging geometry for compressed breast (Majewski et al., 2001). Using NaI(Tl)-PSPMT cameras and multiplicative conjugate counting methods for combining the projections has been shown to provide higher sensitivity for <10mm tumors compared to a single-head imaging system in phantom studies (Majewski et al., 2006; Judy et al., 2007, 2010). An alternative, but novel dual-head imaging system used a NaI(Tl) detector with parallel hole collimation and a smaller CsI detector with focusing pinhole collimation. Sensitivity was greatly increased compared to a single camera and allowed for the detection of tumors that were occult

to the single planar camera (Garibaldi et al., 2008, 2010). A CZT-based dual-head imaging system was used in clinical breast cancer studies and was found to have a 14% increase in sensitivity for <10mm tumors compared to a single camera based upon BI-RADS reader scores (Hruska and O'Connor, 2008a). Furthermore, combining mammography and the CZT dual-head camera increased the absolute sensitivity for breast cancer detection from 27% with mammography alone to 91% (Rhodes et al., 2011).

There are clear advantages to placing a second HPGe camera on the opposite side of the breast in our imaging geometry. An increase in tumor SNR may be observed by approximately doubling the count sensitivity. Photons currently incident upon the lead compression pad could instead contribute to an additional projection image. The second camera would have a closer proximity to tumors that could be occult to the camera inferior to the breast due to attenuation and depth-dependent collimator blurring. These effects could be mitigated with information acquired by the camera superior to the breast, as tumors obscure to one camera may be clearly discernible by the other. Finally, utilizing both sets of projection data in the limited-angle tomographic process could provide similar improvements to tumor contrast and SNR observed in the previous chapter. These potential gains, observed in other dual-head imaging systems, may lead to increased detectability for small tumors using HPGe cameras (Judy et al., 2007; Hruska and O'Connor, 2008a).

In this computational study, we resolve to explore the imaging performance of an

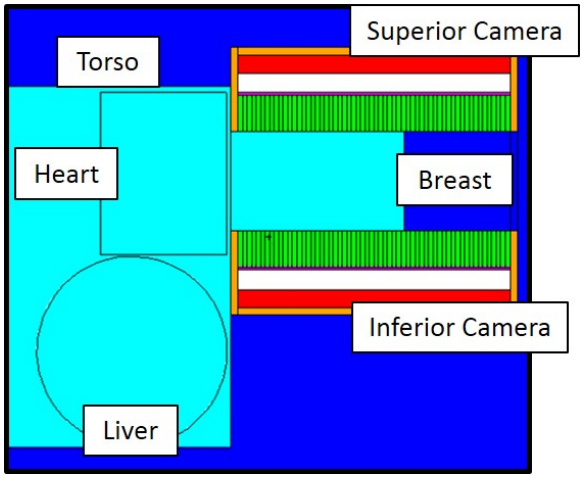

Figure 68: A schematic diagram of the geometry for the Monte Carlo simulations with the dual-head HPGe imaging system. A sagittal view of the inferior and superior detectors (red) and the breast/torso phantom (light blue) with the entire cylindrical liver. Tumors are placed at either 1-cm, 2.25-cm, or 3.5-cm depths. Four-mm thick lead shielding (orange) surrounds the cameras.

opposing dual-head breast imaging system and compare its performance to a single camera. We also strive to explore potential image processing methods using both sets of image data to create viable images. We hypothesize that the addition of a second HPGe camera will offer approximately double the count sensitivity of the single camera. Moreover, the sensitivity gains of the dual-camera system are expected to translate into improvements in tumor SNR and provide better tumor detectability in reconstructed images. These findings could provide motivation for the pursuit of fabricating and manufacturing dedicated HPGe cameras for breast cancer imaging.

7.2 Methods

The HPGe camera model described in chapter VI is adopted for modeling a dual-head breast imaging system. Given the expected poor angular sampling and depth resolution, both perfect (no blurring) and 1.5 mm intrinsic spatial resolutions are applied to collected projections. Displayed in figure 68 is a schematic of the dual-head imaging system model. Instead of a lead compression pad, a second HPGe camera head superior to the breast is substituted. The second camera has the same architecture and performance to the inferior camera, including the tungsten parallel-hole collimator, the aluminum entrance window, the inter-detector vacuum space, the lead shielding and the same HPGe detector. Rather than mirroring the first HPGe camera across the FOV, the superior camera is treated as the first camera rotated around the sagittal axis. This serves to maintain the parity for images applied to the iterative reconstruction algorithm, explained in section 7.2.1.

This work strives to investigate the advantages of using two opposing cameras to acquire images of a common FOV. Part of this investigation is discerning the potential benefits of the second set of projection data from the superior camera by leveraging it with appropriate processing methods. To this effort, we first compare the performance of the planar projections individually. Conjugate counting methods are used to combine projections of opposite-view cameras, which suppress attenuation effects and diverging profiles to generate a single planar image. The arithmetic (average)

and geometric mean images are generated using (26) and (27):

$$\overline{I_A} = \frac{I_1 + I_2}{2} \tag{26}$$

$$\overline{I_G} = \sqrt{I_1 \times I_2}, \tag{27}$$

where I_1 and I_2 are the count values of opposing pixels in the inferior and superior cameras, respectively. Finally, the limited-angle tomography acquisition scheme is expanded to include the inferior and superior projections. An Ordered-Subset Expectation Maximization (OSEM) reconstruction is applied to the collected projections to generate 3D images (Hudson and Larkin, 1994). Because the tomographic image is expected to be unreliable, the 3D image is used to generate a reprojection and MIP image to collapse the depth information into 2D projections.

7.2.1 OSEM Reconstruction

With the addition of the second camera, augmenting the reconstruction algorithm is essential to incorporating the second set of projection data. Instead of using an MLEM algorithm, an OSEM reconstruction is utilized to include both inferior and superior projection data to generate a tomographic image. Mathematically, the OSEM solution to the inverse image problem is the following:

$$f_j^{k+1} = \frac{f_j^k}{\sum_{i \in S} H_{ij}} \sum_{i \in S} H_{ij} \frac{p_i}{\sum_j H_{ij} f_j^k}, \tag{28}$$

where S refers to all detector pixels within the current subset. A vectorized version of (28) can also be utilized with MATLAB:

$$\mathbf{f^{k+1}} = \frac{\mathbf{f^k}}{\sum_{i \in S} H_{ij}} \mathbf{H^T} \frac{\mathbf{p}}{\mathbf{H f^k}}. \tag{29}$$

For the OSEM algorithm, each camera projection is considered an individual subset, resulting in two subsets per iteration. OSEM reconstruction consists of the following steps: The MLEM algorithm is applied to the inferior camera subset first as a sub-iteration. The resulting image is then rotated around the sagittal axis to align with the second camera. This enables continual use of the pre-computed system matrix without alteration. This rotated image is used as the initial guess in the MLEM algorithm with the second subset of projection data from the superior camera. The result of the second MLEM sub-iteration is a full OSEM iteration and the process is repeated.

7.2.2 Phantom Details

The breast/torso phantom originally described in chapter IV is augmented for use with the dual-head camera model. Recall that the phantom was truncated due to the low liver contribution to inferior-camera projections, which also expedited the Monte Carlo simulations. Because the superior camera points toward the liver and lower torso, events in these regions may contribute to collected projections. Thus, the entirety of the liver and torso is included the in phantom. This extends the length of

Table 15: Source definitions for the breast phantom with the dual-head HPGe model.

Organ	Volume (mL)	Activity Concentration	Emission Probability
Liver	1200	80	0.88
Heart	250	15	0.04
Torso	6450	1	0.06
Breast	796	1	0.007
Tumors	0.524	5	2.4×10^{-5}

the torso to 20 cm, resulting in a cubic torso of 20 cm $\times$ 20 cm $\times$ 20 cm and the full liver with dimensions in section 4.3.1. Three different breast phantoms are simulated with 1-cm diameter tumors placed either at a depth of 1 cm from the inferior camera, 2.25 cm, equal-distant to both cameras, or 3.5 cm from the inferior camera, which is 1 cm from the superior camera. Tumors and organ parameters for the phantom are displayed in table 15. A total of 8.4×10^{10} 140-keV photons are emitted isotropically from the breast/torso phantom, generating projections with $\sim$1800 counts/cm^2 count density.

The contrast-detail phantom first described in chapter V is adapted to the dual-head imaging system. Similar to the first contrast-detail phantom with tumors at a 1-cm depth from the inferior camera, a second version places tumors at the center of the FOV, equal-distant from both cameras. 2.0×10^8 140-keV photons are emitted in a cone beam with 22.5° half angle towards both the inferior and superior cameras to generate projections from both set of contrast-detail phantoms.

7.2.3 Simulation Measurements and Analysis

Simulated energy spectra parsed by scatter order and event origin are acquired from the breast simulation for both cameras. An energy window of ±2.5% around the 140-keV photopeak is applied to discriminate against events which fail to deposit sufficient energy. Camera projections for both the inferior and superior cameras are collected for all phantoms described in section 7.2.2. Relative sensitivity, averaged over the three breast phantoms and normalized to the inferior camera, scatter, and torso fractions are calculated for the inferior and superior projections. Planar projections for both cameras were generated by summing counts by detector depth. The average and geometric projections are generated using the planar projection data and applying (26) and (27). The OSEM reconstruction algorithm in (29) was applied to the inferior and superior projections with DOI information left intact to generate 3D images. Average NMSE was calculated using (25) to determine the most accurate 3D image, which in turn is used to generate the reprojected and MIP images. Average tumor contrast and SNR were calculated using (3) and (4) for NBI images. For the contrast-detail phantom images, SNR was calculated for each hot spot. Using SNR as a threshold, detectability curves, showing the number of hot spots with a given SNR value are generated for each projection. The Hough transform algorithm developed within the VUIIS was applied to contrast-detail projections to determine the minimal contrast and size for detectable hot spots.

Table 16: Relative count sensitivity, scatter, and torso fraction measurements.

Camera	Relative Sensitivity	Scatter Fraction	Torso Fraction
Inferior	100%	4.84%	2.98%
Superior	105.68%	7.90%	8.52%

7.3 Results

7.3.1 NBI Simulations

Figures 69 and 70 show the logarithmic energy spectra for both HPGe cameras parsed by scatter order and event origin. The relative sensitivity and the scatter and torso fractions are tallied in table 16. The addition of the superior camera grants an increase of 105% in count sensitivity, nearly doubling the number of recorded events. According to both scatter order spectra, the majority of events in the 140-keV photopeak are primary counts, followed by first and second order scattered photons. The event origin spectra reveals that different organs outside of the field of view contribute to collected projections. The inferior camera still captures counts from the liver and heart due to gamma rays penetrating the lead shielding and through small-angle scatters from the heart. However, the superior camera has a larger contribution of liver events due to its high radioactivity concentration and many lines of sight, resulting in large scatter and torso fractions for the superior camera.

Displayed in figure 71 are the breast projections without spatial resolution from the dual-head model with the tumors located at different depths. The intensity of the hot spots in each image are inversely proportional to the distance between the

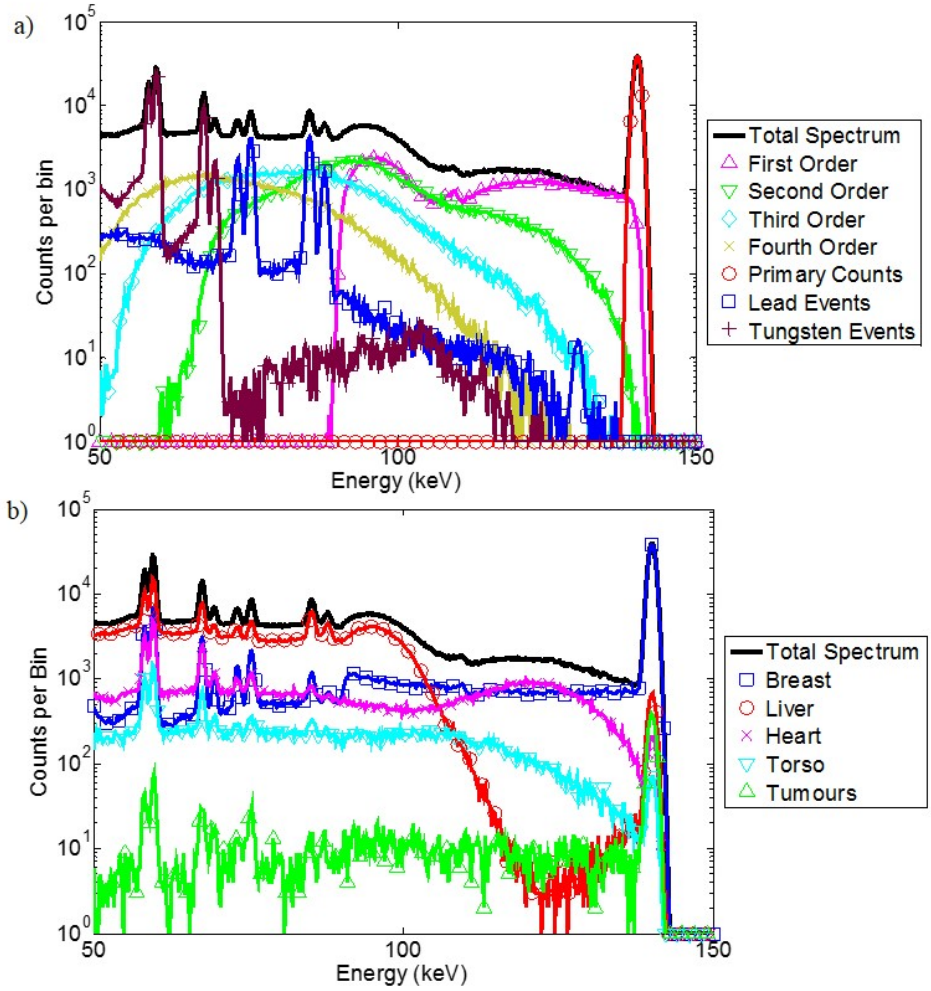

Figure 69: Energy spectra acquired with the inferior HPGe camera from the breast imaging simulations parsed by a) scatter order and b) event origin. The 140-keV photopeak, and subsequent projection, contains mostly primary and first order scattered photons that originate from the breast. Gamma-rays from the organs in the torso penetrate through the lead shielding and contribute to the image projection.

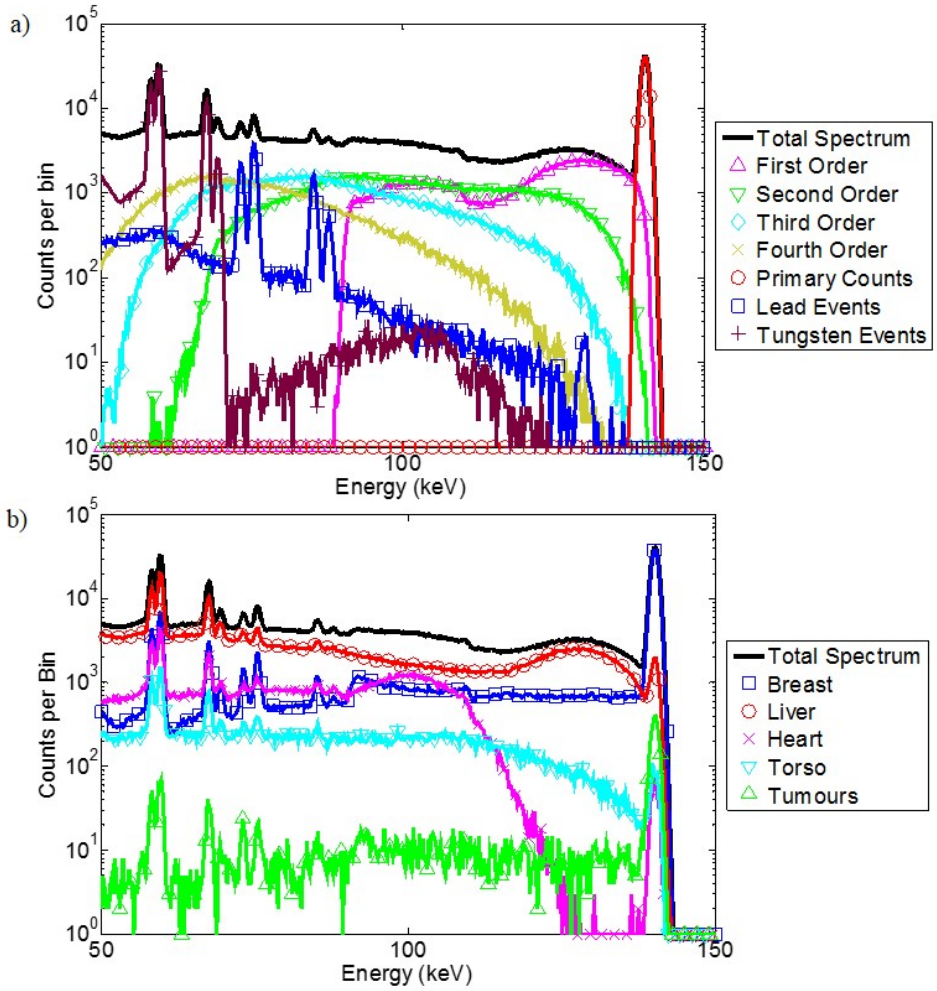

Figure 70: Energy spectra acquired with the superior HPGe camera from the breast imaging simulations parsed by a) scatter order and b) event origin. The 140-keV photopeak, and subsequent projection, consists of mostly primary and first order scattered photons that originate from the breast and liver, respectively.

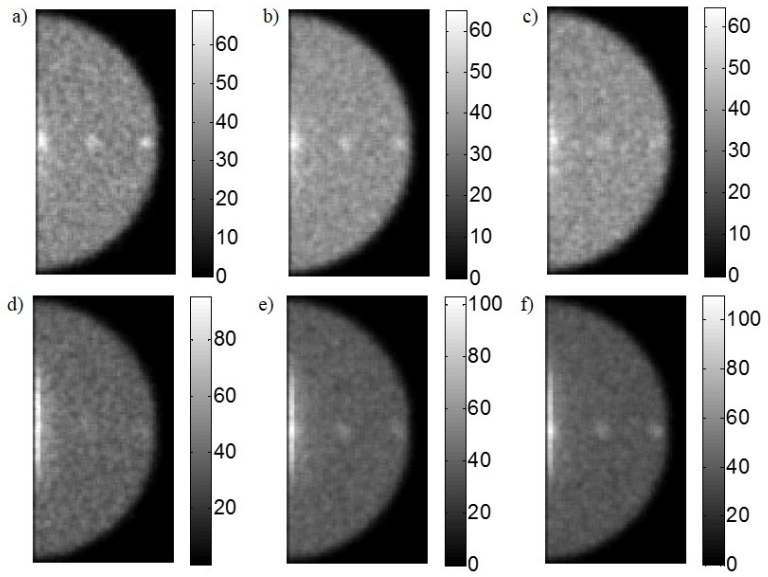

Figure 71: Generated projections of the breast phantom with perfect resolution. Top row: Inferior camera projections with tumors at a) 1-cm, b) 2.25-cm, and c) 3.5-cm depth. Bottom row: Superior camera projections with tumors at d) 1-cm, e) 2.25-cm, and f) 3.5-cm depth. Colorbar units are in counts. Brightness of hot spots correlate with detector distance from tumors. Superior projections exhibit a haze of high counts along the chest wall.

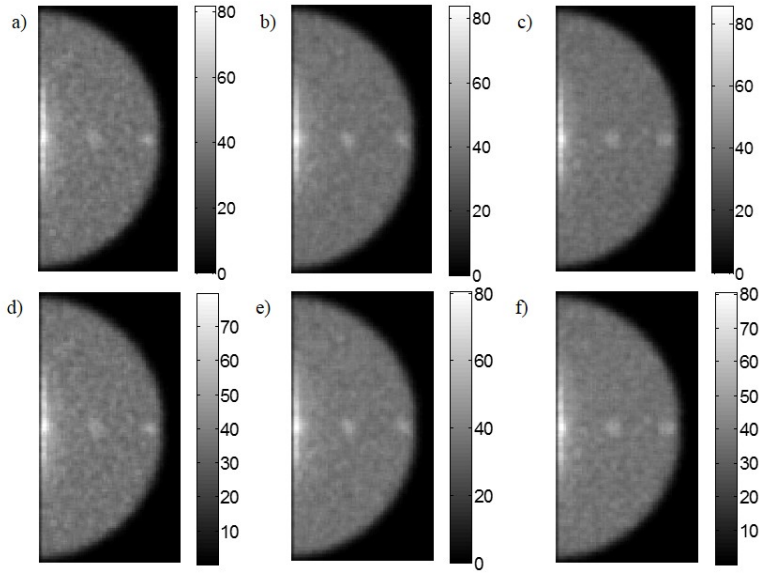

Figure 72: Breast images with perfect spatial resolution generated using conjugate counting methods. Top row: Average projections with tumors at a) 1-cm, b) 2.25-cm, and c) 3.5-cm depth. Bottom row: Geometric mean projections with tumors at d) 1-cm, e) 2.25-cm, and f) 3.5-cm depth. Colorbar units are in counts. All six images exhibit similar qualities. The region of high intensity counts along the chest wall encompasses tumor 1. However, tumor 2 and 3 are observable.

HPGe camera and the tumors in the phantom. The projection of the tumors 1 cm from the inferior camera are visible, while conversely, the tumors 3.5 cm from the superior camera are hidden from view. However, the region of high-intensity counts close to the chest wall heavily contaminates the superior projections and obscures the appearance of tumor 1. Despite the liver artifact, tumors 2 and 3 are visible when close to the superior camera and in the center of the FOV.

The projections generated with perfect resolution using the conjugate counting methods are displayed in figure 72. The average and geometric images are all qualitatively similar, as the conjugate counting technique is designed to suppress attenuation

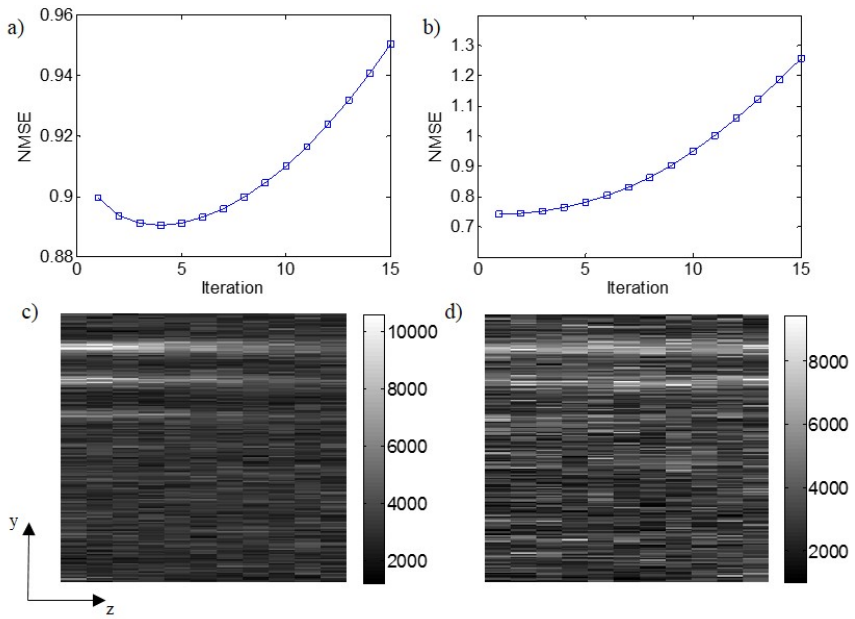

Figure 73: a) The NMSE curve and b) the contrast by iteration curve for the breast images with perfect resolution following OSEM reconstruction. Three OSEM iterations offer enhancements to contrast measurements for the resulting MIP and reprojected images without complete NMSE divergence.

effects and generate depth-independent images. Tumors 2 and 3 are discernible, but the combined images also exhibit the liver artifact from the superior projections that conceals tumor 1.

Applying the OSEM reconstruction algorithm to the inferior and superior projections results in a NMSE and contrast by iteration, as shown in figure 73. After three OSEM iterations, contrast for the hot spots in reprojected and MIP images are enhanced with little divergence from the minimum NMSE. Projections of the reconstructed image after three iterations are displayed in figure 74. The six reconstructed projections exhibit similar features. Tumor 2 and 3 are visible in all six images, independent of the depth of the tumors. The artifact along the chest wall, originally

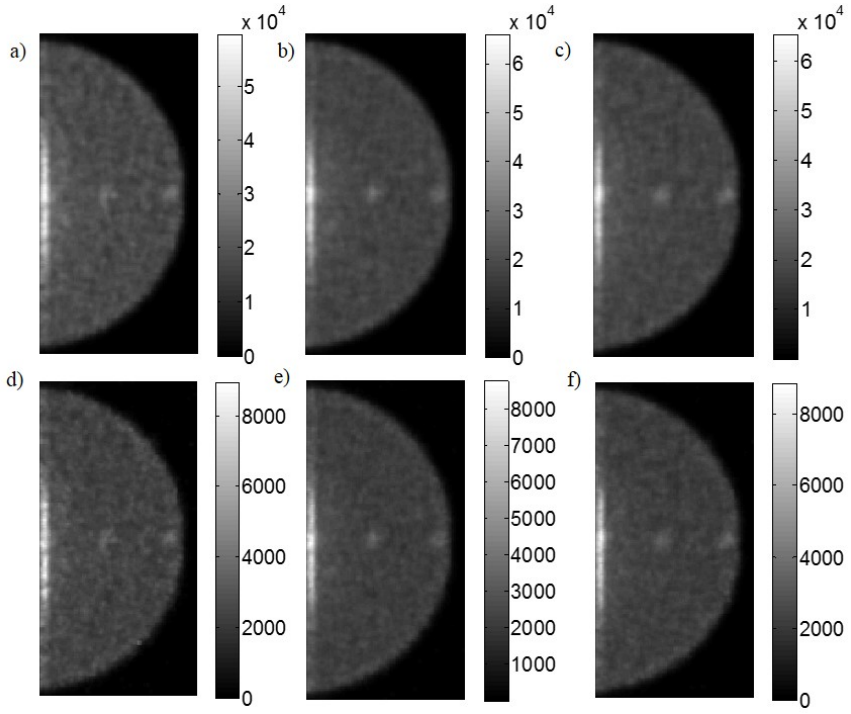

Figure 74: Reconstructed breast phantom projections with perfect spatial resolution generated using an OSEM reconstruction algorithm. Top row: Reprojected images with tumors at a) 1-cm, b) 2.25-cm, and c) 3.5-cm depth. Bottom row: Maximum-intensity projections with tumors at d) 1-cm, e) 2.25-cm, and f) 3.5-cm depth. Color-bar units are in number of emissions. Tumor 2 and 3 are observable in all six images. The large artifact encompassing tumor 1 is also expressed.

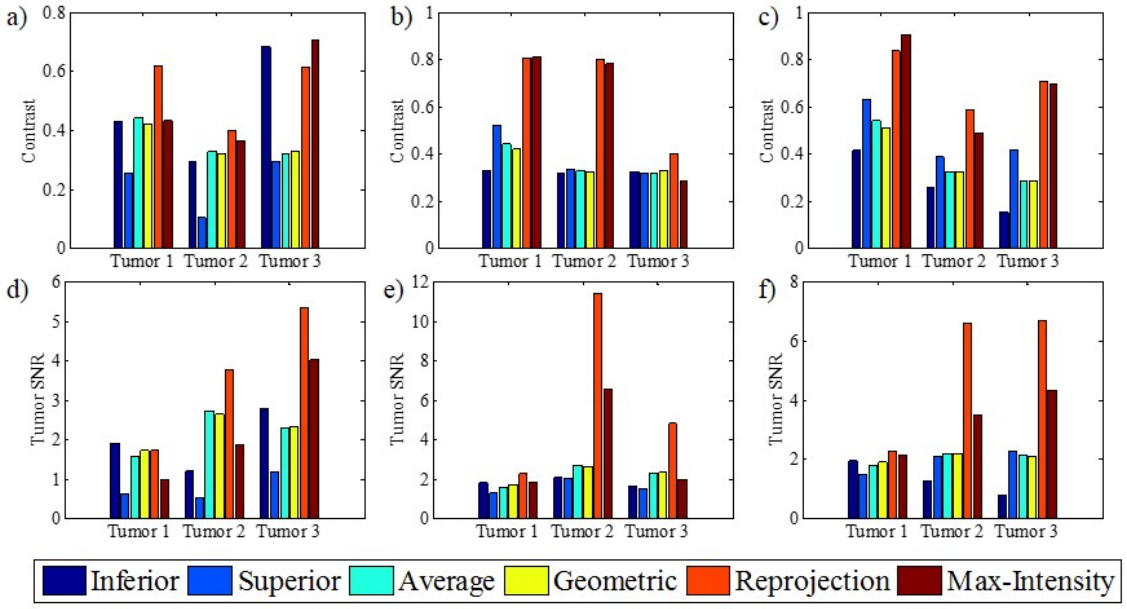

Figure 75: Image quality metrics of hot spots in breast projections with prefect resolution. Contrast measurements of tumors at depths of a) 1 cm, b) 2.25 cm, and c) 3.5 cm. SNR measurements of tumors at depths of d) 1 cm, e) 2.25 cm, f) 3.5 cm. Generally, the reconstructed reprojection and MIP exhibit the highest contrast and SNR for tumors at a given depth.

expressed in the superior projection, is present in all reconstructed projections and contributes to the signal of tumor 1.

Tumor contrast and SNR measurements for all resolution-free projections are shown in figure 75. Comparing the contrast and SNR of hot spots in the individual camera projections, the conjugate counting projections, and the reconstructed projections, we observe the expected trends based on the position of the tumors relative to the cameras. Tumors close to the inferior camera have higher contrast and SNR than the superior camera and vice versa for tumors close to the superior camera. The average and geometric mean images have equivalent image quality and generally

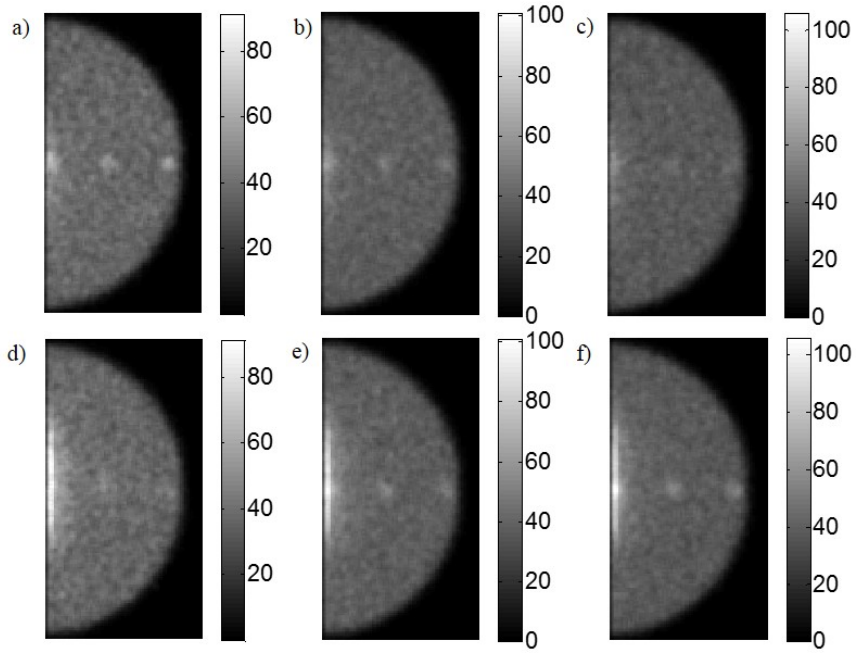

Figure 76: Generated projections of the breast phantom with 1.5-mm spatial resolution. Top row: Inferior camera projections with tumors at a) 1-cm, b) 2.25-cm, and c) 3.5-cm depth. Bottom row: Superior camera projections with tumors at d) 1-cm, e) 2.25-cm, and f) 3.5-cm depth. Colorbar units are in counts. The brightness of hot spots in the projections are inversely correlated with detector distance from tumors. Superior projections exhibit a haze of high counts along the chest wall, most lilely due to contributions from the liver.

have similar to better contrast and SNR than one of the individual cameras alone. The reconstructed projections tend to exhibit the highest contrast and SNR across the three tumors at different depths, with the reprojection having the highest image quality among the six different projections.

Figure 76 highlights the breast phantom projections with 1.5-mm spatial resolution from the individual cameras. The salient features of the inferior and superior projections present in the resolution-free projections are present in these projections. The intensity of the hot spots are inversely correlated to the tumor-to-detector dis-

tance and the contamination from the liver organ in the superior projections is present. Spatially blurring activity appears to have minimal effect on the quality of the collected projections. The result of nominal qualitative effects of spatial resolution on projections is mirrored with the average and geometric mean images, displayed in figure 77. The tumors at the center and near the surface of the breast are observable in this set of combined images, independent of their depth within the phantom. The high-count region along the chest wall is still present and obscures the tumor at that location. Overall, spatial resolution has negligible impact on the qualitative nature of the projection-based images.

Figure 78 indicates that four OSEM iterations grant a considerable increase in tumor contrast with reasonable accuracy compared to the first iteration. The generated reprojection and MIP images from the fourth OSEM iteration in figure 79 have the same traits as the reconstructed projections with no spatial blurring. The reconstruction is able to resolve the tumors at the 1-cm, 2.25-cm, and 3.5-cm depths, however, tumor 1 may be occult from view due to the liver contributions.

The contrast and SNR measurements for the projections with 1.5-mm resolution are displayed in figure 80. Similar trends in contrast and SNR are observed compared to the resolution-free projections. Contrast measurements are higher for tumors in close proximity to the camera in individual projections, while tumors at the center depth are nearly equivalent. The conjugate counting projections have indistinguishable contrast and SNR measurements, which are the average of the inferior and

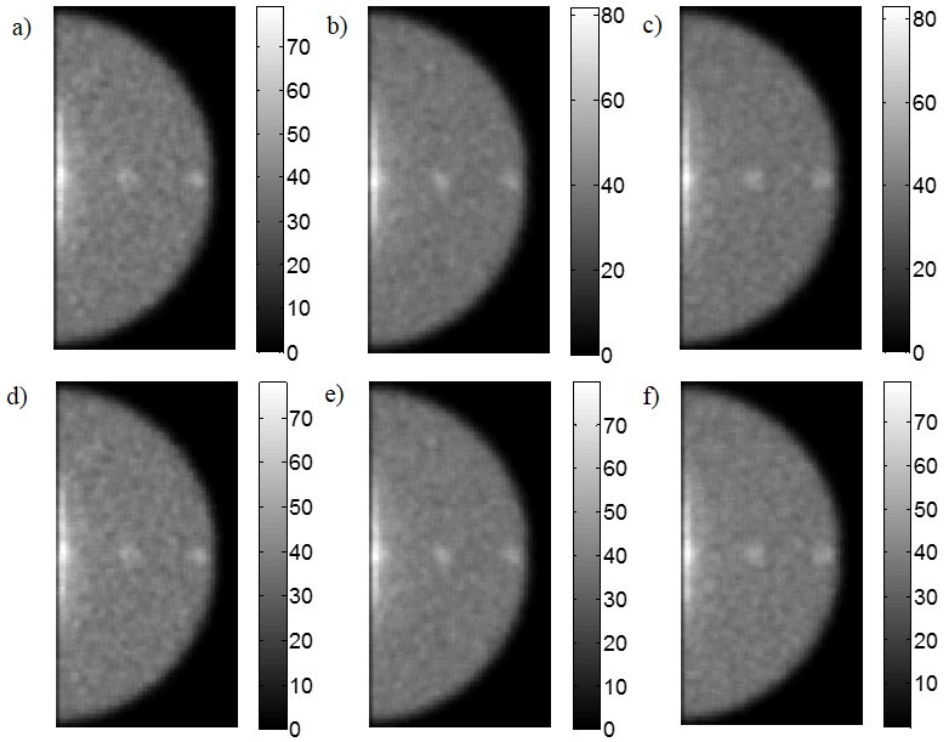

Figure 77: Breast projections with 1.5-mm resolution generated using conjugate counting methods. Top row: Average projections with tumors at a) 1-cm, b) 2.25-cm, and c) 3.5-cm depth. Bottom row: Geometric mean projections with tumors at d) 1-cm, e) 2.25-cm, and f) 3.5-cm depth. Colorbar units are in counts. All six images exhibit similar qualities. The region of high intensity counts along the chest wall found in the superior projections surrounds tumor 1. However, tumor 2 and 3 are easily observable.

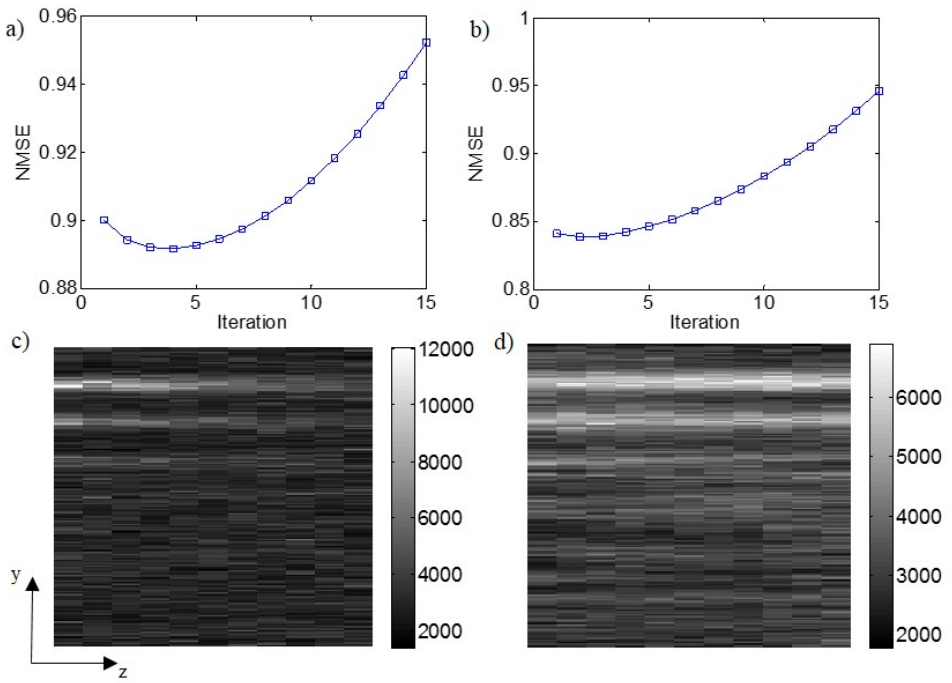

Figure 78: a) The NMSE curve and b) the contrast by iteration curve for the breast images with 1.5-mm resolution following OSEM reconstruction. Four OSEM iterations offer enhancements to contrast measurements for the resulting MIP and reprojected images without sacrificing image accuracy.

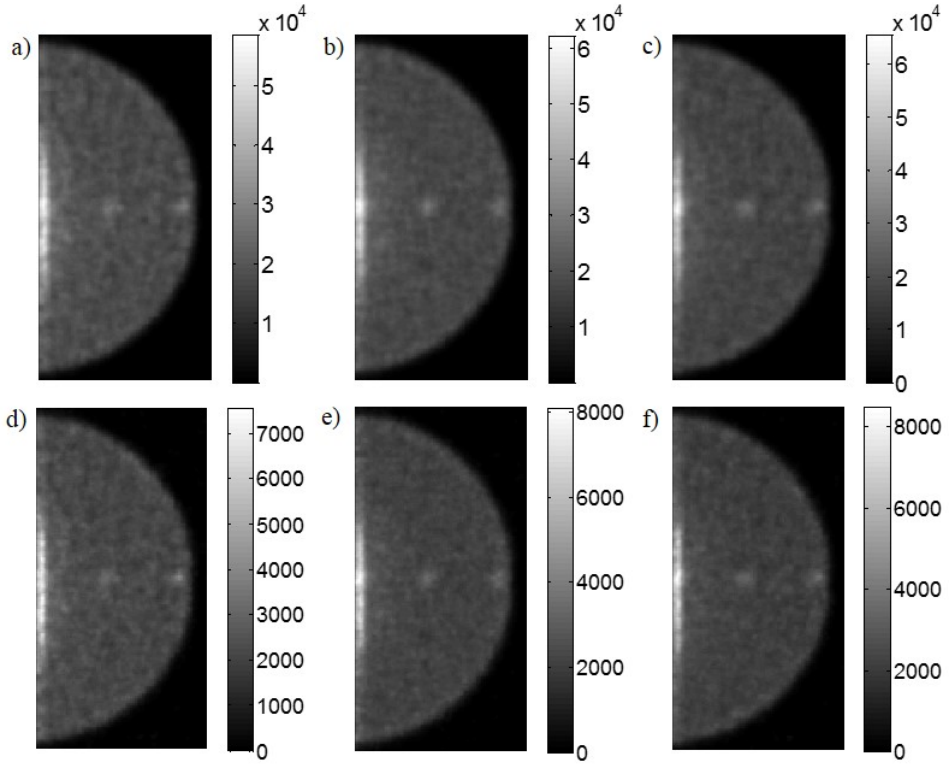

Figure 79: Reconstructed breast phantom projections with 1.5-mm spatial resolution generated using the OSEM reconstruction algorithm. Top row: Reprojected images with tumors at a) 1-cm, b) 2.25-cm, and c) 3.5-cm depth. Bottom row: Maximum-intensity projections with tumors at d) 1-cm, e) 2.25-cm, and f) 3.5-cm depth. Color-bar units are in number of emissions. Tumor 2 and 3 are observable in all six images. The large artifact encircling tumor 1, originally expressed in superior projections, is present in reconstructed images.

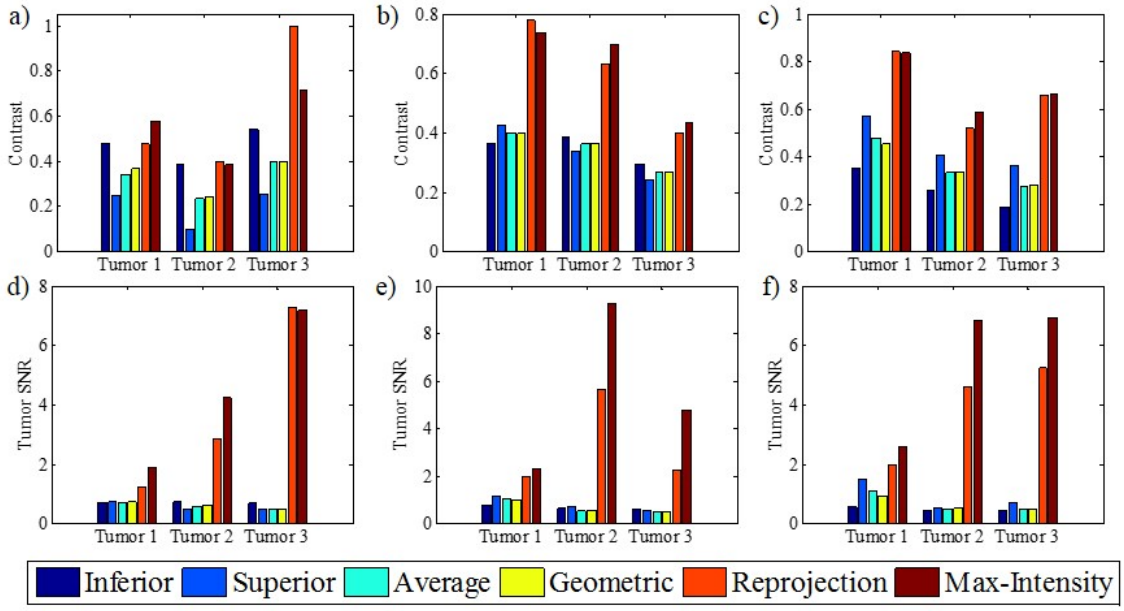

Figure 80: Image quality metrics of hot spots in breast projections with 1.5-mm spatial resolution. Contrast measurements of tumors at depths of a) 1 cm, b) 2.25 cm, and c) 3.5 cm. SNR measurements of tumors at depths of d) 1 cm, e) 2.25 cm, f) 3.5 cm. Generally, the reconstructed reprojection and MIP exhibit the highest contrast and SNR for tumors at a given depth.

superior camera metrics. The reprojection and MIP images show trends for greater contrast and SNR than the other projections, with nearly equivalent contrast, except for tumor 3 in figure 80 (a). However, the maximum-intensity projections generally have better SNR over the reprojected tomographic image.

7.3.2 Contrast-Detail Simulations

Figure 81 (a) and (b) show the NMSE curves for the reconstructed images with tumors at 1-cm and 2.25-cm depth from the inferior camera. The 4th and 3rd iterations are selected for the 1-cm and 2.25-cm depth tumors for reprojection and MIP

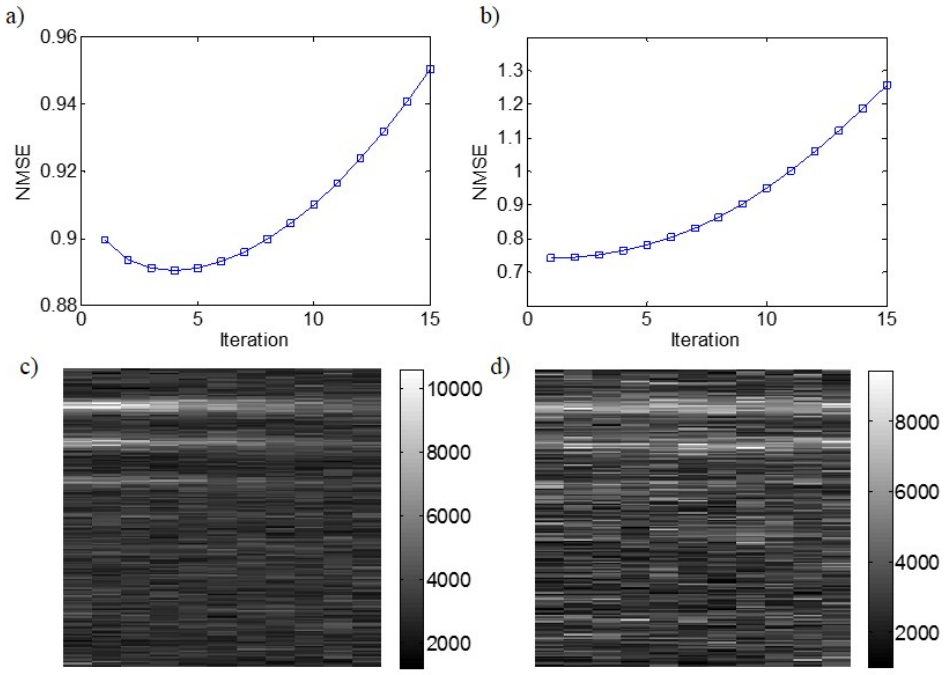

Figure 81: The NMSE curves of the OSEM reconstructed images with perfect resolution with tumors at a) the 1-cm depth and b) the center depth of the phantom. The coronal slices with the lowest NMSE through the 10:1 TBR tumors located at c) the 1-cm depth and d) the center depth. The coronal slices exhibit a spread of activity along the axis normal to both HPGe cameras, making the tumor depth location difficult to distinguish.

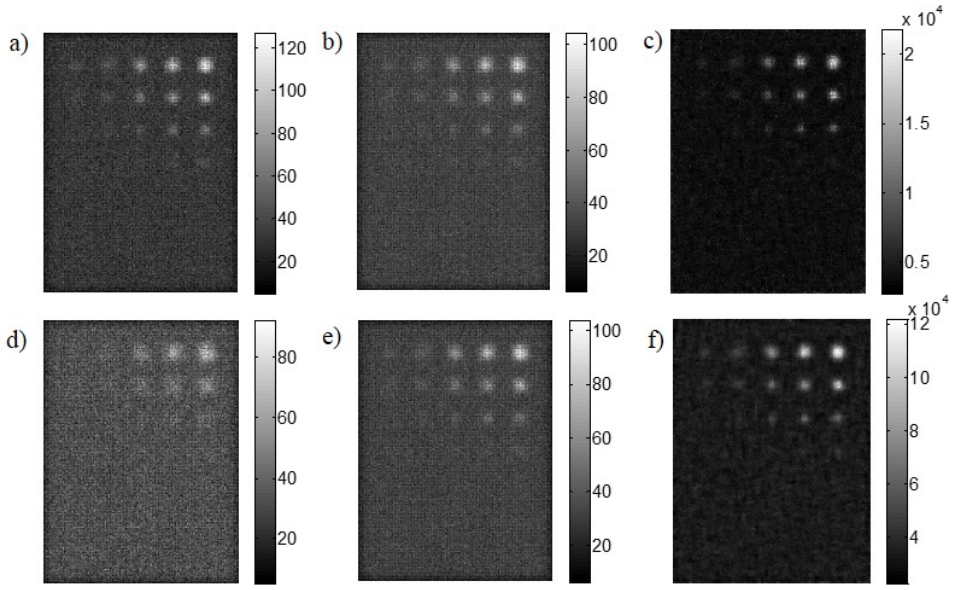

Figure 82: Contrast-detail projections with no spatial blurring for tumors at a 1-cm depth. a) Inferior, b) Average, c) MIP, d) Superior, e) Geometric mean, f) Reprojection. Colorbar units are in counts for the planar projection and in number of emissions for the reconstructed projections.

generation, respectively. The coronal slices through these images, shown in figure 81 (c) and (d), exhibit blurred activity along the z-axis, normal to the cameras. Thus, estimation of tumor localization by depth is unreliable.

The detector projections, conjugate-counting projections, and the reconstructed projections without spatial blurring are displayed in figure 82 and figure 83 for hot spots close to the inferior camera and equal-distant to both cameras, respectively. Without spatial blurring, the shadow (or outline) of the collimator permeates the background of the non-reconstructed projections. The images of figure 82 indicate that the high quality data from the inferior camera, where the tumors are in close proximity, is able to compensate for the noisy data collected in the superior camera

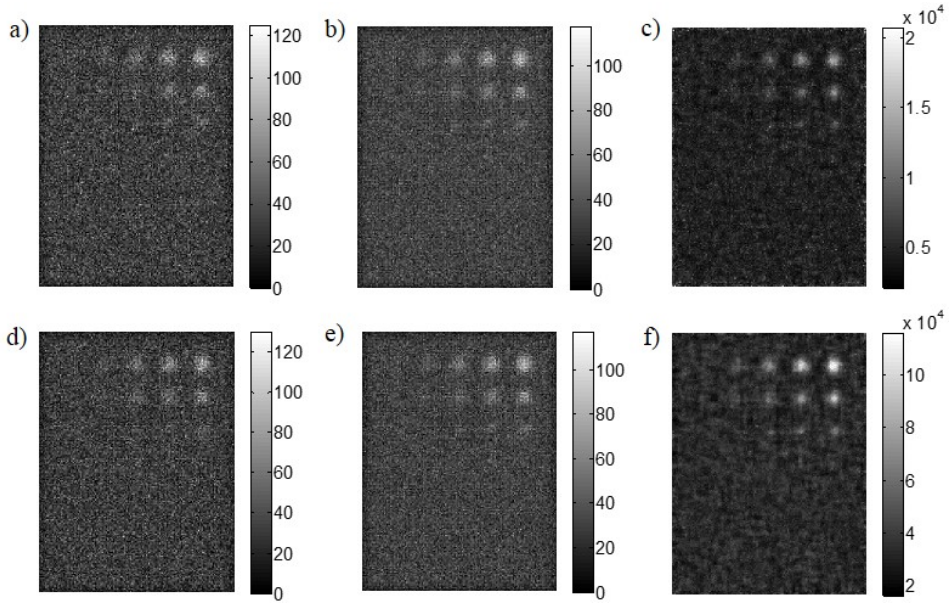

Figure 83: Contrast-detail projections with perfect spatial resolution for tumors at the center depth of the FOV. a) Inferior, b) Average, c) MIP, d) Superior, e) Geometric mean, f) Reprojection. Colorbar units are in counts for the planar projection and in number of emissions for the reconstructed projections.

to generate decent combined-projections through conjugate counting methods. The reprojected image and the MIP image are higher quality due to their low background intensities compared to the other projections. The same result is observed in figure 83, where the quality of collected projections is low due to the larger source-to-detector distance. The detector and combined projections are qualitatively equal, while the MIP and reprojection have reduced relative background to better distinguish the 6-mm diameter and the larger 5:1 TBR tumors.

The detectability curves for the two contrast-detail phantoms are displayed in figure 84. The SNR threshold curves for 1-cm depth tumors confirm that the high quality data from the inferior camera can offset the low SNR of the superior pro-

jection to generate combined projections with suitable SNR. The reprojection and MIP outperform the other projections in term of SNR of hot spots, however, the reprojected image has the greatest number of hot spots with an SNR ≥ 5. In terms of detectability near the inferior camera, the inferior projection alone has the same capability for detecting high TBR as the reconstructed projections, but falls off with low contrast and small diameter tumors. Combining the inferior and superior projections into average or geometric provides a moderate advantage to the superior camera alone. The reconstructed projections have the best capability to detect the smallest tumors across the TBRs investigated. For tumors seated equal-distant from both cameras, the conjugate counting methods produce projections with slightly higher SNR than the individual cameras alone. The reprojection of the tomographic image still provides the best SNR and tumor detection capability over the other projections in this imaging geometry.

The same projections of the two contrast-details were acquired with 1.5-mm spatial resolution. For the LAT acquisition, the NMSE curves, displayed in 85 (a) and (b), show that for tumors at the 1-cm and 2.25-cm depths have the most accurate images after four and two iterations, respectively. The coronal slices at these iterations, shown in figure 85 (c) and (d), still have blurred activity along the acquisition axis, limiting localization in tomographic images. Figure 86 and figure 87 display the collected and generated projections of the contrast-detail phantoms. Similar to the resolution-free projections, the inferior projection has higher quality data of the 1-cm depth

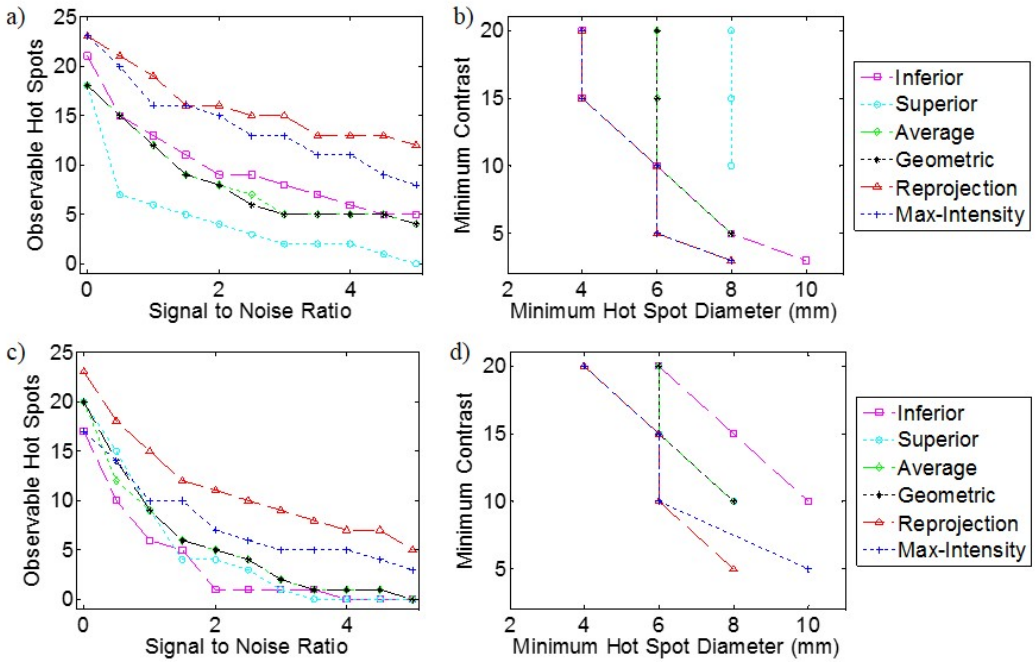

Figure 84: Tumor detectability based upon SNR and minimum TBR and diameter for the contrast-detail projections with no spatial resolution. Detectability for the 1-cm depth tumors based on a) SNR threshold and b) minimum tumor parameters. Detectability for the 2.25-cm depth tumors based on c) SNR threshold and d) minimum tumor parameters. The reconstructed projections consistently provide hot spots with higher SNR and tumor detection capability over the other projections.

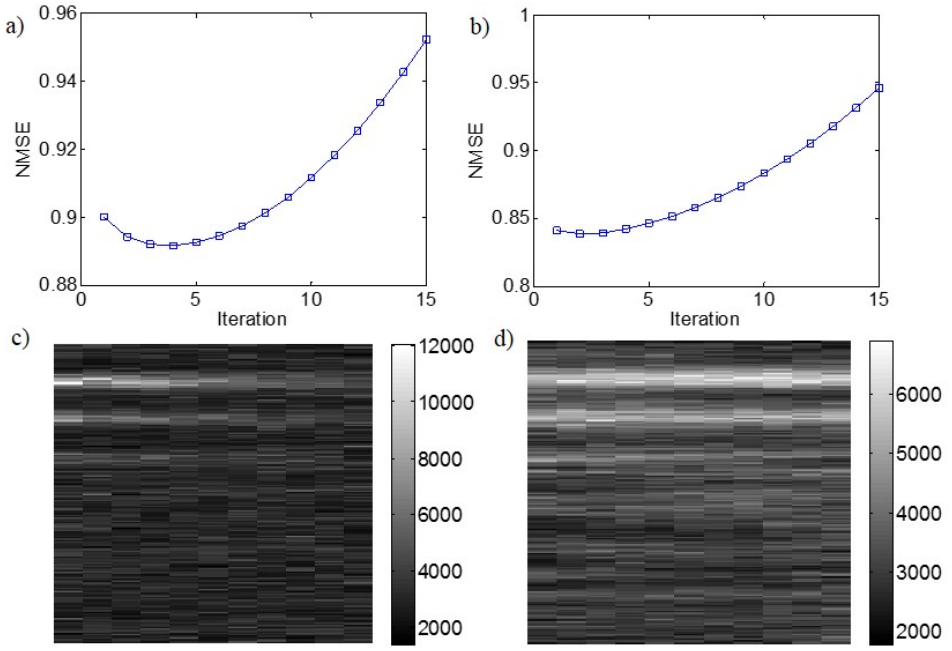

Figure 85: The NMSE curves of the OSEM reconstructed images with 1.5-mm resolution containing tumors at a) the 1-cm depth and b) the center depth of the phantom. The coronal slices with the lowest NMSE through the 10:1 TBR tumors located at c) the 1-cm depth and d) the center depth. The coronal slices exhibit a spread of activity along the axis normal to both HPGe cameras, making the tumor depth localization difficult to estimate.

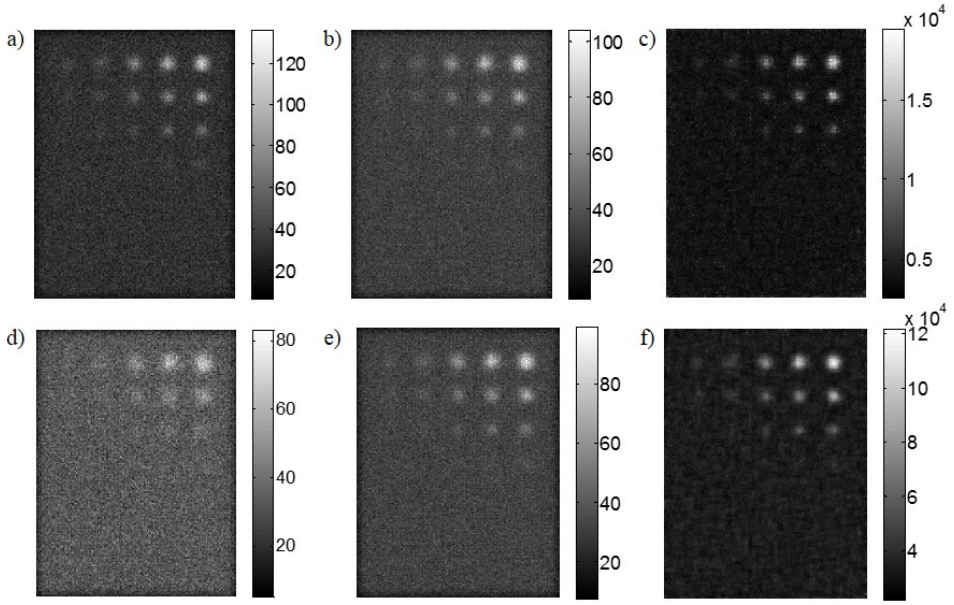

Figure 86: Contrast-detail projections with 1.5-mm spatial resolution for tumors at a 1-cm depth. a) Inferior, b) Average, c) MIP, d) Superior, e) Geometric mean, f) Reprojection. Colorbar units are in counts for the planar projection and in number of emissions for the reconstructed projections.

tumors than the superior projection. Combining these images to generate average and geometric mean projections does provide better visualization of the hot spots at the edge of detectability than the superior alone. However, the LAT projections grant the highest quality images with reduced background intensity and noise. This holds true for the 2.25-cm depth tumors, as the MIP and reprojected LAT images have a lower background level and noise than the other projections.

The detectability curves for these projections, shown in figure 88, mimic some of the features of figure 84. The reconstructed projections outperform the individual and conjugate counting projections in terms of tumor SNR for both contrast-detail phantoms, with the reprojected LAT image providing a slight advantage over the

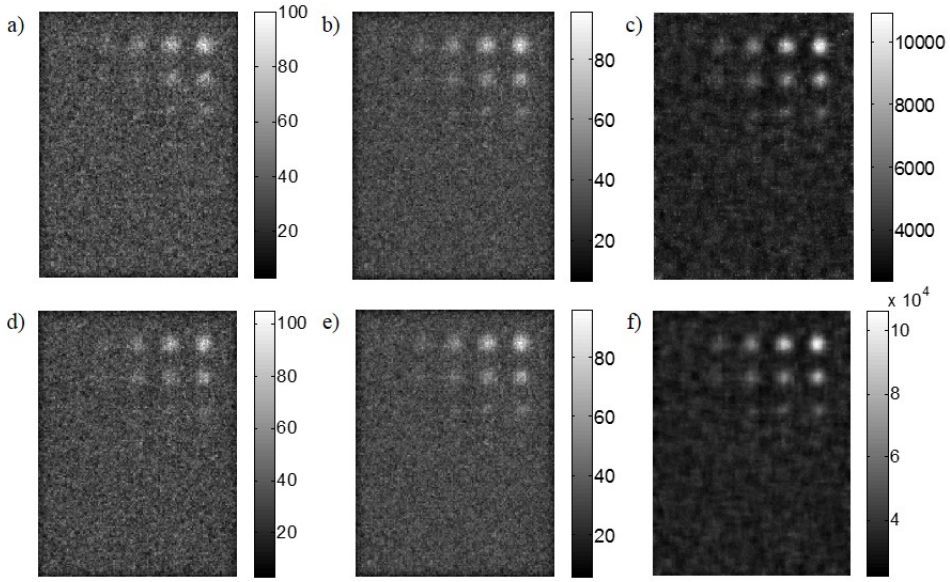

Figure 87: Contrast-detail projections with 1.5-mm spatial resolution for tumors at the center depth of the FOV. a) Inferior, b) Average, c) MIP, d) Superior, e) Geometric mean, f) Reprojection. Colorbar units are in counts for the planar projection and in number of emissions for the reconstructed projections.

MIP image across the investigated range of tumors. The contrast-detail curves for the 1-cm tumors show that only the inferior projection and LAT image are capable of identifying tumors across the entire TBR range, unlike the superior and conjugate counting projections. Interestingly, the inferior camera alone is able to resolve the 4-mm tumor with a TBR of 15:1. However, the reprojection has the best detection capability for low contrast tumors. The same general result is reflected in the 2.25-cm depth tumors, where the reconstructed LAT projections provide the best detection for smaller tumors over the other projections.

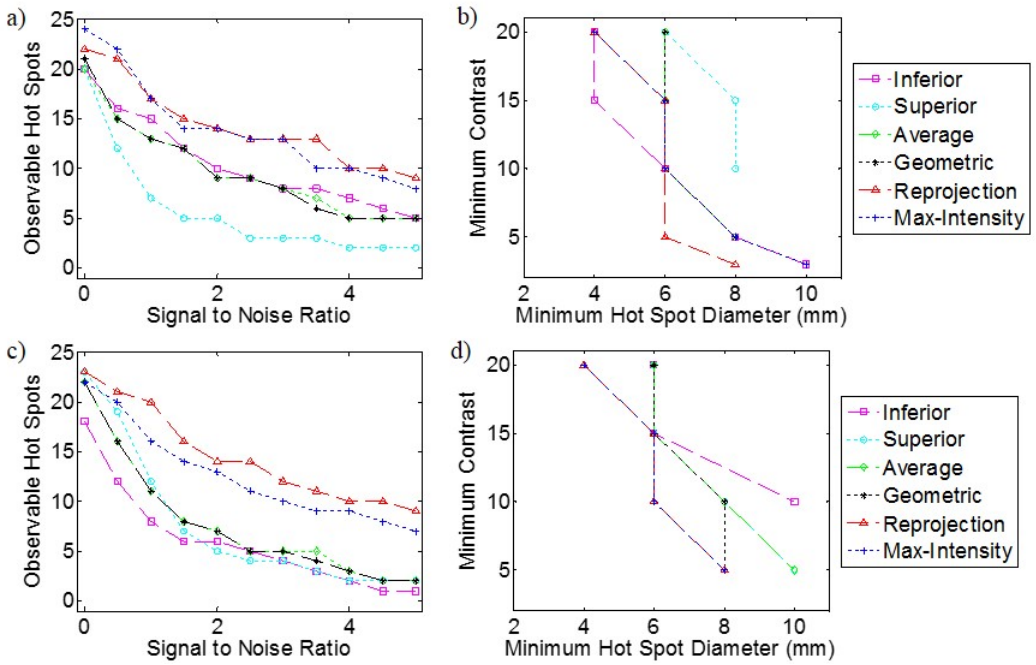

Figure 88: Tumor detectability based upon SNR and minimum TBR and diameter for the contrast-detail projections with 1.5-mm spatial resolution. Detectability for the 1-cm depth tumors based on a) SNR threshold and b) minimum tumor parameters. Detectability for the 2.25-cm depth tumors based on c) SNR threshold and d) minimum tumor parameters. The reconstructed projections consistently provide hot spots with higher SNR and tumor detection capability over the other projections.

7.4 Discussion

In this study, the imaging performance of an opposing HPGe dual-head breast imaging system is investigated. Projections are acquired from both cameras imaging a shared FOV. The generated projections are combined using conventional algebraic methods, which has been shown to offer resolution, contrast, and SNR enhancements over single camera projections (Majewski et al., 2006; Judy et al., 2010), and an OSEM reconstruction algorithm for limited-angle tomography, adopted from the single camera approached highlighted in chapter VI. The enhancements in image quality for two-camera systems have ultimately benefited breast cancer detection for small lesions (Hruska and O'Connor, 2008a; Rhodes et al., 2011). In conjugation with these findings in literature and the work discussed in this document, we hypothesize that similar enhancements will be reflected in a dual-head HPGe imaging system.

Throughout this work with limited-angle tomography, the NMSE curves from reconstructed images tend to diverge following a small number of iterations. Initial thoughts on the reason for this behavior is that the poor angular sampling of limited-angle tomography would lead to large errors in the reconstruction. However, the phantoms being reconstructed are uniform objects with a couple of tumors and no randomized structure. The MLEM and OSEM reconstruction algorithms are initialized assuming an uniform object as the first guess of the source activity distribution. Because the phantoms and the initial guesses are similar, the first few iterations will always yield the lowest error. To investigate this behavior further, more sophisticated

phantoms with greater anatomic structure will have to be applied to the detector model.

Upon close observation of the coronal slices from the tomographic contrast-detail images in figures 81 and 85, although the activity is blurred across several voxels, the activity signature differ considerably for tumors located at varying depths. The activity for the 1-cm depth tumors are concentrated near the inferior camera, while the centralized tumors exhibit an uniform spread across the FOV. This could indicate some minute amount of depth localization for tumors using limited-angle tomography. However, additional simulations are required to determine the degree of depth sensitivity. The signatures in depth activity for the 2.25-cm depth tumors could be mirrored with two tumors located at the same lateral position, but placed at points equal-distant from the center depth. Thus, further investigation into 3D tumor localization is warranted.

Comparing the performance of an ideal HPGe imaging system with no spatial blurring against a realistic system with 1.5-mm resolution revealed some conflicting results. The projections generated with and without spatial resolution are qualitatively similar with no obvious differences across the breast and contrast-detail phantoms. However, enhancements in SNR are observed for the maximum-intensity projections when spatial resolution is reintroduced to the camera projections. Increases in SNR could be explained by the spreading of activity, which can lower the intensity of the image noise. However, this increase in SNR for MIPs is not present with single cam-

era reconstructions (See chapter VI). Conducting additional Monte Carlo simulations may provide more reliable measure on the SNR of MIP images.

For the breast phantom simulations, the performance of the superior camera is impeded by the high liver activity. Quantitatively, the image quality of the superior projections are comparable to the inferior camera. However, the image artifact encompasses tumor 1 and obstructs its visualization. Furthermore, the image artifact is carried over to the combined conjugate-counting and the reconstructed tomographic images, hindering tumor detection along the chest wall. Considering standard detector packaging, lead shielding, dead-space and low performance along the edges of the detector, reliable imaging close to the chest wall may not be possible with the current camera architecture. Adjustments to the dual-head imaging system, such as employing different parallel-hole collimation, may be required to avoid viewing the torso and enable more reliable imaging along the chest wall.

The asymmetric image quality between inferior and superior projections marks a concern for the efficacy of average and geometric projections. Combining low-quality and high-quality datasets using conjugate counting methods yields projections with worse image quality than the high-quality projection alone. With equal, or similar images (where tumors are equal-distant from each camera), little improvement in image quality or detectability is observed in average or geometric mean projections. Thus, conjugate counting methods appear to offer no benefit beyond conventional planar imaging with HPGe cameras. Reviewing the individual projections simultaneously is

sufficient when tomography is not available.

Overall, the LAT projections substantially outperform the individual projections and combined planar images in terms of contrast, SNR, and tumor detection. In general, MIPs from the breast phantom with realistic spatial resolution offer the best contrast and SNR, although the reprojection of the tomographic image provides better detection capability for low contrast/TBR tumors. A drawback of the reconstructed breast images is the high-intensity liver artifact from the superior projection that contaminates the region around the chest wall. Refining the imaging geometry, either through collimator adjustment or image regularization, could mitigate the influence of out-of-view contributions, but at the sacrifice of a smaller imaging volume. Investigating depth sensitivity along the axis normal to the cameras may uncover unique signatures for tumor and lesions at specific positions and improve upon 3D localization.

7.5 Chapter Summary

In this chapter, Monte Carlo simulations using an opposing-view, dual-head HPGe imaging system were conducted to investigate potential image processing methods. Findings reveal that incorporating both sets of projection data into an OSEM reconstruction algorithm grants equivalent to better image performance for NBI and tumor detection capability over single camera planar imaging and conjugate counting algorithms. In the final chapter, we discuss the overall findings of this thesis, its

impact on nuclear breast imaging, and potential future directions for this research.

CHAPTER VIII

REFLECTIONS AND CONCLUSIONS

8.1 Dissertation Summary

To reiterate, the primary purpose of this work was to model and demonstrate the potential imaging capability of a breast-specific High-Purity Germanium imaging system. We theorize that the superb energy resolution of HPGe detectors has inherent value to single-photon imaging by offering effective scatter rejection capability, improved spatial resolution in part to lateral position processing through double-sided orthogonal strips, and good charge transport for depth-of-interaction estimation. Three specific aims were presented in an effort to accomplish this work's purpose.

To satisfy aim 1, a radiation transport Monte Carlo simulator and MATLAB scripts were employed to demonstrate the imaging performance of a general HPGe detector modeled after a CZT-based breast imager. The HPGe model was heavily influenced by detector characterization performed with fabricated position-sensitive HPGe systems by PHDs Co. (Knoxville, TN) following NEMA standards. The HPGe model was further experimentally validated against analytic expressions for spatial resolution and count sensitivity. Projections of a breast and torso phantom with spherical tumors were generated and evaluated by spectral analysis and image

quality. For equivalent activity imaged, the HPGe camera provided ∼25% increase in relative sensitivity and similar tumor contrast and SNR while better suppressing small-angle scatter events and background from the torso. In addition, image quality was maintained when CZT and HPGe projections of equivalent sensitivity were evaluated. Thus, a general HPGe camera offered potential for equal image capability of current commercial semiconductor-based breast-imagers while decreasing the injected radioactivity and lowering the radiation dose to the patient.

For aim 2, the generalized HPGe detector model was further optimized for breast cancer imaging by leveraging its unique design features for limited-angle tomography. First, various parallel-hole collimators were examined for count sensitivity and imaging performance, as these properties are highly regarded for cancer screening. Different registered, or matched bores to detector elements, were designed using material, penetration and spatial resolution factors, with the highest performing and sensitive collimators strongly considered. The square-hole tungsten, registered collimator with short and wide holes provided an 81% enhancement in sensitivity and better suppression of events from torso organs than the standard hexagonal-hole collimator, without sacrificing spatial resolution or imaging performance. A limited-angle tomographic acquisition scheme incorporating DOI information was developed with a Monte Carlo based system matrix and an iterative MLEM reconstruction. Images from the LAT acquisition resulted in hot spots with nearly doubled SNR and trends of improved contrast and detection capability for low TBR tumors compared to planar

projections. Thus, designing an optimized collimation and acquisition scheme with the features of HPGe detectors in mind granted further improvements to the system's imaging performance.

The intention behind aim 3 stemmed from the same progression of other breast imaging systems with the addition of a second HPGe camera with an opposing view of the field of view. The dual-head HPGe model collected projections from breast and contrast-detail phantoms. Various image processing methods were applied to combine projections into images, including conjugate counting and an adaptive OSEM reconstruction. Similar to the performance of the LAT acquisition with a single HPGe camera, the LAT acquisition combining inferior and superior camera projections consistently provided the best image quality, tumor SNR for hot spots, and detectability for tumors across different sizes and radioactivity concentrations. These results signify that a LAT acquisition with a dual-head HPGe imaging system may grant superior image quality than conventional planar imaging, additive, or multiplicative image processing.

In summarizing the breast imaging performance of HPGe imaging systems and providing prospective on the evolution of the work, figure 89 displays images simulated using the CZT breast camera model and all iterations of the HPGe model throughout the work. The reprojected tomographic images are shown from the single- and dual-head LAT acquisitions for this comparison. Figure 90 shows the tumor contrast and SNR measurements for the projections in figure 89. A trend of improved contrast

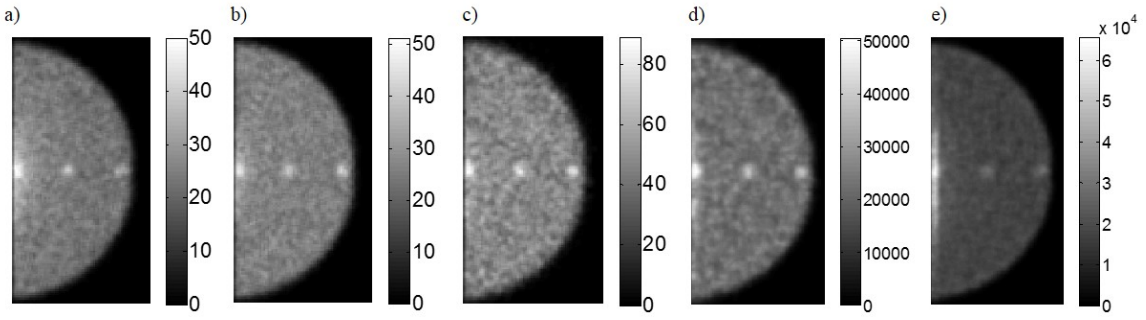

Figure 89: Breast projections with tumors at a 1-cm depth generated by different Monte Carlo models. a) CZT, b) Generalized HPGe, c) HPGe with optimal collimator, d) Single camera reprojected image, e) Dual-head reprojected image.

is observed when substituting the CZT detector for HPGe, then adopting optimal collimation and image processing. The trend is generally mirrored for tumor SNR. Performance with the dual-head HPGe system declines for tumor 1 and 2, but exhibits an increase for tumor 3. The liver artifact in the two-camera system would expectedly lower contrast and SNR, however, the asymmetric image quality for tumor 2 and 3 was not anticipated. Error analysis was not conducted for the LAT projections due to the unknown errors associated with iterative reconstruction and because only a single simulation trial was completed. Given these results and considering the liver artifact, it is concluded that employing a LAT scheme with a single-camera may provide consistently superior image quality over planar acquisitions and techniques. If the challenge of diminishing the effect of the liver contamination can be resolved, the increased count sensitivity afforded by the dual-head HPGe system, even with evidence of poor image quality, still makes it a worth-while pursuit.

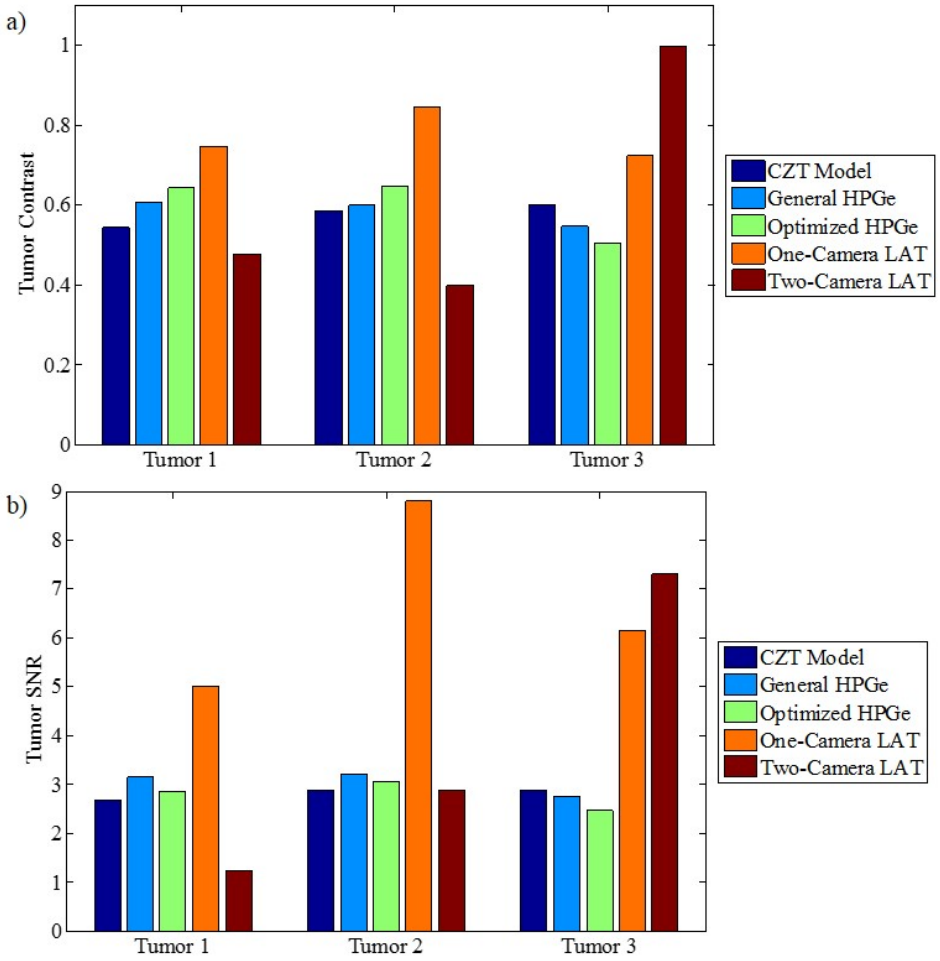

Figure 90: a) Measured tumor contrast and b) tumor SNR for different detector models. The reprojected tomographic image acquired with a single HPGe camera grants the highest image quality for 1-cm diameter tumors 1 cm from the camera near the chester wall and central to the to breast.

8.2 Future Considerations and Endeavors

The results of this research indicate the potential for HPGe cameras to have an impact on breast cancer imaging. However, progress is still required before these cameras become an integral part of the clinic. First, reliable crystal growth is essential to fabricating appropriately sized HPGe detectors. As stated in chapter III, PHDs. Co. have successfully grown an 14-cm diameter HPGe crystal and packaged it within the Germanium Gamma Camera version 2 (GGC2). Characterization and imaging performance of this system is essential to evaluating the detector's effectiveness, as well as the growth methods employed for the Germanium crystal. Beyond crystal growth methods, the configuration for electronic readout must be optimized for high quality imaging performance. For orthogonal strip setups, with an advantage in requiring fewer readout channels, more sophisticated pulse processing will need to be developed to improve lateral position estimation, and recover events within the gaps. Individual pixels for readout may reduce the pulse processing difficulty, but the total number of required channels is squared, leading to other electronic complications. With either choice of readout and pulse processing, optimization will benefit the intrinsic properties of spatial resolution, uniformity, count-rate, and count sensitivity.

Further exploration of an optimal parallel-hole collimator for the HPGe detector may be worth investigating. The spread of the radioactivity distribution normal to the camera in the reconstructed LAT images and the contamination from out-of-view sources in the superior projections ultimately limits the dual-head system's imaging

capability. Alternative collimation schemes, such as a slant-hole collimator for one or both detectors, could further improve NBI imaging capability. Acquiring projections from parallel-hole collimators with a slight difference in the angle of the holes on each of the opposing cameras would provide additional depth position information for tumors, which may offer better 3D localization of disease in tomographic images. Tilting the superior collimator away from the highly-radioactive liver would restrict its lines of sight to the detector, reducing the liver contributions. The tilt also increases the necessary scatter angle for detector entry, lowering the photon's energy to levels outside the energy window for event rejection. Conducting radiation transport simulations with these or other similar collimators may help to determine whether these changes might enhance NBI capability and image quality for the dual-head imaging system.

In the other limited-angle tomographic breast imaging systems, functional data from radionuclide imaging of an injected radiotracer and anatomical data from x-ray transmission imaging are both acquired to best characterize disease (Gong et al., 2012; Perez et al., 2011). To the author's current knowledge, modern dual-head breast imaging systems employing the contact geometry are unable to collect both datasets without camera motion around the breast. An interesting prospect would be the development of a combined HPGe NBI/x-ray system to obtain both sets of functional and anatomical data. Aside from the engineering challenges of fabricating such an imaging system, given the clinical protocols for breast cancer screening and the des-

ignated population for NBI, x-ray imaging may be ineffective. However, benefits to tumor sensitivity and specificity have been observed when muliti-modal techniques are employed (Brem et al., 2005; Rhodes et al., 2011). A future HPGe clinical system may observe similar benefit.

Once again, reducing the radiation dose imparted in NBI scans is paramount for making this imaging technique routine for women with dense breast tissue. Vast increases in count sensitivity and SNR were observed in the HPGe model with trends of improved image quality, enabling a reduction in injected radioactivity for matched SNR of conventional imaging. The CZT-based breast imaging system observed comparable contrast for a 5-fold reduction in injected activity, but only by allowing more scattered events and worsening spatial resolution (Hruska et al., 2012a). These sacrifices would not be required given the enhancements in counts and SNR observed with the HPGe model. Further study into decreased counts per projection must be investigated to validate if the SNR increases in LAT acquisitions translate into equivalent or improved image quality and detection capability.

REFERENCES

Amman, M. and Luke, P. (2000). Three-dimensional position sensing and field shaping in orthogonal-strip germanium gamma-ray detectors. *Nuclear Instruments and Methods in Physics Research Section A: Accelerators, Spectrometers, Detectors and Associated Equipment*, 452(1):155–166.

Anger, H. O. (1967). *Radioisotope Cameras in Instrumentation in Nuclear Medicine*, volume 1. New York: Academic.

Barber, H. B., B. H. W. J. M. (1996). *Nuclear Medicine*. Mosby-Year Book.

Barrett, H., Eskin, J., and Barber, H. (1995). Charge transport in arrays of semiconductor gamma-ray detectors. *Phys. Rev. Lett.*, 75:156–9.

Barrett, H. H. (1990). Limited-angle tomography for the nineties. *Journal of Nuclear Medicine*, 31(10):1688–1692.

Baum, G. (1977). Ultrasound mammography. *Radiology*, 122(1):199–205.

Bolotnikov, A., Camarda, G., Wright, G., and James, R. (2005). Factors limiting the performance of cdznte detectors. *Nuclear Science, IEEE Transactions on*, 52(3):589–598.

Brem, R. F., Floerke, A. C., Rapelyea, J. A., Teal, C., Kelly, T., and Mathur, V. (2008). Breast-specific gamma imaging as an adjunct imaging modality for the diagnosis of breast cancer 1. *Radiology*, 247(3):651–657.

Brem, R. F., Rapelyea, J. A., Zisman, G., Mohtashemi, K., Raub, J., Teal, C. B., Majewski, S., and Welch, B. L. (2005). Occult breast cancer: Scintimammography with high-resolution breast-specific gamma camera in women at high risk for breast cancer 1. *Radiology*, 237(1):274–280.

Brem, R. F., Schoonjans, J. M., Kieper, D. A., Majewski, S., Goodman, S., and Civelek, C. (2002). High-resolution scintimammography: a pilot study. *Journal of Nuclear Medicine*, 43(7):909–915.

Brown, F. B., Barrett, R., Booth, T., Bull, J., Cox, L., Forster, R., Goorley, T., Mosteller, R., Post, S., Prael, R., et al. (2002). MCNP version 5. *Trans. Am. Nucl. Soc.*, 87:4 4.

Brzymialkiewicz, C., Tornai, M., McKinley, R., Cutler, S., and Bowsher, J. (2006). Performance of dedicated emission mammotomography for various breast shapes and sizes. *Physics in medicine and biology*, 51(19):5051.

Brzymialkiewicz, C. N., Tornai, M. P., McKinley, R. L., and Bowsher, J. E. (2005). Evaluation of fully 3-d emission mammotomography with a compact cadmium zinc telluride detector. *Medical Imaging, IEEE Transactions on*, 24(7):868–877.

Burks, M., Jordan, E., Hull, E., Mihailescu, L., and Vetter, K. (2004). Signal interpolation in germanium detectors for improved 3-d position resolution. In *Nuclear Science Symposium Conference Record, 2004 IEEE*, volume 2, pages 1114–1118. IEEE.

Bushberg, J. T., S. J. A. L. E. M. and Boone, J. M. (2002). *The Essential Physics of Medical Imaging*. Lippincott Williams & Wilkins, Philadelphia, PA, 2nd edition.

Buvat, I., Laffont, S., Le Cloirec, J., Bourguet, P., and Di Paola, R. (2001). Importance of the choice of the collimator for the detection of small lesions in scintimammography: a phantom study. *Physics in medicine and biology*, 46(5):1343.

Campbell, D. and Peterson, T. (2011). Evaluating collimator designs for nuclear breast imaging with high-purity germanium detectors. In *Nuclear Science Symposium and Medical Imaging Conference (NSS/MIC), 2011 IEEE*, pages 2743–2748. IEEE.

Campbell, D. and Peterson, T. (2012). Simulations investigating the impact of depth-of-interaction in nuclear breast imaging with a dedicated germanium gamma camera. In *Nuclear Science Symposium and Medical Imaging Conference (NSS/MIC), 2012 IEEE*, pages 2718–2722. IEEE.

Campbell, D. L., Hull, E. L., and Peterson, T. E. (2013). Evaluation of a compact, general-purpose germanium gamma camera. In *Nuclear Science Symposium and Medical Imaging Conference (NSS/MIC), 2013 IEEE*, pages 1–6. IEEE.

Cherry, S. R., Sorenson, J. A., and Phelps, M. E. (2012). *Physics in nuclear medicine*. Elsevier Health Sciences.

Cooper, R. J., Boston, A. J., Boston, H. C., Cresswell, J. R., Grint, A., Harkness, L., Nolan, P., Oxley, D., Scraggs, D., Mather, A., et al. (2009). Positron emission tomography imaging with the smartpet system. *Nuclear Instruments and Methods in Physics Research Section A: Accelerators, Spectrometers, Detectors and Associated Equipment*, 606(3):523–532.

Cutler, S., Perez, K., Barnhart, H., and Tornai, M. (2010). Observer detection limits for a dedicated spect breast imaging system. *Physics in medicine and biology*, 55(7):1903.

Davison, M. E. (1983). The ill-conditioned nature of the limited angle tomography problem. *SIAM Journal on Applied Mathematics*, 43(2):428–448.

Delmon-Moingeon, L. I., Piwnica-Worms, D., Van den Abbeele, A. D., Holman, B. L., Davison, A., and Jones, A. G. (1990). Uptake of the cation hexakis (2-methoxyisobutylisonitrile)-technetium-99m by human carcinoma cell lines in vitro. *Cancer Res.*, 50(7):2198–2202.

Detko, J. F. (1969). Semiconductor diode matrix for isotope localization. *Phys. Med. Biol.*, 14(2):245.

Detko, J. F. (1973). A prototype, ultra-pure germanium, orghogonal strip gamma-camera. In *Medical radioisotope scintigraphy*.

Garibaldi, F., Cisbani, E., Colilli, S., Cusanno, F., Fratoni, R., Giuliani, F., Gricia, M., Lucentini, M., Lo Meo, S., Magliozzi, M., et al. (2006). Molecular imaging: High-resolution detectors for early diagnosis and therapy monitoring of breast cancer. *Nucl. Instr. & Meth. Phys. Rese. A*, 569:286–290.

Garibaldi, F., Cisbani, E., Colilli, S., Cusanno, F., Fratoni, R., Giuliani, F., Gricia, M., Lucentini, M., Magliozzi, M., Santavenere, F., et al. (2010). A novel high resolution and high efficiency dual head detector for molecular breast imaging: New results from clinical trials. *Nuclear Instruments and Methods in Physics Research Section A: Accelerators, Spectrometers, Detectors and Associated Equipment*, 617(1):227–229.

Garibaldi, F., Cisbani, E., Cusanno, F., Magliozzi, M., Torrioli, S., Cossu, E., Padovano, F., Simonetti, G., Schillaci, O., and Majewski, S. (2008). A novel high resolution and high efficiency dual head detector for molecular breast imaging. In *Nuclear Science Symposium Conference Record, 2008. NSS'08. IEEE*, pages 5647–5649. IEEE.

Giger, M. L., Doi, K., and Fujita, H. (1986). Investigation of basic imaging properties in digital radiography. 7. noise wiener spectra of ii–tv digital imaging systems. *Med. Phys.*, 13:131.

Gombia, M., Brill, A. B., Bollini, D., and Del Guerra, A. (2002). Comparison between a germanium orthogonal strip detector and an anger camera through a simulation and modeling study. *Nuclear Science, IEEE Transactions on*, 49(5):2196–2202.

Gong, Z., Klanian, K., Patel, T., Sullivan, O., and Williams, M. B. (2012). Implementation and evaluation of an expectation maximization reconstruction algorithm for gamma emission breast tomosynthesis. *Medical physics*, 39(12):7580–7592.

Gruber, G., Moses, W., and Derenzo, S. (1999). Monte carlo simulation of breast tumor imaging properties with compact, discrete gamma cameras. *Nuclear Science, IEEE Transactions on*, 46(6):2119–2123.

Guerin, L., Verger, L., Rebuffel, V., and Monnet, O. (2008). A new architecture for pixellated solid state gamma camera used in nuclear medicine. *Nuclear Science, IEEE Transactions on*, 55(3):1573–1580.

Gunter, D. L. (2004). *Collimator design for nuclear medicine*. Elsevier.

Hansen, W. L. and Haller, E. E. (1977). Amorphous germanium as an electron or hole blocking contact on high-purity germanium detectors. *Nuclear Science, IEEE Transactions on*, 24(1):61–63.

Harkness, L., Boston, A., Boston, H., Cooper, R., Cresswell, J., Grint, A., Nolan, P., Oxley, D., Scraggs, D., Beveridge, T., et al. (2009). Optimisation of a dual head semiconductor compton camera using geant4. *Nuclear Instruments and Methods in Physics Research Section A: Accelerators, Spectrometers, Detectors and Associated Equipment*, 604(1):351–354.

Hayward, J. and Wehe, D. (2007). Observation of charge-sharing in an hpge double-sided strip detector. *Nuclear Instruments and Methods in Physics Research Section A: Accelerators, Spectrometers, Detectors and Associated Equipment*, 579(1):99–103.

Hayward, J. and Wehe, D. (2008a). Incomplete charge collection in an hpge double-sided strip detector. *Nuclear Instruments and Methods in Physics Research Section A: Accelerators, Spectrometers, Detectors and Associated Equipment*, 586(2):215–223.

Hayward, J. P. and Wehe, D. K. (2008b). Charge loss correction in a high-purity germanium double-sided strip detector. *Nuclear Science, IEEE Transactions on*, 55(5):2789–2797.

Hendee, W. R. and Ritenour, E. R. (2003). *Medical imaging physics*. John Wiley & Sons.

Hendrick, R. E. (2010). Radiation doses and cancer risks from breast imaging studies. *Radiology*, 257:246–253.

Hruska, C. B. and O'Connor, M. K. (2006a). Czt detectors: How important is energy resolution for nuclear breast imaging? *Physica Medica*, 21:72–75.

Hruska, C. B. and O'Connor, M. K. (2006b). Effect of collimator selection on tumor detection for dedicated nuclear breast imaging systems. *Nuclear Science, IEEE Transactions on*, 53(5):2680–2689.

Hruska, C. B. and O'Connor, M. K. (2008a). A monte carlo model for energy spectra analysis in dedicated nuclear breast imaging. *Nuclear Science, IEEE Transactions on*, 55(1):491–500.

Hruska, C. B. and O'Connor, M. K. (2008b). Quantification of lesion size, depth, and uptake using a dual-head molecular breast imaging system. *Medical physics*, 35(4):1365–1376.

Hruska, C. B., Phillips, S. W., Whaley, D. H., Rhodes, D. J., and OConnor, M. K. (2008). Molecular breast imaging: use of a dual-head dedicated gamma camera to detect small breast tumors. *AJR. American journal of roentgenology*, 191(6).

Hruska, C. B., Weinmann, A. L., and O'Connor, M. K. (2012a). Proof of concept for low-dose molecular breast imaging with a dual-head czt gamma camera. part i. evaluation in phantoms. *Medical physics*, 39(6):3466–3475.

Hruska, C. B., Weinmann, A. L., Skjerseth, C. M. T., Wagenaar, E. M., Conners, A. L., Tortorelli, C. L., Maxwell, R. W., Rhodes, D. J., and O'Connor, M. K. (2012b). Proof of concept for low-dose molecular breast imaging with a dual-head czt gamma camera. part ii. evaluation in patients. *Medical physics*, 39(6):3476–3483.

Hudson, H. M. and Larkin, R. S. (1994). Accelerated image reconstruction using ordered subsets of projection data. *Medical Imaging, IEEE Transactions on*, 13(4):601–609.

Johnson, L. C., Campbell, D. L., Hull, E. L., and Peterson, T. E. (2011a). Characterization of a high-purity germanium detector for small-animal spect. *Phys. Med. Biol.*, 56(18):5877.

Johnson, L. C., Campbell, D. L., Ovchinnikov, O. S., and Peterson, T. (2011b). Performance characterization of a high-purity germanium detector for small-animal spect. In *Nuclear Science Symposium and Medical Imaging Conference (NSS/MIC), 2011 IEEE*, pages 607–612. IEEE.

Johnson, L. C., Ovchinnikov, O. S., Shokouhi, S., and Peterson, T. (2012). Characterization of a small-animal high-purity germanium spect system. In *Nuclear Science Symposium and Medical Imaging Conference (NSS/MIC), 2012 IEEE*, pages 2185–2190. IEEE.

Judy, P. G., Gong, Z., Dinion, N. L., Welch, B. L., Saviour, T. S., Kieper, D., Majewski, S., McKisson, J., Kross, B., Proffitt, J., et al. (2010). Analysis of image combination methods for conjugate breast scintigraphy. *IEEE Trans. Nucl. Sci.*, 57:1146–1154.

Judy, P. G., Welch, B., St Saviour, T., Kieper, D., Majewski, S., McKisson, J., Kross, B., Proffitt, J., Stolin, A., More, M. J., et al. (2007). Molecular breast imaging with directly opposing compact gamma cameras. In *Nuclear Science Symposium Conference Record, 2007. NSS'07. IEEE*, volume 6, pages 4040–4043. IEEE.

Keller, E. L. (1968). Optimum dimensions of parallel-hole, multi-aperture collimators for gamma-ray cameras. *Journal of Nuclear Medicine*, 9(6):233–235.

Khalkhali, I., Cutrone, J. A., Mena, I. G., Diggles, L. E., Venegas, R. J., Vargas, H. I., Jackson, B. L., Khalkhali, S., Moss, J. F., and Klein, S. R. (1995). Scintimammography: the complementary role of tc-99m sestamibi prone breast imaging for the diagnosis of breast carcinoma. *Radiology*, 196(2):421–426.

Khalkhali, I., Diggles, L. E., Taillefer, R., Vandestreek, P. R., Peller, P. J., and Abdel-Nabi, H. H. (1999). Procedure guideline for breast scintigraphy. *Journal of Nuclear Medicine*, 40(7):1233–1235.

Kieper, D., Majewski, S., Kross, B., Popov, V., Weisenberger, A., Welch, B., Wojcik, R., Williams, M., Goode, A., More, M., et al. (2003). Optimization of breast imaging procedure with dedicated compact gamma cameras. *Nuclear Instruments and Methods in Physics Research Section A: Accelerators, Spectrometers, Detectors and Associated Equipment*, 497(1):168–173.

Knoll, G. F. (2000). *Radiation detection and measurement*. John Wiley & Sons, Hoboken, 3rd edition.

Kriege, M., Brekelmans, C. T., Boetes, C., Besnard, P. E., Zonderland, H. M., Obdeijn, I. M., Manoliu, R. A., Kok, T., Peterse, H., Tilanus-Linthorst, M. M., et al. (2004). Efficacy of mri and mammography for breast-cancer screening in women with a familial or genetic predisposition. *New England Journal of Medicine*, 351(5):427–437.

Lange, K., Carson, R., et al. (1984). Em reconstruction algorithms for emission and transmission tomography. *J. Comput. Assist. Tomogr*, 8(2):306–316.

Luke, P., Amman, M., Phlips, B., Johnson, W., and Kroeger, R. (2000). Germanium orthogonal strip detectors with amorphous-semiconductor contacts. *Nuclear Science, IEEE Transactions on*, 47(4):1360–1363.

Majewski, S., Black, R., Kross, B., Popov, V., Welch, B., Wojécik, R., Williams, M., Moré, M., and Goodale, P. (2006). Phantom evaluations of a dedicated dual-head scintimammography system. *Physica Medica*, 21:35–38.

Majewski, S., Kieper, D., Curran, E., Keppel, C., Kross, B., Palumbo, A., Popov, V., Wisenberger, A., Welch, B., Wojcik, R., et al. (2001). Optimization of dedicated scintimammography procedure using detector prototypes and compressible phantoms. *Nuclear Science, IEEE Transactions on*, 48(3):822–829.

McCready, V., Parker, R., Gunnersen, E., Ellis, R., Moss, E., Gore, W., and Bell, J. (1971). Clinical tests on a prototype semiconductor gamma-camera. *Br. J. Radiol.*, 44(517):58–62.

Moré, M. J., Li, H., Goodale, P. J., Zheng, Y., Majewski, S., Popov, V., Welch, B., and Williams, M. B. (2007). Limited angle dual modality breast imaging. *Nuclear Science, IEEE Transactions on*, 54(3):504–513.

Mueller, B., OConnor, M. K., Blevis, I., Rhodes, D. J., Smith, R., Collins, D. A., and Phillips, S. W. (2003). Evaluation of a small cadmium zinc telluride detector for scintimammography. *J. Nucl. Med.*, 44:602–609.

Murthy, K., Aznar, M., Thompson, C. J., Loutfi, A., Lisbona, R., and Gagnon, J. H. (2000). Results of preliminary clinical trials of the positron emission mammography system pem-i: a dedicated breast imaging system producing glucose metabolic images using fdg. *Journal of Nuclear Medicine*, 41(11):1851–1858.

NEMA (2007). *NEMA Standards Publication NU 1-2007: Performance Measurements of Gamma Cameras*. National Electrical Manufacturers Association, Rosslyn, VA.

O'Connor, M. K., Hruska, C. B., Weinmann, A., Manduca, A., and Rhodes, D. J. (2010). Development of radiation dose reduction techniques for cadmium zinc telluride detectors in molecular breast imaging. In *Proc. SPIE*, pages 780603–780603. International Society for Optics and Photonics.

Orlov, S. (1975). Theory of three dimensional reconstruction: Ii. the recovery operator. *Sov. Phys Cristallogr*, 20:429–433.

Pani, R., De Vincentis, G., Scopinaro, F., Pellegrini, R., Soluri, A., Weinberg, I., Pergola, A., Scafe, R., and Trotta, G. (1998). Dedicated gamma camera for single photon emission mammography (spem). *Nuclear Science, IEEE Transactions on*, 45(6):3127–3133.

Pani, R., Pellegrini, R., Cinti, M., Bennati, P., Betti, M., Casali, V., Schillaci, O., Mattioli, M., Orsolini Cencelli, V., Navarria, F., et al. (2006). Recent advances and future perspectives of gamma imagers for scintimammography. *Nuclear Instruments and Methods in Physics Research Section A: Accelerators, Spectrometers, Detectors and Associated Equipment*, 569(2):296–300.

Patton, J., Price, R., Rollo, F., Brill, A., and Pehl, R. (1978). Clinical and experimental results with a 9 element high purity germanium array. *Nuclear Science, IEEE Transactions on*, 25(1):653–656.

Perez, K. L., Cutler, S. J., Madhav, P., and Tornai, M. P. (2011). Towards quantification of functional breast images using dedicated spect with non-traditional acquisition trajectories. *Nuclear Science, IEEE Transactions on*, 58(5):2219–2225.

Peterson, T. E. and Furenlid, L. R. (2011). Spect detectors: the anger camera and beyond. *Physics in medicine and biology*, 56(17):R145.

Pieper, B. C., Bowsher, J. E., Tornai, M. P., Peter, J., Greer, K., and Jaszczak, R. J. (2001). Breast tumor imaging using a tiltable head spect camera. *Nuclear Science, IEEE Transactions on*, 48(4):1477–1482.

Prats, E., Aisa, F., Abós, M. D., Villavieja, L., García-López, F., Asenjo, M. J., Razola, P., and Banzo, J. (1999). Mammography and 99mtc-mibi scintimammography in suspected breast cancer. *Journal of nuclear medicine: official publication, Society of Nuclear Medicine*, 40(2):296–301.

Raghunathan, P., Goodale, P. J., Klinger, J., Appleby, M., Atkinson, J., and Williams, M. B. (2005). Matched collimators for pixellated gamma camera. In *Nuclear Science Symposium Conference Record, 2005 IEEE*, volume 4, pages 4–pp. IEEE.

Raylman, R. R., Majewski, S., Wojcik, R., Weisenberger, A. G., Kross, B., Popov, V., and Bishop, H. A. (2000). The potential role of positron emission mammography for detection of breast cancer. a phantom study. *Medical physics*, 27(8):1943–1954.

Rhodes, D. J., Hruska, C. B., Phillips, S. W., Whaley, D. H., and Oconnor, M. K. (2011). Dedicated dual-head gamma imaging for breast cancer screening in women with mammographically dense breasts. *Radiology*, 258:106–118.

Robert, C., Montémont, G., Rebuffel, V., Buvat, I., Guérin, L., and Verger, L. (2010). Simulation-based evaluation and optimization of a new cdznte gamma-camera architecture (hisens). *Physics in medicine and biology*, 55(9):2709.

Robert, C., Montémont, G., Rebuffel, V., Verger, L., and Buvat, I. (2011). Optimization of a parallel hole collimator/CdZnTe gamma-camera architecture for scintimammography. *Med. Phys.*, 38:1806.

Rockmore, A. J. and Macovski, A. (1976). A maximum likelihood approach to emission image reconstruction from projections. *Nuclear Science, IEEE Transactions on*, 23(4):1428–1432.

Rosenberg, R. D., Hunt, W. C., Williamson, M. R., Gilliland, F. D., Wiest, P. W., Kelsey, C. A., Key, C. R., and Linver, M. N. (1998). Effects of age, breast density, ethnicity, and estrogen replacement therapy on screening mammographic sensitivity and cancer stage at diagnosis: review of 183,134 screening mammograms in Albuquerque, New Mexico. *Radiology*, 209:511–518.

Saad, W., Roslan, R., Mahdi, M., Choong, W.-S., Saion, E., and Saripan, M. (2011). Monte carlo design of optimal wire mesh collimator for breast tumor imaging process. *Nuclear Instruments and Methods in Physics Research Section A: Accelerators, Spectrometers, Detectors and Associated Equipment*, 648(1):254–260.

Saripan, M. I., Saad, W. M., Hashim, S., Mahmud, R., Nordin, A. J., and Mahdi, M. A. (2009). Monte carlo simulation on breast cancer detection using wire mesh collimator gamma camera. *Nuclear Science, IEEE Transactions on*, 56(3):1321–1324.

Schlosser, P., Miller, D., Gerber, M., Redmond, R., Harpster, J., Collis, W., and Hunter, W. (1974). A practical gamma-ray camera system using high-purity germanium. *Nuclear Science, IEEE Transactions on*, 21(1):658–664.

Shepp, L. A. and Vardi, Y. (1982). Maximum likelihood reconstruction for emission tomography. *Medical Imaging, IEEE Transactions on*, 1(2):113–122.

Shultis, J. K. and Faw, R. E. (2011). An mcnp primer. *Kansas State University, Manhattan*.

Silverstein, M. J., Lagios, M. D., Recht, A., Allred, D. C., Harms, S. E., Holland, R., Holmes, D. R., Hughes, L. L., Jackman, R. J., Julian, T. B., et al. (2005). Image-detected breast cancer: state of the art diagnosis and treatment. *Journal of the American College of Surgeons*, 201(4):586–597.

Smith, M. F., Majewski, S., and Weisenberger, A. G. (2003). Optimizing pinhole and parallel hole collimation for scintimammography with compact pixellated detectors. *Nuclear Science, IEEE Transactions on*, 50(3):321–326.

Taillefer, R., Robidoux, A., Lambert, R., Turpin, S., and Laperrière, J. (1995). Technetium-99m-sestamibi prone scintimammography to detect primary breast cancer and axillary lymph node involvement. *Journal of nuclear medicine: official publication, Society of Nuclear Medicine*, 36(10):1758–1765.

Ter-Pogossian, M. M. and Phelps, M. E. (1973). Semiconductor detector systems. In *Seminars in nuclear medicine*, volume 3, pages 343–365. Elsevier.

Thompson, C., Murthy, K., Picard, Y., Weinberg, I., and Mako, R. (1995). Positron emission mammography (pem): a promising technique for detecting breast cancer. *Nuclear Science, IEEE Transactions on*, 42(4):1012–1017.

Tornai, M. P., Bowsher, J. E., Archer, C. N., Peter, J., Jaszczak, R. J., MacDonald, L. R., Patt, B. E., and Iwanczyk, J. S. (2003). A 3d gantry single photon emission tomograph with hemispherical coverage for dedicated breast imaging. *Nuclear Instruments and Methods in Physics Research Section A: Accelerators, Spectrometers, Detectors and Associated Equipment*, 497(1):157–167.

Tornai, M. P., Brzymialkiewicz, C. N., Bradshaw, M. L., Bowsher, J. E., Patt, B. E., Iwanczyk, J. S., Li, J., and MacDonald, L. R. (2005). Comparison of compact gamma cameras with 1.3-and 2.0-mm quantized elements for dedicated emission mammotomography. *Nuclear Science, IEEE Transactions on*, 52(5):1251–1256.

Tornai, M. P., Brzymialkiewicz, C. N., Cutler, S. J., and Madhav, P. (2004). Comparison of scintimammography and dedicated emission mammotomography. In *Nuclear Science Symposium Conference Record, 2004 IEEE*, volume 5, pages 2818–2822. IEEE.

Tornai, M. P., Patt, B. E., Iwanczyk, J. S., Levin, C., and Hoffman, E. (1997). Discrete scintillator coupled mercuric iodide photodetector arrays for breast imaging. *Nuclear Science, IEEE Transactions on*, 44(3):1127–1133.

Van Loef, E. V., Wilson, C. M., Cherepy, N. J., Hull, G., Payne, S. A., Choong, W.-S., Moses, W. W., and Shah, K. S. (2009). Crystal growth and scintillation properties of strontium iodide scintillators. *Nuclear Science, IEEE Transactions on*, 56(3):869–872.

Vetter, K., Burks, M., and Mihailescu, L. (2004). Gamma-ray imaging with position-sensitive hpge detectors. *Nuclear Instruments and Methods in Physics Research Section A: Accelerators, Spectrometers, Detectors and Associated Equipment*, 525(1):322–327.

Villanueva-Meyer, J., Leonard Jr, M., Briscoe, E., Cesani, F., Ali, S., Rhoden, S., Hove, M., and Cowan, D. (1996). Mammoscintigraphy with technetium-99m-sestamibi in suspected breast cancer. *Journal of nuclear medicine: official publication, Society of Nuclear Medicine*, 37(6):926–930.

Wagenaar, D. J. (2004). *CdTe and CdZnTe semiconductor detectors for nuclear medicine imaging*. Elsevier.

Warner, E., Hill, K., Causer, P., Plewes, D., Jong, R., Yaffe, M., Foulkes, W. D., Ghadirian, P., Lynch, H., Couch, F., et al. (2011). Prospective study of breast cancer incidence in women with a brca1 or brca2 mutation under surveillance with and without magnetic resonance imaging. *Journal of Clinical Oncology*, 29(13):1664–1669.

Warwick, D., Smallwood, J., Guyer, P., Dewbury, K., and Taylor, I. (1988). Ultrasound mammography in the management of breast cancer. *British journal of surgery*, 75(3):243–245.

Weinmann, A. L., Hruska, C. B., and OConnor, M. K. (2009). Design of optimal collimation for dedicated molecular breast imaging systems. *Med. Phys.*, 36:845.

Wieczorek, H. and Goedicke, A. (2006). Analytical model for spect detector concepts. *Nuclear Science, IEEE Transactions on*, 53(3):1102–1112.

Williams, M. B., Goode, A. R., Galbis-Reig, V., Majewski, S., Weisenberger, A. G., and Wojcik, R. (2000). Performance of a pspmt based detector for scintimammography. *Physics in medicine and biology*, 45(3):781.

Williams, M. B., Judy, P. G., Gunn, S., and Majewski, S. (2010). Dual-modality breast tomosynthesis 1. *Radiology*, 255(1):191–198.

Williams, M. B., Narayanan, D., More, M. J., Goodale, P. J., Majewski, S., and Kieper, D. (2002). Analysis of position-dependent compton scatter in scintimammography with mild compression. In *Nuclear Science Symposium Conference Record, 2002 IEEE*, volume 2, pages 863–867. IEEE.

Zhang, F., He, Z., Knoll, G. F., Wehe, D. K., and Berry, J. E. (2005). 3-d position sensitive cdznte spectrometer performance using third generation vas/tat readout electronics. *Nuclear Science, IEEE Transactions on*, 52(5):2009–2016.

Zhang, F., He, Z., Xu, D., Knoll, G. F., Wehe, D. K., and Berry, J. E. (2004). Improved resolution for 3-d position sensitive cdznte spectrometers. *Nuclear Science, IEEE Transactions on*, 51(5):2427–2431.